UNIVERSITY OF CALIFORNIA SAN DIEGO

Active Metasurfaces and Their Applications

A Dissertation submitted in partial satisfaction of the
requirements for the degree
Doctor of Philosophy

in

Electrical Engineering (Electronic Circuits and Systems)

by

Aobo Li

Committee in charge:

Professor Daniel F. Sievenpiper, Chair
Professor Eric Fullerton
Professor Boubacar Kante
Professor Brian Keating
Professor Vitaliy Lomakin

2018

The Dissertation of Aobo Li is approved, and it is acceptable in quality and form for publication on microfilm and electronically:

_____

_____

_____

_____

_____

Chair

University of California San Diego

2018

DEDICATION

To my beloved wife *Rui Xu* ,my parents Mr. *Yumin Li* and Mrs. *Guiyun Yi* and all my friends.

TABLE OF CONTENTS

LIST OF FIGURES

LIST OF TABLES

LIST OF ABBREVIATIONS

AMC	Artificial magnetic conductor
FSS	Frequency selective surface
EBG	Electromagnetic band gap
HIS	High impedance surface
TEM	Transverse electromagnetic
EM	Electromagnetic
TE	Transverse electric
TM	Transverse magnetic
RF	Radio frequency
DC	Direct current
RF	Radio frequency
PEC	Perfect electric conductor
PMC	Perfect magnetic conductor
TRM	Transverse resonance method
MOSFET	Metal-oxide-semiconductor field effect transistor
MS	Metasurface

ACKNOWLEDGEMENTS

I would like to give my greatest thanks to my Ph.D advisor, Prof. Daniel F. Sievenpiper. He is such a smart, knowledgable and supportive advisor who always does his utmost to support me and all his other students in a way that makes us feel Ph.D is such a challenging but exciting life. I learnt quite much not only in our area related knowledge but most importantly the most efficient way of solving problems, which I believe is the most valuable thing I have gained from my Ph.D life. I would like to show my appreciation to my committee members, Professor Eric Fullerton, Professor Boubacar Kante, Professor Vitaliy Lomakin, and Professor Brian Keating, for taking the time to be part of my committee and for their precious comments and suggestions. A special thank my parents, family, my friends, and especially everyone in the Applied Electromagnetics Group at UCSD.

The material in this dissertation is based on the following papers which are either published or preparation for publication.

Chapter 2 is based on and is mostly a reprint of the following paper: **A. Li**, E. Forati, and D. Sievenpiper, "Study of Electric Field Enhancement in Resonant Metasurfaces", *Journal of Optics* **19**, 125104, 2017. The dissertation author was the primary author of the work of the material in these papers, and the co-authors have approved the use of the material for this dissertation.

Chapter 3 is based on and is mostly a reprint of the following paper: **A. Li**, S. Kim, Y. Luo, Y. Li, J. Long, and D. Sievenpiper, "High-Power, Transistor-Based Tunable and Switchable Metasurface absorber", *IEEE Transactions on Microwave Theory and Techniques*, vol. **65**, no.8, pp.2810-2818, August 2017. The dissertation author was the primary author of the work of the material in this paper, and the co-author has approved the use of the material for this dissertation.

Chapter 4 is based on and is mostly a reprint of the following paper: **A. Li**, Y. Li, E. Forati, S. Kim, J. Lee, J. Long and D. Sievenpiper, "Direct conversion of static voltage to a steerable RF radiation beam using an active metasurface", in preparation.The dissertation author was the primary author of the work of the material in this paper, and the coauthors have approved the use of the material for this dissertation.

Chapter 5 is based on and is mostly a reprint of the following paper: **A. Li**, Y. LI, J. Long, E. Forati and D. Sievenpiper, "Time moduated non-reciprocal metasurface surface wave absorber", in preparation. The dissertation author was the primary author of the work of the material in this paper, and the co-authors have approved the use of the material for this dissertation.

Chapter 6 gives a summary of the these followed by an overview of the on-going and envisions of future works.

Aobo Li

La Jolla, CA

Dec 2018

VITA

2010	Bachelor of Science in Electrical Engineering, Shanghai Jiao Tong University, Shanghai, China
2013	Master of Science in Information Engineering, Shanghai Jiao Tong University, Shanghai, China
2013	Master of Science in Telecommunications, Georgia Institute of Technology (Shanghai Campus), Shanghai, China
2014	Applications Engineer at National Instruments, Beijing, China
2014-2017	Graduate Student Researcher, University of California San Diego, U.S.A.
2018	Doctor of Philosophy in Electrical Engineering (Electronic Circuits and Systems), University of California San Diego, U.S.A.

PUBLICATIONS

Journal Articles

A. Li, Y. Li, J. Long, E. Forati, and D. Sievenpiper, "Time moduated non-reciprocal metasurface surface wave absorber", in preparation.

A. Li, Y. Li, E. Forati, S. Kim, J. Lee, J. Long, and D. Sievenpiper, "Direct conversion of DC to a steerable RF radiation beam using an active metasurface", submitted.

A. Li, S. Singh, and D. Sievenpiper, "Metasurfaces and their applications", *Nanophotonics* **7**, no.6 989-1011, 2018.

A. Li, Z. Luo, H.Wakatsuchi, S. Kim, and D. Sievenpiper, "Nonlinear, active, and tunable metasurfaces for advanced electromagnetics applications", *IEEE Access* **5**, 27439-27452, 2017

A. Li, E. Forati, and D. Sievenpiper, "Study of the electric field enhancement in resonant metasurfaces", *Journal of Optics* **19**, no.12, 125104, 2018

A. Li, S. Kim, Y. Luo, Y. Li, J. Long, and D. Sievenpiper, "High-power transistor-based tunable and switchable metasurface absorber", *IEEE Transactions on Microwave Theory and Techniques* **65**, no.8, 2810-2818, 2017.

Y. Li, **A. Li**, and T. Cui, "Four-channel orbital angular momentum beam multiplexer designed with low-profile metasurfaces", *Journal of Physics D: Applied Physics*, 2018.

Y. Li, **A. Li**, T. Cui, and D. Sievenpiper, "Multi-Wavelength Multiplexing Hologram Designed using Impedance Metasurfaces", *IEEE Transactions on Antennas and Propagation* **66**, no.11, 6408-6413, 2018.

Y. Li, **A. Li**, and D. Sievenpiper, "Theoretical design and analysis of wideband active hard electromagnetic surfaces using non-Foster circuit loaded anisotropic metasurfaces", *Journal of Physics D: Applied Physics* **51**, no.7, 075101, 2018.

Y. Luo, S. Kim, **A. Li**, and D. Sievenpiper, "Theoretical analysis of nonlinear surface wave absorbing metasurfaces", *Optics express* **26**, no.2, 797-810, 2018.

E. Forati, S. Piltan, **A. Li**, and D. Sievenpiper, "Experimental study of the interaction between DC discharge microplasmas and CW lasers", *Optics express* **24**, no.2, 1495-1560, 2016.

Conference Papers

A. Li, E. Forati, S. Kim, J. Lee, Y. Li, and D. Sievenpiper, "Periodic structures for scalable high-power microwave transmitters", 2017 IEEE Antennas and Propagation Symposium, San Diego, CA, July 9, 2017

A. Li, E. Forati, and D. Sievenpiper, "Study of the electric field enhancement of high-impedance surfaces", 2016 IEEE Antennas and Propagation Symposium, Fajardo, Puerto Rico, July 9, 2016

S. Kim, **A. Li**, and D. Sievenpiper, "Reconfigurable impedance ground plane for broadband antenna systems", 2017 IEEE Antennas and Propagation Symposium, San Diego, CA, July 9, 2017

ABSTRACT OF THE DISSERTATION

Active Metasurfaces and Their Applications

by

Aobo Li

Doctor of Philosophy in Electrical Engineering (Electronic Circuits and Systems)

University of California San Diego 2018

Professor Daniel F. Sievenpiper, Chair

Metasurfaces are sub-wavelength scale ($\ll \lambda/4$), two dimensional (2D) periodic structures being widely studied due to their unique ability to manipulate electromagnetic waves in microwave and optical frequencies in fields of antennas, absorbers, surface waveguides, cloaking, modulators, polarizers, lenses and imaging, etc.

Despite of the unique properties of the metasurfaces, they have limitations including bandwdith, reciprocity or linear response especially in microwave frequencies. By applying active electronics to the metasufaces could potentially add additional dimensions to reconfigure or modulate the property of the surface resulting in non-linear property, swithcability,

frequency and power dependency, non-reciprocity as well as wider bandwidth, etc. In this thesis, we studied the benefits of loading active components on metasurfaces specifically in areas of absorbers and transmitters, which overcomes some limitations of conventional approaches.

The thesis first introduces the metasurfaces and their unique properties as well as the applications. Specifically, high impedance surfaces (HIS) are widely adopted in low profile antenna applications, surface wave suppression and artificial magnetic conductors, etc due to existence of the forbidden band gap. Then the thesis studied the electric field enhancement of the high impedance surfaces in both microwave and near infrared frequencies. The bandstop properties of the HIS has great advantages in absorbers. By applying transistors on the HIS, the absorbers could be switched and tuned, which are discussed in the 3rd chapter of the thesis. On the other hand, the thesis also introduced a direct DC to radio frequency (RF) radiation by applying avalanche switches to the metasurface. A non-reciprocal surface wave metasurface absorber is introduced with time and spatial modulation technique applied.

Chapter 1

Introduction

Electromantics [1] and wave propagations are observed, studied and applied over a variety of fields from telecommunications, healthcare, space exploration and scientific researches, etc. As systems are getting more and more complicated with increasingly compact necessities, modern electronic systems require a thinner frontends interacting with electromagnetic waves. Metasurfaces [2–5] stand out due to it's sub-wavelength properties and widely applied in absorbers, field enhancement applications and atennas from microwave to visible. With the increasing demand on reconfigurability of the system, it is essential to enable the metasurfaces with switchability and tunability to improve the functionality of the whole system in applications like absorbers, transmitters and antenna ground planes etc.

1.1 Metasurfaces and their applications

Metasurfaces are a topic of significant research and are used in various applications due to their unique ability to manipulate electromagnetic waves in microwave and optical frequencies, shown in Fig. 1.1. These artificial sheet materials, which are usually

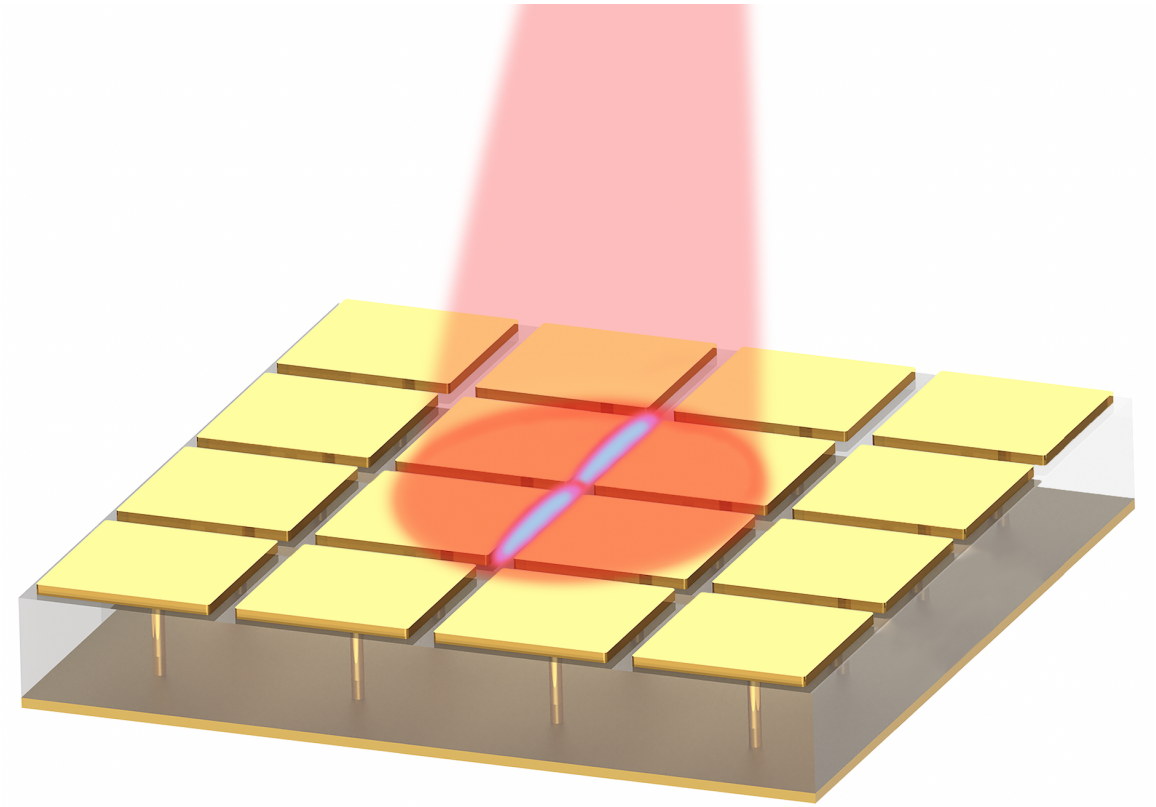

Figure 1.1: Metasurface: High impedance surface as an example.

composed of metallic patches or dielectric etchings in planar or multi-layer configurations with subwavelength thickness, have the advantages of light weight, ease of fabrication, and ability to control wave propagation both on the surface and in the surrounding free space. Recent progress in the field has been classified by application and reviewed in this article. Starting with the development of frequency-selective surfaces and metamaterials, the unique capabilities of different kinds of metasurfaces have been highlighted. Surface impedance can be varied and manipulated by patterning the metasurface unit cells, which has broad applications in surface wave absorbers and surface waveguides. They also enable beam shaping in both transmission and reflection. Another important application is to radiate in a leaky wave mode as an antenna. Other applications of metasurfaces include

cloaking, polarizers, and modulators. The controllable surface refractive index provided by metasurfaces can also be applied to lenses. When active and non-linear components are added to traditional metasurfaces, exceptional tunability and switching ability are enabled. Finally, metasurfaces allow applications in new forms of imaging.

When a wave in free space impinges on a surface, reflection and transmission are governed by the effective surface properties, which can be described in terms of its impedance. Frequency-selective surfaces (FSS) [6–8] have been widely studied and used in filters, absorbers, antenna radomes, etc., due to their ability to selectively transmit or reflect waves of different frequencies or incident angles. FSS are composed of subwavelength periodic metallic structures. Metasurfaces, similar to FSS, provide an effective surface impedance, which can be specifically designed and manipulated for various applications including absorption [9–14], wave front engineering [15–17], leaky-wave radiation [18–23], cloaking [24–30], phase and polarization control [31–33], as well as lenses [34–37] and imaging structures [38–43].

1.2 High impedance surface

High impedance surface (HIS) [44], first invented by Prof. Daniel F Sievenpiper in 1999, was studied broadly in the past two decades in areas of low profile antennas [45], absorbers, wavefront engineering, etc. A high impedance surface is composed of unit cells with periodic, sub-wavelength metallic patches backed by a ground plane with a via in the center conducting the top patch to the ground, the side view of which is shown in Fig. 1.2. A simple equivalent circuit model of the HIS could be represented as a parallel *RLC* circuit. The reason the surface is called high impedance surface is because at resonance, there is a high impedance region, which could be extracted from the dispersion diagram of the surface,

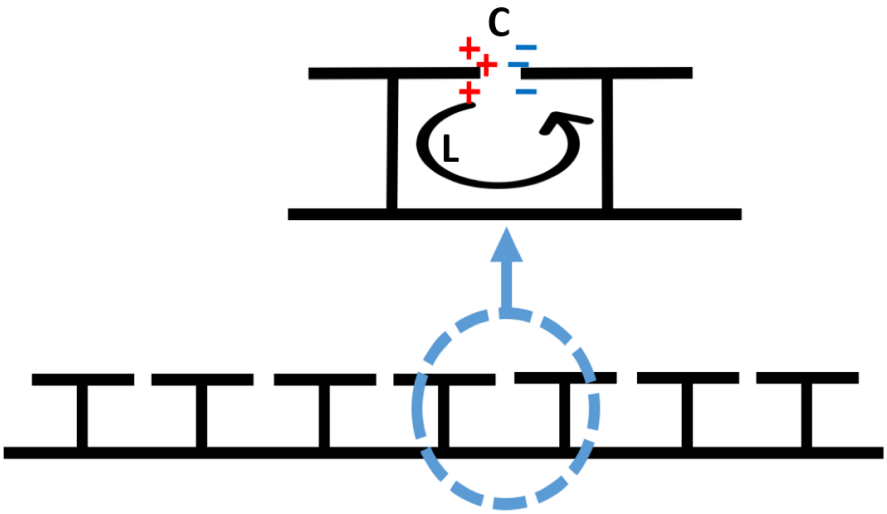

Figure 1.2: Side view of high impedance surface array with zoomed view of resonating unit cell.

shown in Fig. 1.3. A bandgap is observed between the first transverse electric (TE) and the first transverse magnetic (TM) mode. In other words, no surface waves are supported within the band gap, and this interesting property can be used in applications such as de-coupling of nearby antennas. At resonance, the image currents add up in phase at the surface showing similar properties of the perfect magnetic conductor (PMC) surface, that are widely applied in low profile antenna applications, since the antennas could be placed right above the surface without $\lambda/4$ distance from ground plane limitations.

Additionally, although the artificially engineered structures are able to work as the absorber, there will be significant scattering into free space or backward reflections to other systems which are sharing the same platform, while the reactive coating does not cover the entire outer structure of interest. Therefore, a new type of nonlinear metasurface such as an adaptive absorber is needed to mitigate high surface currents for decoupling other sensitive components of the shared conductive body.

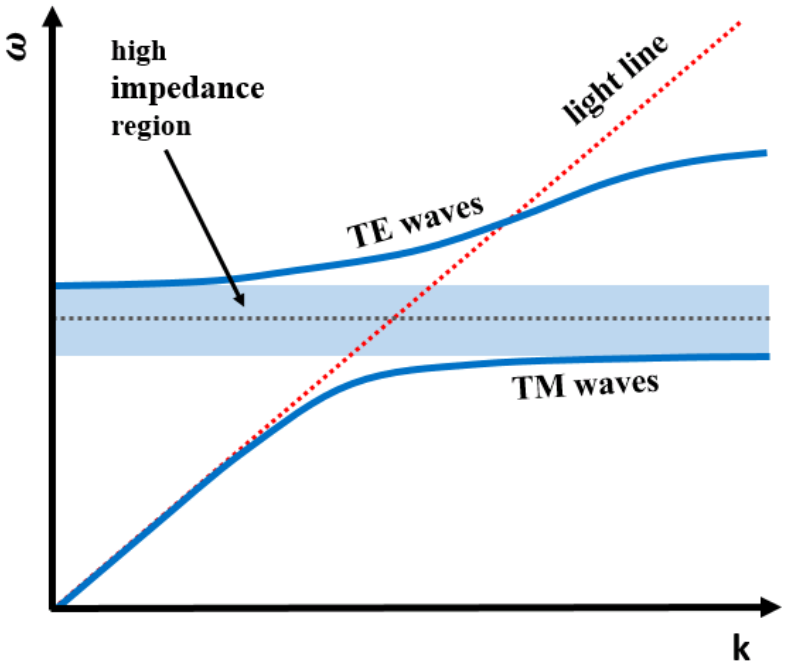

Figure 1.3: Dispersion diagram of the high impedance surface.

1.3 Motivation

Classic examples of microwave absorbers [46], including Dallenbach [47] and Kleinsteuber and Salisbury absorbers [48], are designed with a thickness of one-quarter wavelength, so that the electric field of the incoming wave is maximum at the lossy layer. Metasurface-based absorbers can reduce the thickness of the absorber greatly by using resonant structures to increase the electric field at the surface. HIS based absorbers are studied and used in a lot of applications for its stable response to different incident angles for TM mode. The principle of the absorbing mechanism is shown in Fig. 1.4 for both spatial and surface waves. The waves at the targeting frequency are trapped in the sub-wavelength cavities of the surface due to HIS's band stop property and further dissipated by the resistors at the gaps between neighbouring in form of ohmic loss.

In general, metasurface-based absorbers have advantages of low profile and light

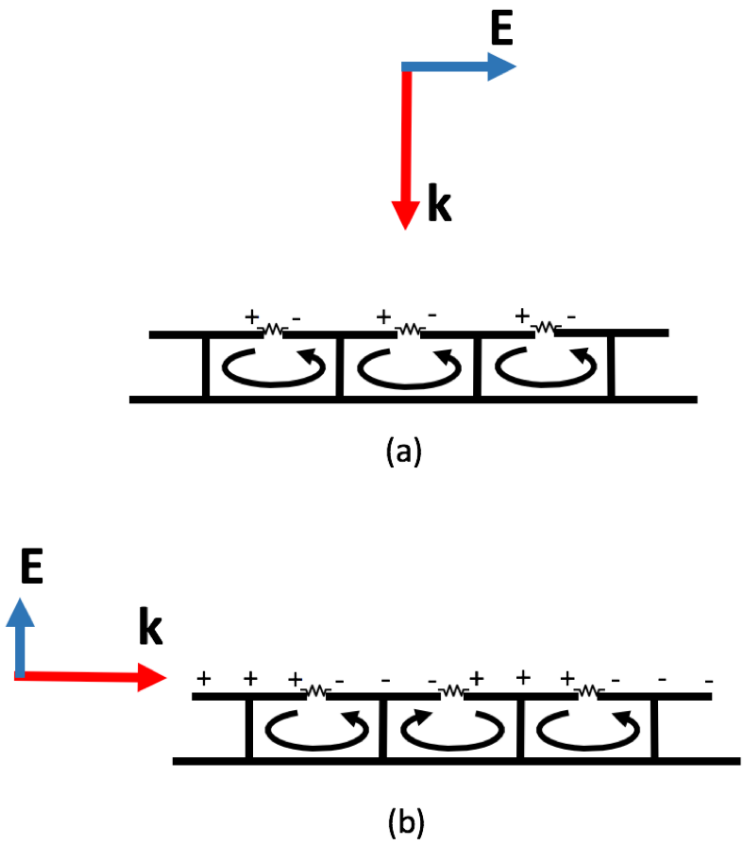

Figure 1.4: Schematic of HIS absorbers.

weight with simple metallic structures. There are, however, limitations in terms of their absorption bandwidth, absorption rate, and air breakdown at high power. TM wave attenuation by lossy dielectric slabs were theoretically studied. The fundamental limitation of the absorption bandwidth of a given passive surface was studied and proved to be directly limited by the thickness of the absorber. Meanwhile, the passive surface has reciprocal and linear response irrelevant with wave propagation directions and input powers, etc. A recent research on metasurface absorbers that targeted but is not bound to these limitations is focusing on active loading and tuning aimed at gaining more flexibility in response to incident waves. By applying active electronics on the passive traditional antennas and surfaces may introduce additional freedom of tuning, non-linearity and mutifunctionality,

thus enhancing the performance comparing with traditional passive solutions.

1.4 Dissertation Organization

The thesis presents the unique properties of the HIS working as a microwave absorber and transmitter by active electronics loading as well as theoretically analysis of the field enhancement of the resonant metasurfaces.

Chapter 1 is an overview of the metasurfaces and their applications. HIS's property and its applications is specifically introduced. Traditional HIS based metasurface absorbers are reviewed and the fundamental limitations of them bring up the motivation that by loading active electronics could enhance their performance.

Chapter 2 studied the electric field enhancement of the resonant metasurface from microwave to near infrared frequencies.

Chapter 3 presents the principle, simulation, fabrication and measurement of the transistor loaded high power switchable and absorption rate tunable metasurface absorbers. An adaptive switchable function is also demonstrated.

Chapter 4 demonstrates a new type of direct DC to RF conversion high power, beam steerable metasurface transmitter by loading avalanche transistors.

Chapter 5 reveals benefits from time and spatial modulation for absorber applications. A non-reciprocal surface wave metasurface absorber is analyzed in simulation with a traveling wave switching the surface.

Chapter 6 summarizes and concludes the thesis, and addresses directions for further research.

Chapter 2

Study of the electric field enhancement in resonant metasurfaces

In this chapter, electric field enhancement of resonant metasurface is studied. The electric field properties (distribution and enhancement) of high impedance surfaces under radiation are studied. It is shown that the electric field enhancement at the gap between metal plates has linear relation with a geometrical factor and is independent of the resonator quality factor. Conditions under which the metasurface can act as an efficient optical absorber are also studied. At the end, wavelengths around 800 nm are suggested for silver (plasmonic) resonators at optical frequencies to maximize the electric field enhancement.

2.1 Overview of Resonant Metasurfaces

Metasurfaces [3] are usually resonant periodic patterns designed to control the interaction between electromagnetic fields and objects [49] . Applications include providing an artificial magnetic conducting boundary [50] , controlling wave scattering properties, and

controlling the surface wave propagation on objects [16, 51–55] . Our study is focused on the high impedance surface (HIS) [44] shown in Fig. 2.1, in which simple rectangular metal plates are connected to the metal ground plane by vertical vias. HISs are mostly known at radio frequencies for their numerious applications in enhancement of antenna performance [56] , surface waves suppression [57] , microwave absorbtion [9] , etc. Besides radio frequencies, the electric field enhancement generated by an HIS has potential applications at infrared (IR) frequencies such as imaging, sensing, photovoltaics, and photo-emission [58–61].

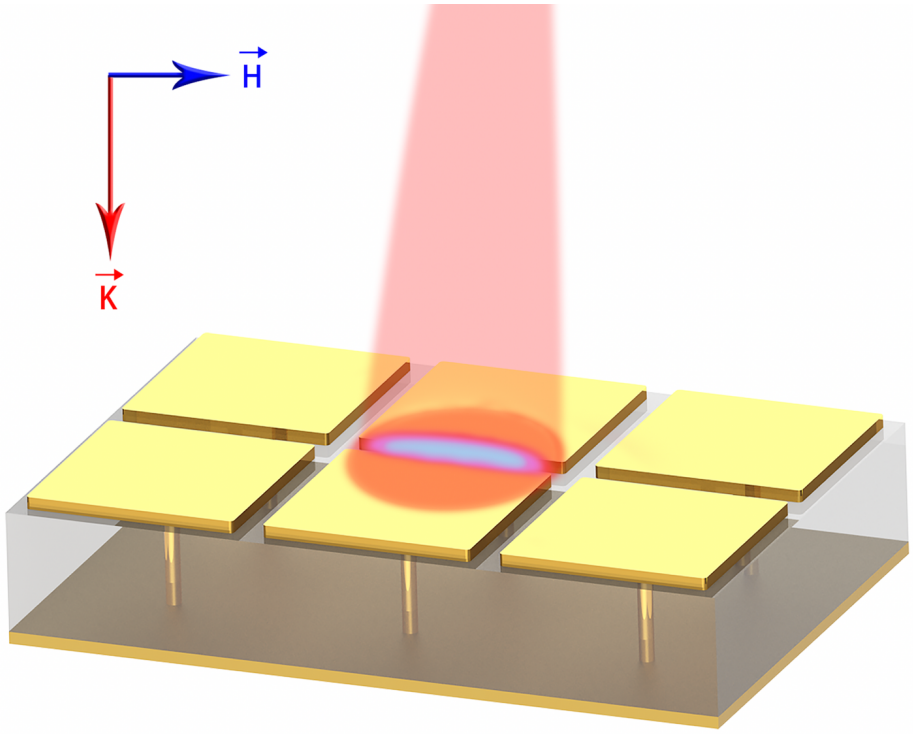

Figure 2.1: Electric field enhancement in high impedance surfaces

At normal incidence, impinging waves do not excite current in vias of the HIS in figure 1, therefore this structure is equivalent to a capacitive array of metallic patches over a ground plane. As a result, the conclusions presented in the followings can likely be applied to a wide range of metasurfaces consisting of metallic patterns separated by narrow gaps,

under normal wave incidence.

Most of the interesting properties of resonant metasurfaces occur at or around their resonance frequency, where there is a comparatively large amount of energy stored inside the structure relative to the incoming wave's power. For some high power applications, such as the engineered ground plane for high power antennas, and high power absorbers [62] , the breakdown electric field of the dielectric is a limiting parameter. Therefore, understanding the location of the highest magnitude of the electric field inside the cavity, and its relation with the incident radiation and the metasurface properties is useful.

In this work, we investigated the relationship between the resonance quality factor, geometrical parameters of the metasurface, and the electric field enhancement factor [63] . We start with microwave frequencies where metals are nearly perfectly conducting sheets. However, lossless metal assumption breaks down at optical frequencies, and it is common to use the well-known experimental data for modeling noble metals [64] . Adapting the Johnson-Christy model for silver, we extended our study to IR frequencies and included effects of loss in our conclusions. At visible optical frequencies (and shorter wavelengths), most of the energy is stored inside the metal rather than the dielectric (of an HIS cavity), and the resonant cavity is formed by the metallic patch itself, that is a plasmonic resonator. Many groups have been studying and reporting the electric field enhancement of plasmonic resonators [65–68] .

In other words, with reasonable dimensions (larger than 1 nm), it is not feasible to implement a metasurface with significant stored energy in its dielectric layer. Therefore, the analytical method introduced in the next section only applies to frequencies where loss is not significant (which is up to near-IR frequencies). The results in this paper are based on full-wave calculations using Ansys HFSS, and throughout the paper we assume a normal

plane wave excitation. Note that some of our conclusions may change for different excitation conditions, and we will briefly discuss this towards the end.

2.2 Electric Field Enhancement of HIS

The electric field enhancement of the HIS could be divided into two parts, which are fields inside of the cavity of the resonant HIS and field enhancement at the gap between neighboring elements, where strongest field occurs.

2.2.1 Electric field enhancement in the cavity

At radio frequencies, the unit cell of the metasurface shown in Fig. 2.1 was modeled in Ansys HFSS as Fig. 2.2 (a). Periodic boundary conditions were imposed using PEC and PMC sheets around the unit cell. Wave port excitation with the appropriate polarization and phase de-embedding to the surface has been performed. This metasurface could be equivalently modeled as a parallel *RLC* circuit, shown in Fig. 2.2 (b), where $R = 377\,\Omega$ represents the radiation loss into the space, L is the inductance due to the separation between the capacitive layer and the ground plane, approximated by μh, where μ is the material permeability and h is the thickness of the substrate, C is the capacitance due to the gaps between the patches, approximated by $\frac{w(\varepsilon_1+\varepsilon_2)}{\pi} cosh^{-1}\left(\frac{a}{g}\right)$ where w is the width of the patch, ε_1 and ε_2 are the permittivities of air and substrate separately, a is the period of the surface and g is the gap width. Note here we are assuming that the capacitance between the patch and the ground is negligible comparing with the capacitance between neighboring patches.

$$Q = \frac{E_{\text{ave}}}{E_{\text{inc}}}, \tag{2.1}$$

The E_{ave} calculations are performed by averaging the electric field over the dielectric volume as well as the metal patch and ground planes at the IR frequency.

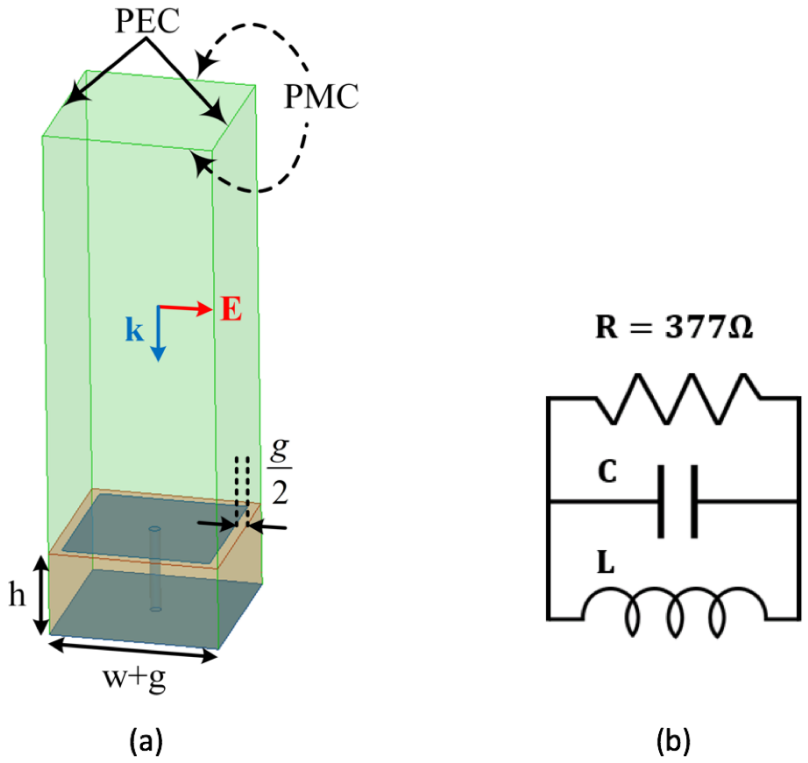

Figure 2.2: The electric field enhancement at the gap (a) Unit cell of the modeled metasurface in HFSS, in which g is the gap size, h is the thickness of the substrate (Rogers 5880 for microwave region, SiO_2 for IR frequencies), w is the width of the patch with material of gold, (b) Equivalent circuit model of high impedance surface at normal incidence (L and C values are defined in [69]).

Since the Q of a parallel RLC is the ratio of the capacitor to the resistor impedances ($Q = \omega_0 RC$), and they share the same applied voltage, it is straightforward to show that $Q = \frac{I_c}{I_s}$, in which I_s is the parallel source current, and I_c is the maximum current across the capacitor at resonance.This suggests that the ratio of the average magnetic/electric field inside the cavity of the HIS to the incident magnetic/electric field scales linearly with Q, i.e.

As a verification, we confirmed equations. (2.1) for several HIS with different quality factors both at microwave and IR frequencies, as shown in Fig. 2.3. For the microwave

frequency (2.4 GHz) simulations, Rogers RT 5880 was used as the substrate, and perfect electric conductor (PEC) sheets were used as the conducting patches and the ground plane. For the IR frequency ($\lambda = 10\,\mu$m) simulations, silicon dioxide (SiO_2) was used as the substrate, and silver patches and ground planes were used with the thickness of 10 nm and 100 nm, respectively. The chosen 100 nm thickness is much greater than the skin depth which is 12 nm at 30 THz. Figure 3 confirms that, at microwave frequencies, Q versus the field enhancement curve is a straight line with the slope of nearly unity, as equations (2.1) predicts. The small discrepancy from the slope of unity is due to the fringing electric fields at the gap which stores a small fraction of the energy in air outside the cavity. Fig. 2.3 also includes three curves for IR frequencies: (a) when Johnson-Christy (JC) permittivity model was used for silver, and the ohmic loss was disregarded by assigning a large conductivity, (b,c) when JC permittivity and conductivity models were used for silver, and the electric field is plotted as a function of both the cavity Q and the radiation Q called Q_{rad} which is calculated as $\eta/\omega_0 L$ from equivalent *RLC* circuits model (i.e. the ohmic loss is disregarded in Q calculations, but is considered in the electric field calculations).

Equations. (2.1) is a general conclusion which is valid regardless of the nature of the loss (radiation or ohmic). This is confirmed in Fig. 2.3 for both lossless and lossy metal patches. However, another interesting observation occurs when we try to adjust the dimensions to achieve higher Q at IR frequencies.As we adjust the cavity dimensions to achieve higher Q_{rad}, the ohmic loss dominates the radiation loss, and the total Q saturates to a maximum value called Q_{max}. Equations(2.1) is valid even in the presence of the ohmic loss, however it is not possible to realize Q (and therefore field enhancement) larger than 5 at IR frequencies for our geometry. As the designed Q_{rad} increases further above 5, the radiation loss decreases and the ohmic loss increases accordingly (since the E_{ave} and hence

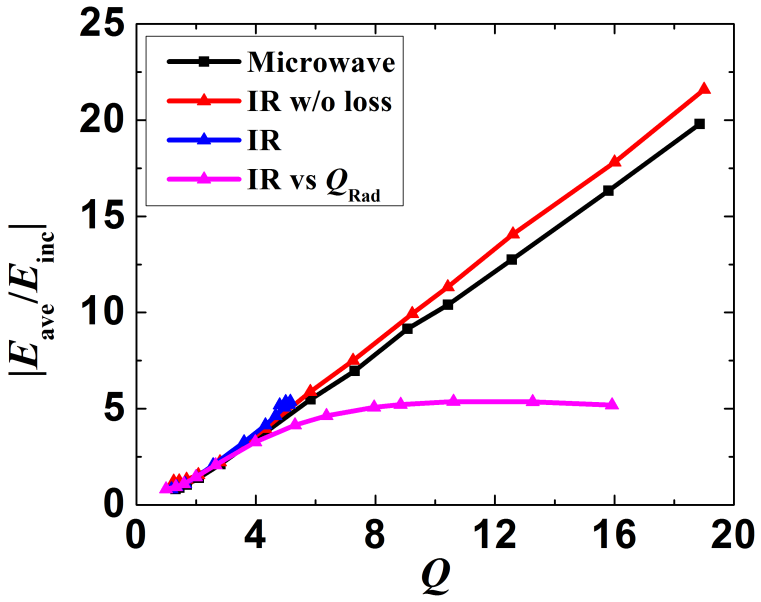

Figure 2.3: Average magnitude of the electric field enhancement inside the cavity as a function of Q.

the stored energy inside the cavity is fixed). This is an important conclusion for designing resonant metasurface absorbers for IR frequencies, in which increasing the ohmic loss is desired. We may maximize the absorption by maximizing the Q_{rad}. This may seem intuitive, but the point is the limited average electric field inside the dielectric which leads to a fixed stored energy inside the structure for $Q_{\text{rad}} > Q_{\text{max}}$, regardless of the Q_{rad} value. In summary, for an IR absorber, (a) a $Q_{\text{rad}} > Q_{\text{max}}$ is desired, and (b) the absorption rate can be readily quantified using the designed Q_{rad}. (Calculation of Q_{rad} is relatively simple as the cavity's materials are assumed lossless.)

Note that the maximum achievable Q_{max} of 5 is for the specific combination of silver and $\lambda = 10\,\mu\text{m}$. This value may change at other wavelengths and using a different metal. Calculation of the Q in the simulations can be performed based on the phase of the reflected wave at resonance, if the cavity is not too lossy, or based on the electric field enhancement regardless of the loss existence in the cavity. The two approaches are explained in detail,

towards the end. Table. 2.1 lists dimensions of the simulated structures in Fig. 2.3 The gap sizes of the structures are fixed at 0.02 λ and thickness of the substrates h is swept to give a wide Q coverage, thus width of the unit cells w is tuned accordingly to keep the resonating frequency unchanged.

Besides the E_{ave}, another interesting quantity is the maximum electric field magnitude inside the cavity, which usually occurs at the gap between patches. This quantity is important for high power applications at microwave wavelengths, besides the numerous applications that the electric field enhancement has at IR and optical frequencies including imaging, spectroscopy and bio-applications [70–72].

2.2.2 Electric field enhancement at the gap

Similar to the E_{ave} inside the cavity, one might intuitively expect cavities with higher Q can provide higher maximum electric fields at the gap between patches (E_{gap}). However, we can easily show that the E_{gap} is independent of the Q, and only depends on a geometrical factor (the ratio of the gap size to the period of the surface, represented as G) and the incident power. In other words, by increasing Q below Q_{max}, the stored energy inside the cavity (and thus the average electric field inside the cavity) will increase, without affecting the maximum electric field at the gap between patches.

Table 2.1: Dimensions of the simulated HISs used in Fig. 2.3 (w and h of the cavities are adjusted according to the Q value)

Material	λ	w	h	g
PEC	122 mm	0.03 λ - 0.325 λ	0.01 λ - 0.16 λ	0.02 λ
Silver (w/o loss)	10 μm	0.052 λ - 0.348λ	0.01 λ - 0.16 λ	0.02 λ
Silver	10 μm	0.055 λ - 0.25λ	0.01 λ - 0.16 λ	0.02 λ

One approach to obtain the E_{gap} is to start with the definition of the Q as,

$$Q = \omega_0 \times \frac{\text{Maximum Stored Energy}}{\text{Lost Power}}, \tag{2.2}$$

in which ω_0 is the radial frequency. At resonance, the stored energy is $U_{\text{stored}} = \frac{1}{2}CV^2$, where C is the edge to edge capacitance of patches, and V is the average voltage across their gaps, related to the electric field by $V = E_{gap} \times g$, where g is the gap size. Although the equation for C is known [69] , we found it more accurate to first find the equivalent inductance using μh, and to convert it to C using $\omega_0 = \frac{1}{\sqrt{LC}}$. Simple manipulation of the equations leads to the stored energy as,

$$U_{\text{Stored}}^{\text{die}} = \frac{1}{2}\frac{E_{\text{gap}}^2 g^2}{\omega_0^2 L} \tag{2.3}$$

In the absence of the ohmic loss, radiation is the only energy dissipation mechanism, which equals the incidence power as,

$$P_{\text{loss}} = P_{\text{inc}} = \frac{[E_0 \times (w+g)]^2}{2\eta}, \tag{2.4}$$

Replacing equations. (2.3) and equations. (2.4) into equations. (2.2), and equating it with the quality factor of a parallel *RLC* circuit ($Q = \frac{R}{\omega_0 L}$) leads to,

$$E_{\text{gap}} = \frac{2(w+g)}{g} \times E_0, \tag{2.5}$$

As the HIS's reflection phase of the resonance frequency is 0, the reflected wave adds up in phase with the incoming wave and forms a standing wave at the space above the surface, which contributes another factor of 2 to the electric field enhancement at the surface

indicated in equations. (2.5) above.

As another important conclusion, equations. (2.5) suggests that the E_{gap} (which is indeed the maximum electric field in the cavity), only depends on the geometrical factor ($G = \frac{w+g}{g}$) and the incident power, independent of the resonator quality factor. This conclusion is accurate if the ohmic loss in the resonator is negligible, which is indeed the case at microwave frequencies. In order to incorporate the ohmic loss, we start with

$$Q = \omega_0 \frac{U_{\text{s}}^{\text{die}} + U_{\text{s}}^{\text{metal}}}{P_{\text{rad}} + P_{\text{ohmic}}}, \tag{2.6}$$

in which $U_{\text{s}}^{\text{die}}$ and $U_{\text{s}}^{\text{metal}}$ are the stored energies in the cavity dielectrics and metals, respectively and P_{rad} and P_{ohmic} are dissipated powers through radiation and ohmic loss, respectively. Since the conductivity of metals is usually high even at near IR wavelengths, it is a reasonable approximation to assume $U_{\text{s}}^{\text{metal}} = \alpha U_{\text{s}}^{\text{die}}$ where α is a coefficient (typically much smaller than unity at RF frequencies).

Then, using $P_{\text{rad}} + P_{\text{ohmic}} = P_{\text{inc}}$ and equations. (2.4) and equations. (2.6),

$$\frac{E_{\text{g}}}{E_0} = 2G \frac{1}{\sqrt{1+\alpha}} \sqrt{\frac{Q}{Q_{\text{rad}}}}, \tag{2.7}$$

In order to interpret equations. (2.7), we use one of the conclusions in Figure 3. That is, depending on the ohmic loss in the cavity, there is a maximum achievable resonance quality factor, Q_{max}. This value in Fig. 2.3 is around 5. Below Q_{max}, the radiation loss dominates the ohmic loss, meaning $Q = Q_{\text{rad}}$. This will simplify equations. (2.7) to equations. (2.5). As we try to increase Q_{rad} by adjusting the cavity dimensions, we reach $Q = Q_{\text{max}}$ due to

the loss, and equations. (2.7) simplifies to,

$$\frac{E_g}{E_0} = 2G\sqrt{\frac{Q_{max}}{Q_{rad}(1+\alpha)}}, \tag{2.8}$$

Based on equations. (2.8), as we adjust the cavity dimensions to achieve higher Q_{rad}, the ratio of E_{gap} to the incident electric field decreases. Moreover, as we reach the Q_{max} for the cavity, the stored energy inside the cavity and the total loss will remain constant. In this regime, increasing Q_{rad} will cause the radiation loss to decrease and the ohmic loss to increase. This is the regime which is useful for designing absorbers, as we concluded from equations. (2.1) as well.

We confirmed equations. (2.8) by simulating the E_{gap} for several HIS geometries as a function of G while Q is constant, and as a function of Q while G is fixed. Fig. 2.4 shows the results for geometries both at microwave and IR frequencies. In Fig. 2.4, we used the same substrates and metal models as Fig. 2.3. The dimensions of the simulated structures in Fig. 2.4 are also summarized in Table. 2.2. Note that, For the Fig. 2.4 (a), in order to keep G constant, w and g were fixed and h was varied to sweepQ_{rad} from 2 to 10. For the Fig. 2.4 (b), when w being fixed, g is swept varying G from 2 to 28, while h is tuned to remain Q_{rad} unchanged.

Table 2.2: Dimensions of simulated HISs used in Fig. 2.4.

Material	λ	w	h	g	(Unless specified) Q
PEC	104 - 141 mm	28.2 mm	1.22 - 12.25 mm	1.22 - 12.25 mm	8
Silver (w/o loss)	7.9 - 15.2 μm	4 μm	0.1 - 1 μm	0.1 - 1 μm	8
Silver	10 μm	0.6 − 2.6 μm	0.1 - 1 μm	0.2 - 2 μm	8

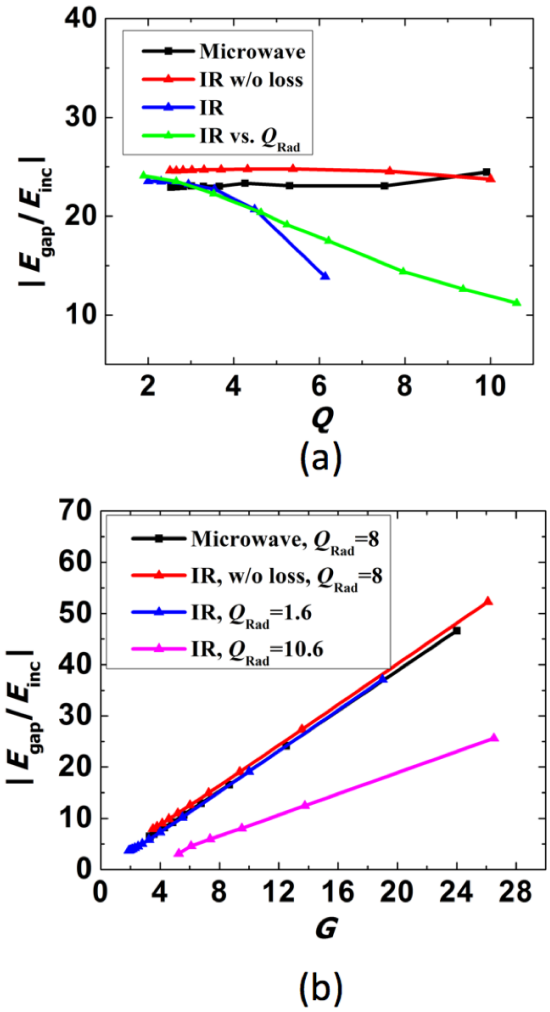

Figure 2.4: The electric field enhancement at the gap (a) as a function of Q, and (b) as a function of G.

Fig. 2.4 confirms that, in case of negligible ohmic loss, the electric field enhancement at the gap scales linearly with the geometrical factor, and is independent of the Q. Similar to Fig. 2.3, the gap field enhancement at IR frequencies in Fig. 2.4 (a) is plotted using JC silver model with and without disregarding the ohmic loss. Fig. 2.4 (a) also confirms that for $Q_{\text{rad}} < 5$, radiation forms the dominant loss mechanism in the HIS, and equations. (2.7) simplifies to equations. (2.5). However, for $Q_{\text{rad}} > 5$, equations. (2.7) can be used, and increasing Q_{rad} decreases the E_{gap}. In other words, minimizing the Q_{rad} and maximizing

G will lead to the maximum E_{gap}. This conclusion is important if one intends to maximize the gap electric field enhancement using HISs with ohmic loss (e.g. at IR and optical wavelengths).

Fig. 2.4 (b) also includes the gap field enhancement assuming silver (with loss) for two Qs smaller and larger than 5. As expected, $Q = 1.6$ yields similar results as the lossless case, while the results of $Q_{\text{rad}} = 10.6$ deviate significantly from the lossless case.

2.3 Further discussion at IR frequencies

In the previous section, there was the assumption of $\alpha \ll 1$ in equations. (2.6) which is valid if the wave does not penetrate considerably into the metallic sheets. This is a good approximation at frequencies lower than deep infrared. The high conductivity of the metal will cause the resonant electric field confinement inside the dielectric region. This confinement is very difficult at near IR and visible optical frequencies (and becomes impossible for shorter wavelengths). As a result, plasmonic resonances inside the metallic patch becomes more important for the optical electric field enhancement.

Several studies have been performed on the electric field enhancement due to plasmonic resonances (for single particles, clusters, arrays, etc) [66, 73, 74] , in which the accuracy of the material models (especially at the boundaries) are crucial. Due to the temporal dispersion of the plasmonic material (such as gold and silver), optimum wavelengths may exist to maximize the electric field enhancement. In this section, based on the results from previous sections, we decide to keep G and Q_{rad} constant as we compare structures with different resonance frequencies. This ensures that radiation loss in different implementations is the same, and the field enhancement at the gap is only dependent on the ohmic loss (since G is also a constant). Note that the value of the metal conductivity at different frequencies is

not a good criteria for loss evaluations. In fact, both zero and infinite conductivities lead to a zero loss value. Depending on the geometry and electric field distribution, specific (limited) conductivity values lead to a large ohmic loss. For example, Fig. 2.5 shows the electric field enhancement of an HIS with $Q_{\text{rad}} = 7$ and $G = 13.8$, as the conductivity of the metal sheets is varied (artificially). There is a value of the conductivity which minimizes the field enhancement (at which the ohmic loss is maximum). The conductivity and the relative permittivity of silver (JC model) are also shown in Fig. 2.5 (b). In other words, the higher conductivity of silver at lower wavelengths in Fig. 2.5 (a) does not lead to a lower ohmic loss.

Fig. 2.6 shows the electric field enhancement of HISs with $Q_{\text{rad}} = 2$ and $G = 2$. Based on Fig. 2.6, there is a clear peak in the field enhancement at wavelengths around 800 nm. Although Fig. 2.6 is obtained based on a specific geometry, it is possible to generalize the conclusion and expect silver material to provide maximum plasmonic field enhancement at wavelength around 800 nm. This conclusion may be useful in designing plasmonic resonators to achieve high electric field enhancement since their resonance frequency can be adjusted by their physical dimensions. Note that the field enhancement in Fig. 2.6 is small since we used a low $Q_{\text{rad}} = 7$ to ensure electric field confinement in the dielectric (rather than the metal). This was only done to increase the accuracy in our comparison. The field enhancement of different HISs with $Q_{\text{rad}} = 10$ and $G = 14$ are also plotted in Fig. 2.7 for IR wavelengths. The visible wavelengths have been removed from this figure due to the lack of sufficient accuracy.

In all of the geometries in Fig. 2.5 and Fig. 2.6, the thickness of the metal patch and the ground sheet are fixed at 5 nm and 200 nm, respectively. The ground plane is thick enough to remain 10 times larger than the skin depth in the whole wavelength span. The

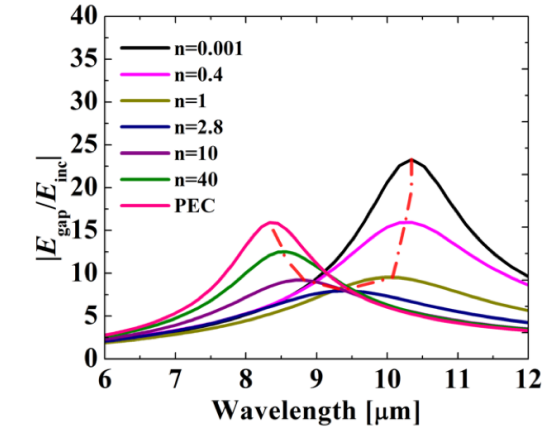

Figure 2.5: (a) $E_{\text{gap}}/E_{\text{inc}}$ of a silver HIS with the conductivity $\sigma = n \times \sigma_{\text{Ag}}$, where σ_{Ag} is the conductivity of silver at 30 THz. The HIS dielectric is SiO_2, (b) Silver conductivity and permittivity as a function of wavelength using JC model.

gap size and the thickness of the SiO_2 substrate are also maintained larger than 1 nm to be realistic. The radiation quality factor is calculated using $\eta/\omega_0 L$, which can be derived from the equivalent parallel *RLC* circuit.

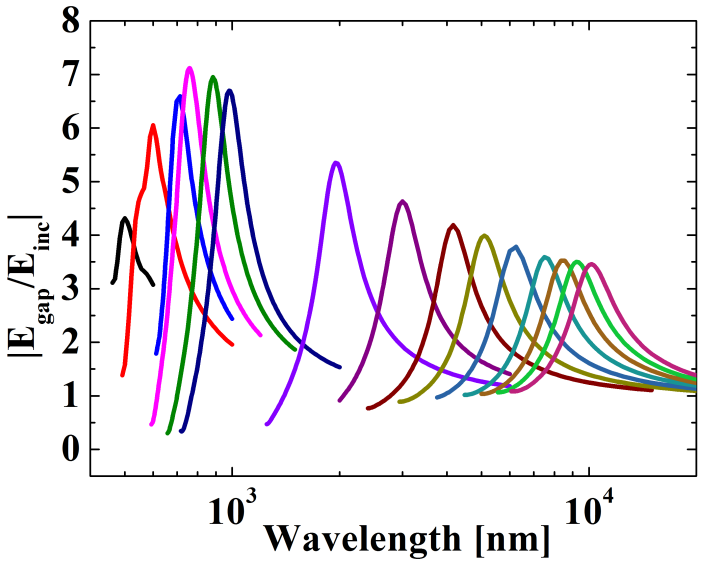

Figure 2.6: $E_{\text{gap}}/E_{\text{inc}}$of silver HISs at different IR and visible wavelengths. Q and G for all of the HISs are both fixed at 2.

2.4 Q calculation discussion

There are multiple ways of calculating the quality factor for a resonant structure. One popular way of defining the resonance quality factor is by using the bandwidth, $Q = \frac{1}{FBW}$, in which FBW is the fractional bandwidth of the resonant structure. This fractional bandwidth can be easily found from the 3 dB bandwidth of the magnitude of electric field at the gap, as shown in Fig. 2.8. If the geometry is lossless, or has negligible ohmic loss, the fractional bandwidth can also be found from the -90^o to $+90^o$ reflection phase bandwidth at the surface with a plane wave excitation.The later method is faster and easier, however its accuracy decreases as the ohmic loss increases. This can be easily verified from the circuit model of a resonator including loss. Fig. 2.8 (a) shows how the two methods lead to the same FBW for a lossless structure with dimensions $w = 28.2\,\text{mm}$, $g = 2.45\,\text{mm}$ and $h = 4.9\,\text{mm}$, and Fig. 2.8 (b) show the reflection phase of the same structure as its metal conductivity is varied.Except for the very high and very low conductivity values, the reflection phase does

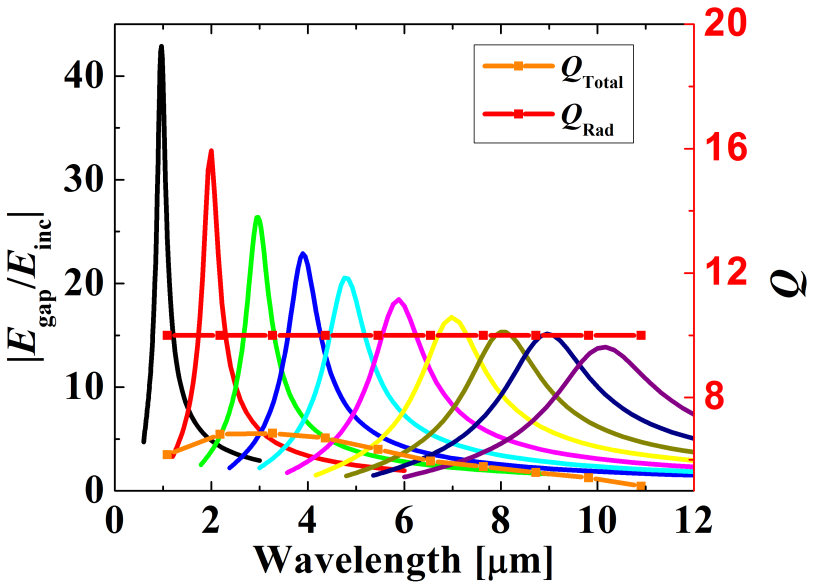

Figure 2.7: $E_{\text{gap}}/E_{\text{inc}}$ of silver HISs at different IR wavelengths. Q and G for all of the HISs are fixed at 10 and 14, respectively.

not lead to an accurate fractional bandwidth.

2.5 Conclusion

The electric field enhancement inside a resonant metasurface was studied at different frequencies. It was shown that the field enhancement at the gap between metal plates with negligible ohmic loss (such as at microwave frequencies) has linear relation with a geometrical factor (G) and is independent of the quality factor (Q_{rad}). In case the metal is moderately lossy (such as at IR wavelengths), increasing Q_{rad} causes higher ohmic loss which decreases the electric field at the gap. At the visible optical frequency range, wavelengths around 800 nm seems to provide the lowest ohmic loss and hence the maximum electric field enhancement at the gap. These conclusions are useful for a wide variety of applications, such as for nonlinear absorbers [75,76] , ground planes for high power antennas or microwave sources, and optical structures which require high field enhancement [77–79].

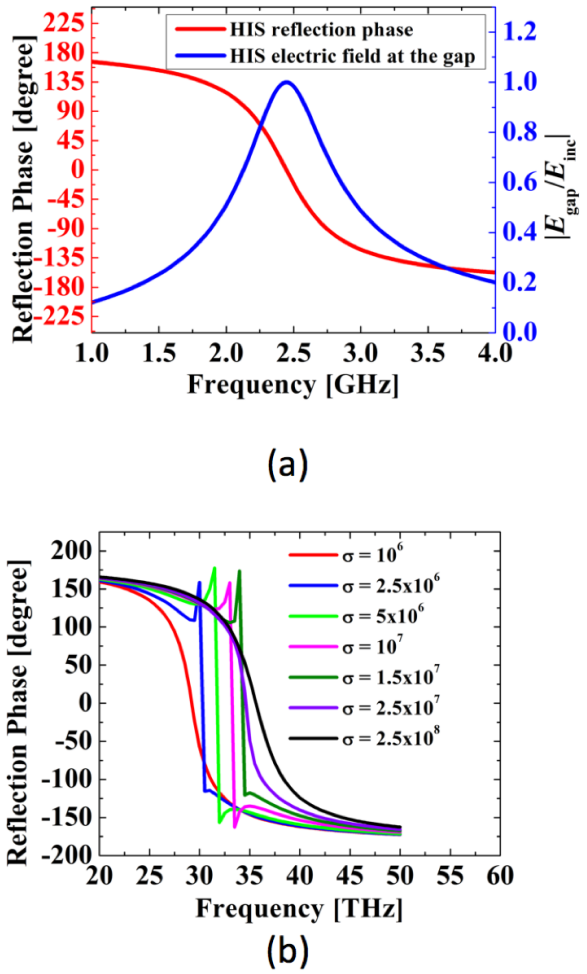

Figure 2.8: (a) The FBW of a lossless HIS using the reflection phase and the electric field at the gap, (b) the reflection phase of an HIS with different metal conductivities and the dielectric permittivity is 1.75

Chapter 2 is based on and is mostly a reprint of the following paper: **A. Li**, E. Forati, and D. Sievenpiper, "Study of Electric Field Enhancement in Resonant Metasurfaces", *Journal of Optics* **19**, 125104, 2017. The dissertation author was the primary author of the work in this chapter, and the co-author has approved the use of the material for this dissertation.

Chapter 3

High Power Transistor Loaded Active Metasurface Absorber

In this chapter, a switchable and tunable high power active metasurface absorber is studied. High power signals traveling along the surface of the shielding of transmitter systems may leak into the system through openings between connecting parts and cause damage to vulnerable electronic devices. This problem could be alleviated by implementing lossy coatings or recently developed passive power-dependent nonlinear surfaces. However, these solutions will either suppress the performance of the electromagnetic devices being shielded or be highly power dependent. Applying transistors creates an active non-linear meta-surface that can allow the absorption of the surface to be directly controlled by the system, or tuned in response to the local power level using feedback control. This can provide a sharp absorption response with a wide range of controllable power threshold. Different absorption rates at the same power level can also be achieved by applying different biasing to the transistors. In this paper, the first transistor based, thin, switchable and tunable high power surface wave absorber is proposed with full wave and circuit co-simulation

analysis as well as waveguide and anechoic chamber measurement.

3.1 Introduction and Motivation

Microwave absorbers are widely studied because of their absorbing abilities that can suppress transmission and reduce reflection or scattering for radar absorber applications [80–83]. Another important role that microwave absorbers are playing is to absorb energy of incoming signals to protect sensitive electronic devices from being disrupted or even damaged when input power is high enough, and couples into the system through apertures on the metallic body that support the system.

One approach to mitigating high power microwaves is to deploy conventional absorbers on the surface of the object to alleviate scattering or energy transmission. However, this coating material is usually expensive, thick and bulky, and it may have negative effects on the performance of the front-end of shielded communication system, like transmit or receive antennas.

Frequency selective surfaces (FSS) and metasurfaces working as microwave absorbers have been proposed and applied in many studies [9, 84–90], because these subwavelength periodic metallic units have advantages of low loss, low cost, low profile and unique high performance in various applications such as conformal antennas [45], wavefront engineering and advanced imaging systems. For metamaterial perfect absorber (MPA), related works have been done in both RF and optical frequencies in applications of cloaking as well as energy absorption. The conventional metasurface absorbers are generally passive and have the same response regardless of the incident power and waveform, thus may be limited in applications when devices to be shielded are working at the same absorbing frequency bands. Therefore, tunable absorbers [12, 91, 92] are studied and further research has

been carried out by loading the metasurface with lumped elements and diodes to introduce non-linearity [11, 14, 46, 75, 93–98]. This non-linearity could either be power-dependent or waveform-dependent or both, enabling the surface to respond differently to various incoming signals. The active frequency selective absorbers could be tuned to absorb at different frequencies by tuning the biasing of the PIN diode to achieve a wide band absorber in normal direction. However, a large area of active absorber that may require thousands of PIN diodes would draw a large amount of current, which may make it impractical. On the other hand, as diodes only turn on when the voltages across them are greater than the turn-on thresholds (typically 0.4 V for schottky diodes and 0.7 V for PIN diode) conventional diode based nonlinear absorbers are limited to specific power ranges.

In this work, we propose the first transistor based tunable and switchable surface wave absorbing metasurface. It provides surface wave suppression to protect electronic devices from leakage of high power signals or surface currents through discontinuities in the enclosing structure, as indicated in Fig. 3.1 Compared to the diode-based absorber, the use of field-effect transistors (FET), gives an additional degree of freedom because absorption is controlled through the gate voltage, rather than the diode turn-on voltage, making this surface switchable and tunable at both low and high microwave power levels. In other words, this transistor based absorbing surface could be turned on or off at both high power for protection purposes and at low power for scattering or communication purposes. Furthermore, the absorption rate can be easily tuned by adjusting the bias voltage of the transistors, which will be introduced in this paper. Comparing with adopting diodes for switching purpose, FETs can be maintained in a particular tuning state with no static power draw, since they are voltage controlled. On the other hand, FET's drain-source channel is symmetric, which allow signals conducting in both ways, the active absorbers we are proposing could be

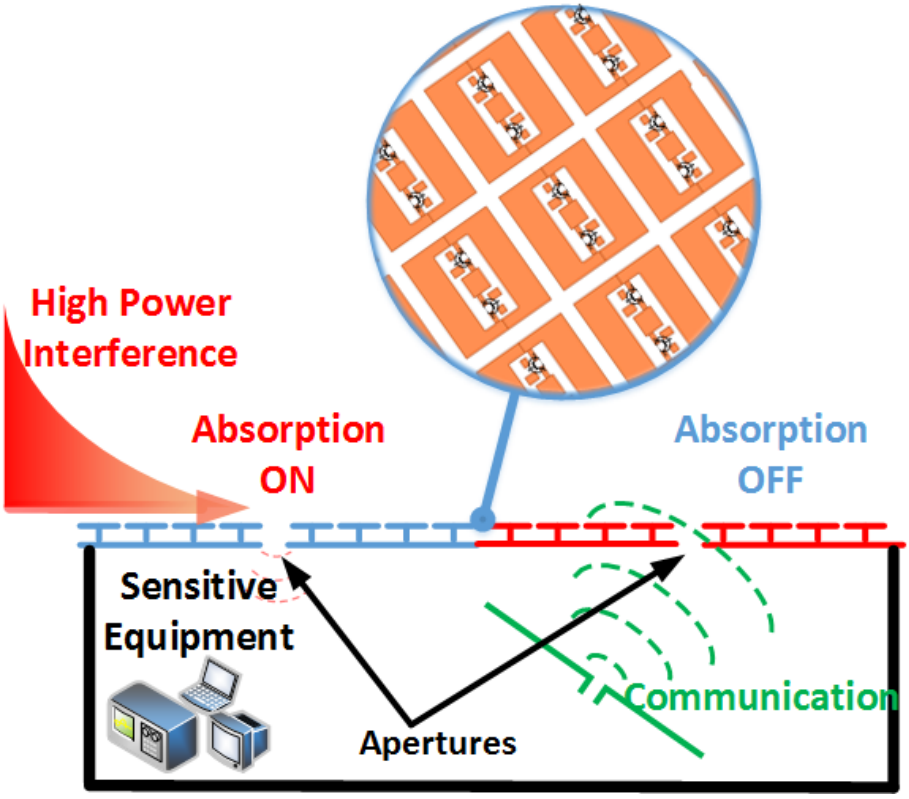

Figure 3.1: Conductive body covered with transistor based absorbing surface which can protect sensitive equipment from being damaged by high power interference by turning on the absorber through transistors, meanwhile it can sustain communication when the absorbing surface is turned off.

tuned without damaging its linearity. We first demonstrate the absorbing response of the transistor loaded metasurface with electromagnetic and circuit co-simulation, and then show the switching and tuning capability of the surface in a waveguide measurement. In order to further verify the surface current suppression performance, we demonstrate a large array of this surface with a slit in the middle representing the discontinuity of the surface. A large difference in attenuation between ON and OFF state leakage through the slit is observed in the chamber measurement, which matches well with the difference of the magnitude of the radiation pattern in the ON and OFF states. Compared with conventional nonlinear

absorbers, this transistor-based absorbing surface has a sharper response to the amplitude of the input power level. Finally, we demonstrate that we can provide feedback using a power sensor and LabVIEW based control system to provide an even sharper response, turning on the absorption at any prescribed leakage power level.

3.2 Non-linear Absorber Analysis

The mechanism of this absorbing surface is based on the surface wave suppression property of the HIS. It is composed of periodic sub-wavelength metallic patches with centered vias connecting the patches to the bottom ground plane. It has a bandgap between the transverse magnetic (TM) and transverse electric (TE) surface wave modes, and it does not support surface waves within the forbidden gap. Near the band edge, incoming fields are enhanced by the resonance of the surface [63], and if losses are included the wave can be highly attenuated. If such a material is deployed on the outer enclosure of an object to be protected, it can effectively suppress surface currents, and thereby minimize leakage through apertures, openings, or discontinuities in the enclosure.

The surface can be modeled as a paralle *RLC* circuit where the resonance frequency is $\omega_0 = \frac{1}{\sqrt{LC}}$ in which L is the equivalent inductance determined by the thickness of the surface, and C is the equivalent capacitance of the gap between neighboring patches. The quality factor (Q) of this HIS resonator is related to the gap resistance. A parallel *RLC* circuit's Q is represented as $Q = \frac{R}{\omega_0 L}$, in which R is the resistance at the gap, and, where is the permeability of the substrate, and is its thickness. When the surface is illuminated with microwaves, the concentration of charge across the gap also leads to current through the resistance, causing absorption. Further this R can be tuned to adjust the absorption rate and bandwidth, as it affects the quality factor of the resonators that make up the surface.

In order to make this absorbing metasurface tunable and switchable, we introduce active components in the form of transistors at the vias of the metallic patches. This will allow the topology of the surface to be manually transformed, thus having different absorption response to incoming waves shown in Fig. 3.2 (a). We connect the center of the via to the drain of the FET transistor and connect the source of the transistor to the ground plane. The drain to source channel can be turned on and off by applying different DC biases (positive or negative bias respectively depending on the threshold voltage of the transistor). For an ideal transistor, the drain to source resistance is zero in the ON state (positive gate biasing), which connects the via to the ground, creating a high impedance surface and allowing high absorption of surface waves. On the contrary, in the OFF state (negative gate biasing), the drain to source channel resistance for an ideal transistor is infinite, and it appears as an open circuit, which disconnects the via from the ground. This transforms the surface from an HIS into simple array of periodic patches backed with a conducting ground plane, and eliminating the resonance as seen by surface waves. In this state, the structure is essentially a conductor-backed frequency selective surface [6], which has a much higher resonance frequency, and thus lower loss within the band of interest. Hence, it will support surface wave propagation with very low absorption. In addition, when the gates of the transistors are biased with a voltage level between ON and OFF states, the drain to source channel will show different equivalent resistances, which changes the quality factor of the surface and adjusts its absorption. In this case, a tunable absorption rate will be observed with different gate biasing voltages.

Besides the topology mentioned above, another transistor-based switchable and tunable surface is represented in Fig. 3.2 (b). Instead of at the vias, transistors are placed at the gaps between the plates, in parallel with the gap resistance. In this structure, the drain to

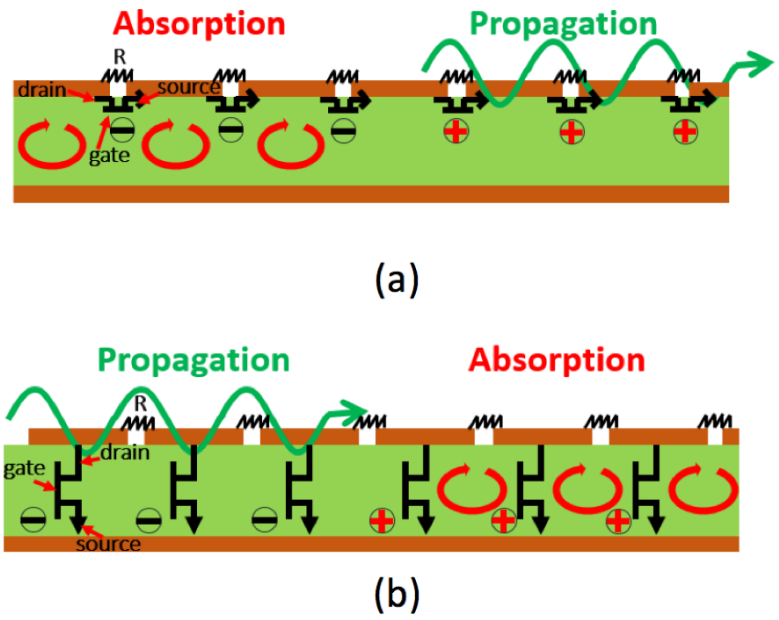

Figure 3.2: Transistor-loaded metasurface in the ON and OFF states for surface wave absorption. (a) Transistors loaded at the via. (b) Transistors loaded at the gap.

source channel can also be controlled by the bias voltage at the gate. For the transistor's OFF state (negative gate biasing), the drain to source channels are turned off and the surface is highly absorbing. For the transistor's ON state (positive gate biasing), the drain to source channels are shorting the resistors at the gaps and connecting all the top patches together, which makes surface look highly conductive, and thus reducing absorption. Similar tunable states are expected to be seen as with the former topology. The following chapter will discuss about the simulation and measurement of these two structures.

3.3 Co-simulation and Waveguide Measurement

Two topologies (A and B) of the transistor loaded HISs are designed and co-simulated with HFSS and Ansoft Designer. The elements of topology A and B are implemented as shown in Fig. 3.3 (a) and Fig. 3.3 (b) respectively. For topology A, to avoid positioning the

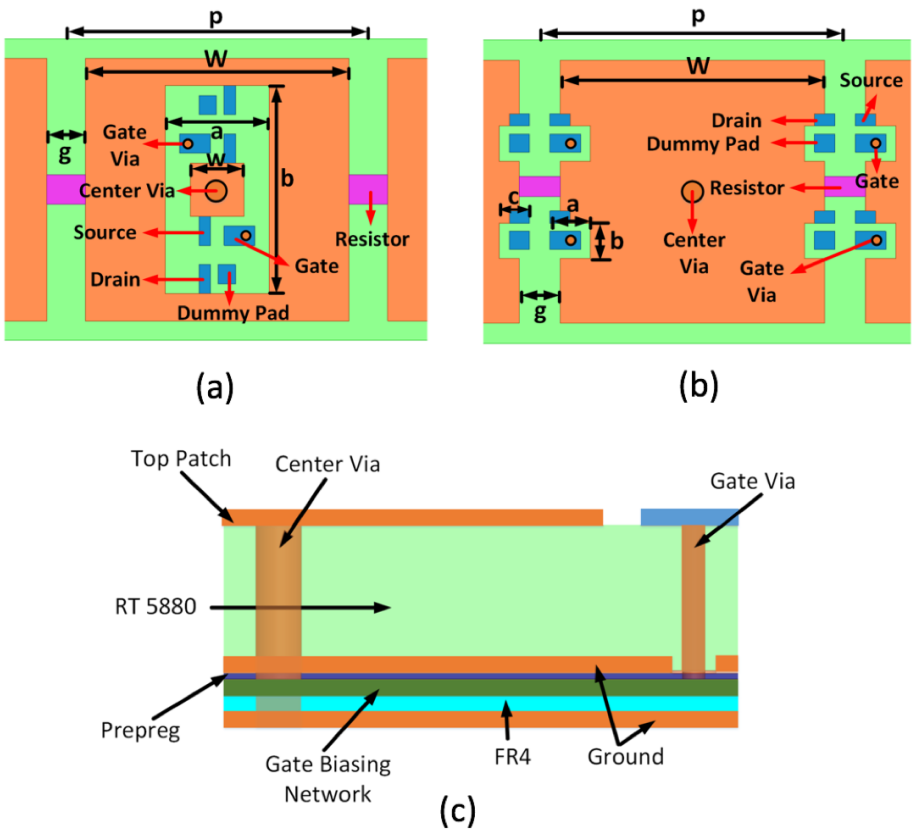

Figure 3.3: The element top view of the two topologies in which, orange color metal represents the surface patch, while blue metals are pad for transistors (NE3503M04 is used here) and purple rectangular represents the position of the 2 $k\Omega$ gap resistors. (a) Topology A with a pair of transistors at the center vias, in which p=15.6, W=13.6, g=2, a=5.38, b=10.76, w=2.76 (all in mm). Note p is the period of the unit cell. (b) Topology B with a pair of transistors at the gap in which, p=17.5, W=15.5, g=2, a=2, b=1.75, c=1.5 (all in mm). Note p is the period of the unit cell. (c) Side stack view of the structure for both topology A and B.

transistors inside the substrate, we designed a pair of transistors on the surface to connect their drains to the outer ring of each patch and their source to the inner pad which is attached to the via. The gates of the transistors are connected through additional vias from top to the biasing network layer, which provides bias voltage to the gates of all the transistors simultaneously in order to control the whole surface's electromagnetic properties. The 2 $k\Omega$ resistors are placed at the gap between neighboring elements, aligned with the E field direction at the gap which is perpendicular to the edge of the units along the surface (k

direction in Fig. 3.4). For topology B, a pair of transistors are placed at the gap in parallel with the resistor, their drains and sources are connected to the neighboring elements. The gates are connected through vias from top to the biasing network layer. The centers of the elements of both A and B are shorted to the ground layer with a through hole plated via with radius 0.5 mm. Rogers RT5880 with thickness of 3.125 mm is used as the substrate for both topologies. For the biasing circuits layer, we used 0.127 mm thick FR4 as a substrate. The side view of the stack is shown in Fig. 3.3 (c), which applies to both A and B topologies.

3.3.1 EM/Circuit Co-simulation

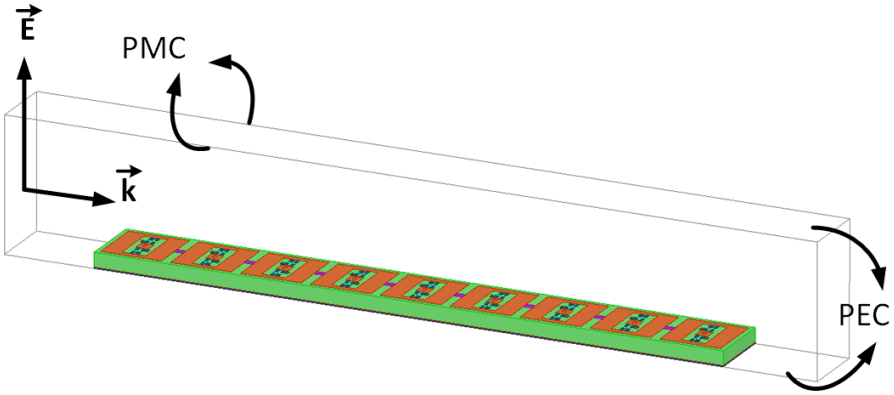

Figure 3.4: HFSS simulation model of nine unit cells with top and bottom PEC walls and two side PMC walls as a two-dimensional array when TM wave excited.

In order to evaluate the absorption performance of the proposed two topologies, we here implemented HFSS's full wave simulation [93] of an array of nine elements with periodic boundaries for two side walls excited by two wave ports at the left and right side, and PEC boundary for top and bottom walls when TM excited, shown in Fig. 3.4. As the target center absorbing frequency is 2.2 GHz which lies in the frequency range of waveguide WR-430, the same height (54.61 mm) of the air box is chosen to be aligned with real waveguide measurements. For TM excitation, the top and bottom of the air box is assigned

to be PEC boundary and the two side walls are assigned to be PMC (periodic boundary for TM excitation) thus representing the structure located in an ideal TEM waveguide. Lumped ports are assigned for gap resistors and transistors drain and source channels at their intended locations.

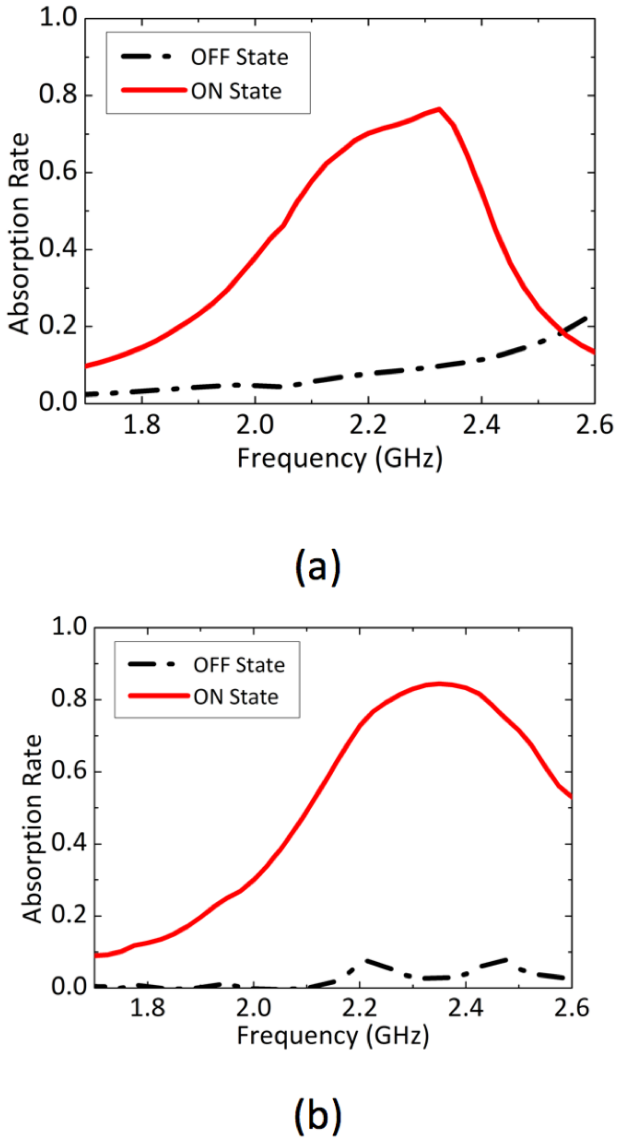

Figure 3.5: Co-simulation results of the switchable absorption results of the non-linear absorbers (a) Topology A (-3 V for OFF state, 1 V for ON state). (b) Topology B (-3 V for ON state, 1 V for OFF state).

Full wave simulation provides the S-parameter matrix of the passive part of the

absorber, from which when imported to circuit simulators (ADS or Ansoft Designer), then connected with transistors and resistors to the corresponding lumped ports. Two wave ports are connected to microwave excitation and receiving port respectively with impedance set to be characteristic impedance of the wave port of the model. Absorption performance of the surface can be studied in time domain circuit simulations. We include a full SPICE model of the transistor (NE3503M04) including parasitics and the resistors in the transient simulation. We can easily derive the absorption rate of this surface wave absorber by,

$$Abs(f) = 1 - T(f) - R(f), \tag{3.1}$$

in which Abs is the absorption rate, T and R are the frequency dependent transmitted power and reflected power respectively. In circuit simulations, we bias the gate of the transistors in circuit simulators to turn the transistors on and off by providing positive (0$\sim$1 V) and negative (-3 V) biases respectively. The switchable absorber's simulated results are shown in Fig. 3.5 (a) and Fig. 3.5 (b). For both topologies, we could see over 80% peak absorption in the ON state and less than 10% absorption rate in the OFF state, showing good switching ability.

3.3.2 Waveguide Measurement

With the optimized structure, we fabricated a small array indicated in Fig. 3.6 (a) and Fig. 3.6 (b) for both topology A (six by nine unit cells) and B (five by eight unit cells) with dimensions the same as indicated in Fig. 3.3 (a) and Fig. 3.3 (b) respectively and measured in the standard WR-430 TE waveguide. Note that TEM waveguide is used in simulation only for simplification of simulations. Power amplifiers (Ophir 5022 and 5193) are used to provide different levels of input power. Several power meters (Agilent N1911A) are used to

detect the incident, reflected and transmitted power at the waveguide in real-time, with the measurement controlled by LabVIEW. The measurement set up is shown in Fig. 3.6 (c).

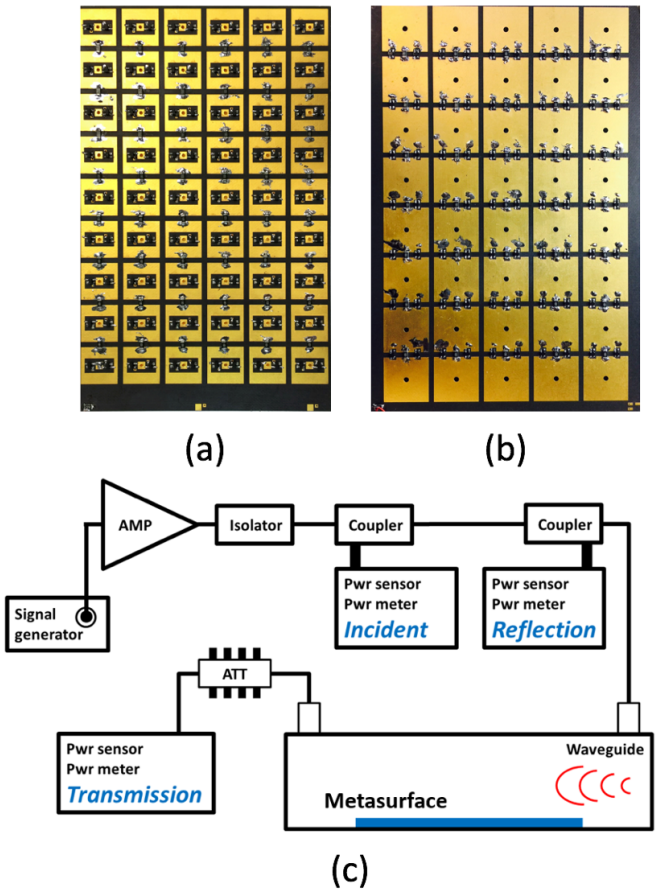

Figure 3.6: Small absorbing array fabrication for waveguide measurements (a) Fabrication of topology A. (b) Fabrication of topology B. (c) Waveguide time-domain measurement setup.

The measured absorption rate curves for the two topologies under different input power levels are plotted in Fig. 3.7 (a) and Fig. 3.7 (b). At low power level (less than 10 mW), we could observe a large absorption difference between ON and OFF states of both topologies. Note that at the measured abosrption rate curves of input power less than 10 mW shares the same one as 10 mW case. At the frequencies of interest, near 2.2 GHz, the surface has more than 80% absorption rate in the ON state and lower than 20% absorption

rate in the OFF state. We could observe that for ON states, the absorption rate begins to drop as power is increased. This is because with higher input power, the drain to source channel current begins to saturate, causing the absorption rate to drop. However we could still see more than 50% absorption for topology A at 2.2 GHz and a peak abosrption rate over 60% at 2.35 GHz with 1 W input power, which equals 168 W/m2. This power density is calculated from input power (1 W) divided by the area of the waveguide(0.006 m2 for WR-430). The measured OFF states of different input powers share the same curve (black curve in Fig. 3.7), since the transistor's drain-source channel is off all the time with the tested input power range. For Topology B, at 5 W (838 W/m2) input power we could still see more than 60% absorption at the frequcncy of interest between 2 GHz to 2.2 GHz. The power handling ablity is higher because this topology's absorbing state is in transistor's OFF state, where current saturation is not a critical issue. For topology A, to achieve higher power performance, we could change the current transistors with ones having higher saturation drain current. This limitation will be discussed further in the following section.

Besides the switching ability of the absorber, the absorption rate can also be tuned to middle states between ON and OFF by applying different bias voltages (-1 V 0 V) to the gates. With different bias voltages, the drain to source equivalent impedance is changed accordingly (higher bias voltages gives a lower channel impedance), further affecting the resonance of the surface and changing the absorption rate. This tunable absorption of topology A is measured and shown in Fig. 3.7 (c). Note that for bias voltage greater than 0 V (drain-source channel fully ON) and less than -1 V (drain-source channel fully OFF), the measured absorption rate curves are identical to 0 V bias one and -1 V bias one respectively.

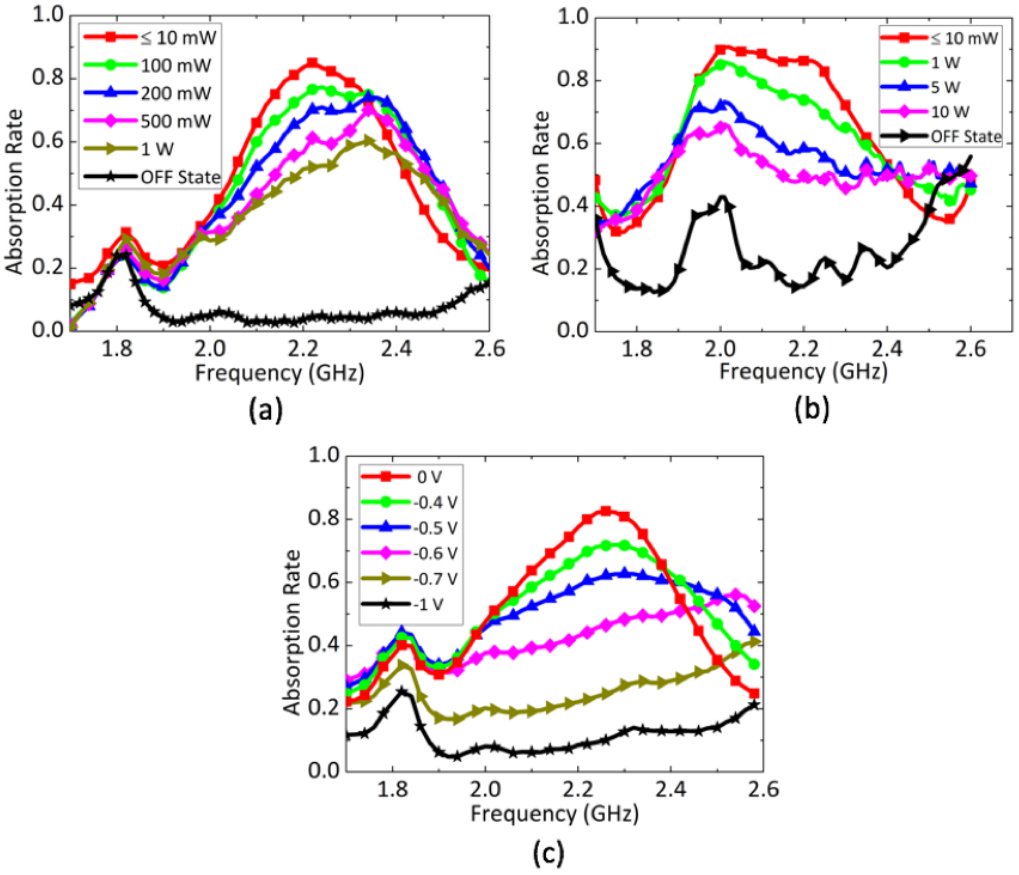

Figure 3.7: Waveguide measurement results (a) Absorption rate at ON and OFF states of topology A with different levels of input power. (b) Absorption rate at ON and OFF states of topology B with different levels of input power. (c) Measured tunable absorption rate of topology A with different gate biasing.

3.3.3 Measurement Result Discussion

For topology A's waveguide measurement, we could see a small peak at 1.8 GHz at both OFF and ON states as well as those intermediate states. That is caused by the gate vias of the transistors, which introduces another additional resonance. This could be removed or addressed by adjusting the positions of the vias. Additionally, for the waveguide measurement, as input power increases, there is a drop of absorption rate in the on state, seen in Fig. 3.7 (a). The reason for this is because when transistors' gates are positively biased, the drain to source channel is turned on but this channel's current will saturate at

some input power. In other words, at comparatively low power, the transistors are working in the linear region which yields a small channel resistance, but at high power they are working in the saturation region which increases the channel resistance significantly and reduces the quality factor of the surface. We further verified this through simulations by assigning RLC boundaries connecting topology A's outer rings to the vias. When the resistance increases, a drop of absorption could be observed as expected, indicated in Fig. 3.8. This problem could be solved by applying higher power transistors at the via to enable higher power applications. Note that for topology A when using NE3503M04 as the switching transistor, with 1 W (168 W/m2) input power to the WR-430, we could still achieve more than 60% peak absorption at 2.35 GHz and over 50% of absorption at 2.2 GHz.

Topology B is another way to solve the saturation problem, since the absorber is in the ON state when the transistors are negatively biased. This topology may instead be limited by the breakdown voltage between drain and source, but this would occur at even higher power levels. This could be easily seen from Fig. 3.7 (b), that when input power is 5 W (838 W/m2), more than 70% peak absorption at 2 GHz and 60% of absorption at 2.2 GHz could still be achieved. However, from topology B's measurement, we observed that compared with the simulated results, the OFF state's absorption rate is higher than expected. This is because in the OFF state, when the transistors are positively biased, they are not ideally shorted, instead they will show some drain to source resistance and capacitance. Unlike placing the transistors at the vias, this parasitic capacitance and channel resistance influence the surface more since the field is mostly concentrated at the gap between neighboring elements where the transistors are placed. This issue could be addressed by implementing smaller transistors at the gap with smaller parasitics.

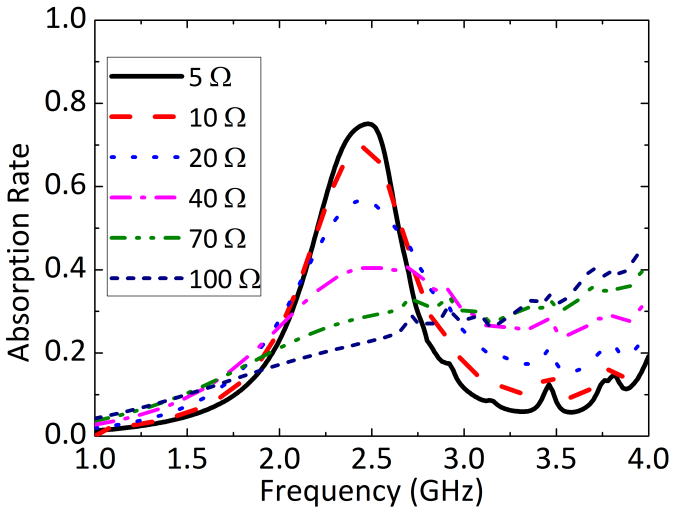

Figure 3.8: Waveguide measurement results (a) Absorption rate at ON and OFF states of topology A with different levels of input power. (b) Absorption rate at ON and OFF states of topology B with different levels of input power. (c) Measured tunable absorption rate of topology A with different gate biasing.

3.4 Large Panel Demonstration

A large panel of the absorber of topology A is fabricated in order to test the surface current suppression and absorbing abilities in a realistic scenario in our far-field chamber. The fabricated array consists of 400 unit cells (25 by 16 cells, with length 395 mm and width 254 mm) and a slit in the middle of the board with width 2.54 mm and length 56 mm. The purpose of that slit is to allow for leakage of microwave power and thus to test the absorber's tunable and switchable properties and its ability to suppress leakage. The slit is designed to work as a slot antenna at 2.2 GHz with the absorbing surface, which allows energy to couple through the slit in the OFF state. We expect to see large attenuation of the leakage power in the absorber's ON state.

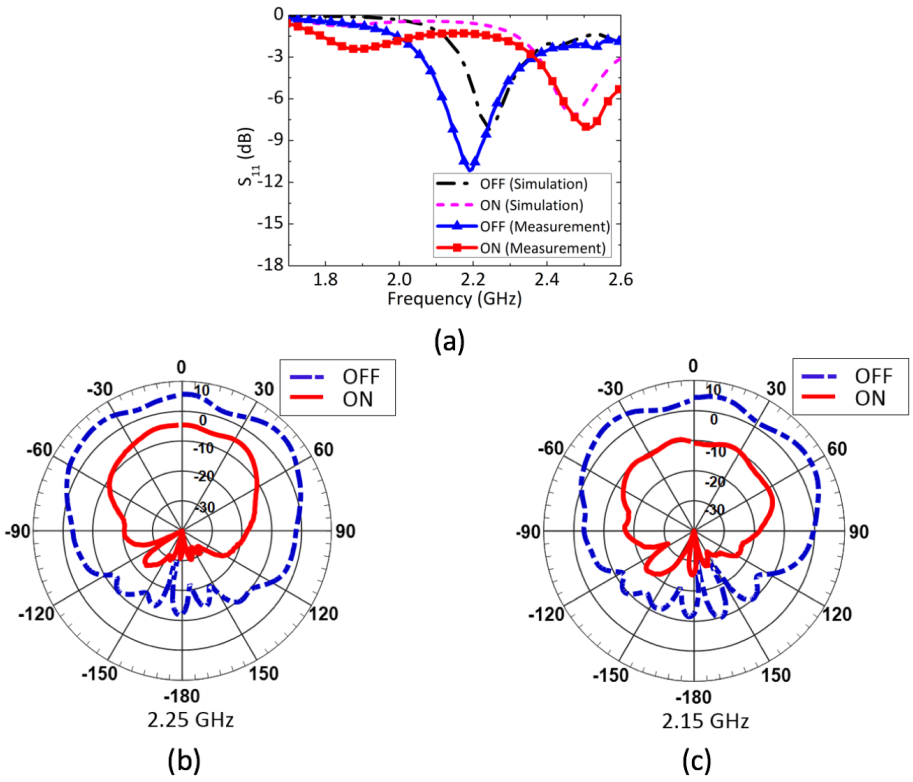

Figure 3.9: (a) Measured vs. Simulated S11 of the slit at both on and off states. (b) Radiation pattern (E-plane) at ON and OFF states of 2.15 GHz. (c) Radiation pattern (E-plane) at ON and OFF states of 2.25 GHz.

3.4.1 Radiation Pattern Measurement

We first measured the return loss (S11) of the slit in the absorber's OFF and ON states (transistor gates biased negative and positive, respectively) by attaching the standard waveguide WR-430 to the bottom ground plane covering the slit. The slit was basically operating as a slot antenna, but surrounded with the switchable metasurface. The measured return loss results compared with simulated results for a slightly smaller twelve by twelve cell panel is presented in Fig. 3.9 (a). The difference between the measured return loss to the simulated one is mainly due to the fabricated panel is larger than the simulated one which is smaller in size to save simulation time. Measured return loss lower than -10 dB is observed at 2.2 GHz in the OFF state, while in the ON state -1.3 dB is measured. Because

slot antennas radiate through currents on the surrounding ground plane, suppressing those surface currents effectively suppresses radiation, resulting in higher return loss. We further verified this surface current suppression by measuring the radiation pattern in anechoic chamber at the two different states (OFF and ON states).

We used a horn antenna (ETS-Lindgren 3164-08) as transmitting antenna. The distance between the transmitting antenna to the absorbing surface is fixed at 2.5m which is enough to satisfy the far-field distance. The radiation patterns of the E plane of the surface at 2.15 GHz and 2.25 GHz are measured and plotted in Fig. 3.9 (b) and Fig. 3.9 (c). An 18 dB difference between OFF and ON states in the azimuth plane is observed, showing good surface current absorbing ability.

3.4.2 Switchable and Tunable Absorption

In a more intuitive way, the leakage power through the slit compared with the incident power level was measured in the anechoic chamber. The set up for this measurement is presented in Fig. 3.10 (a). Port 1 of the VNA (Agilent E5071C) provides small transmitting signals which are amplified by a high-power amplifier, then further transmitted through the horn antenna with proper polarization, directed toward the center of the panel under test. The standard waveguide WR-430 is attached to the bottom of the slit and the received signal returns to the VNA's port 2. The whole setup including VNA was well calibrated with free space path loss, all insertion loss of cables and connectors, etc. Both normal incidence and grazing incidence are measured with corresponding positions and angles relative to the polarization of the transmitting horn antenna shown in Fig. 3.10 (b).

For the normal incidence mode, the ON and OFF states' gains are measured and plotted in Fig. 3.11 (a). The gain of the surface is defined as the measured S21 value at

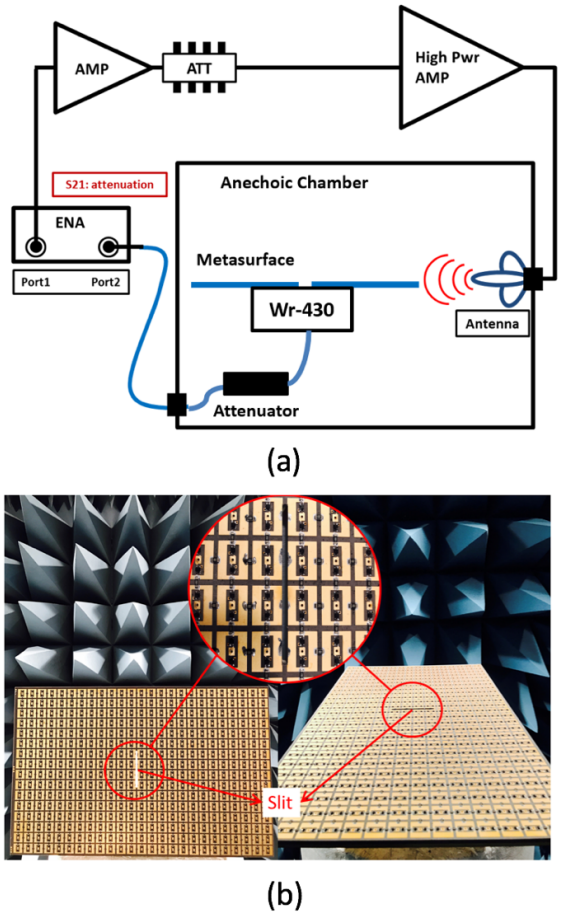

Figure 3.10: Anechoic chamber measurements. (a) Surface wave absorption chamber measurement setup. (b) Normal incidence (left) and grazing incidence (right) modes measurement position of the surface, with zoomed view of the surface. This array's element shares the same dimensions with the element described in Fig. 3.3 (a) and the stack is the same as Fig. 3.3 (c), in which the thicknesses of the RT 5880 and FR4 are both 3.125 mm. The RT5880 and FR4 are isolated by thin prepreg sheet.

normal direction with set up indicated in Fig. 3.10 (a). In the OFF state, a peak gain of 6 dB is observed around 2.2 GHz, which matches with the gain in the normal direction (zero degree) of the slit from the Fig. 3.9 (b) and Fig. 3.9 (c) in part A, Section IV. In the ON state, we could see a peak attenuation of 16 dB at the frequency of interest, showing good surface current suppression ability. For the grazing incidence mode, we measured the surface's tunable and switchable absorbing ability by giving different bias to the gates of all

the transistors (NE3503M04) and the results are plotted in Fig. 3.11(b). In the OFF state, the peak measured gain is around 0 dB, while in the ON state an attenuation of 18 dB is achieved. All these numbers match well with the azimuth-plane amplitude measured in the previous section for both OFF and ON states. With the range from -1 V to 0 V DC bias on the gates of the switching transistors, different attenuations could be obtained, demonstrating the tunable absorption ability of this surface.

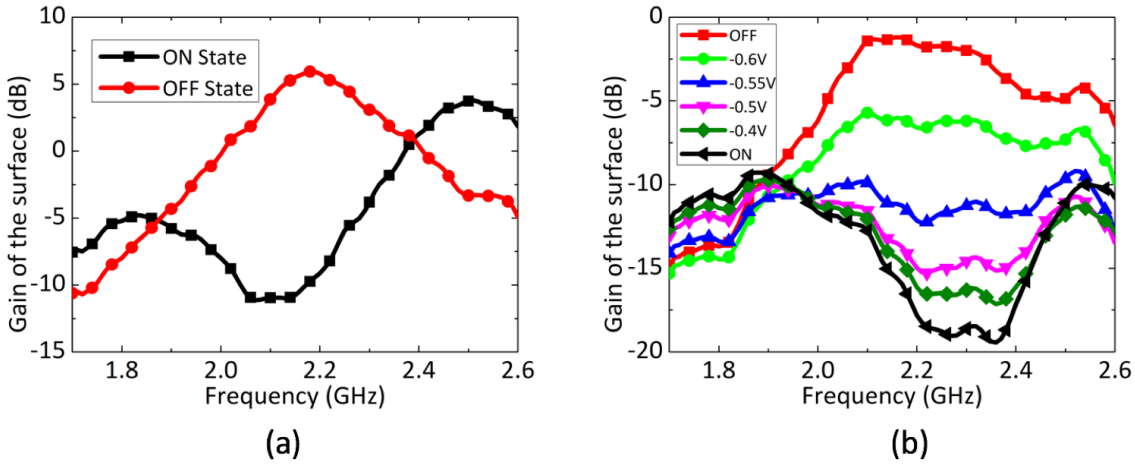

Figure 3.11: (a) Relative amplitude comparing with input power leaking through the slit at on and off states of normal incidence mode. (b) Tunable absorption rate with different DC bias of grazing incidence.

Another advantage of this absorber is that it can potentially provide a sharp response to different incoming power levels. In other words, it is possible to preset a certain power density level threshold to this surface and control the absorber to be switched on, off or to any other middle state accordingly simply by providing different DC biasing voltages. To show this sharp response ability of the absorber, we used power meter (Agilent N1911A) to detect the received leakage power from the slit through standard waveguide WR-430. We define the threshold as the preset value of maximum power (leakage power) allowed to be received by the waveguide (WR-430). In real-time this power level is compared with the preset threshold value to control the DC supply and adjust the surface absorption. The

transmitting signal is generated by a signal generator, (Agilent N5181A) amplified by high power amplifiers (Ophir 5022 and 5193) and transmitted at a power level ranging from 25 dBm to 50dBm at the horn antenna located 2 m away from the surface. The measurement setup is shown in Fig. 3.12 (a) and the absorption response is presented in Fig. 3.12 (b) with different leakage power threshold values. A sharp response is demonstrated using this surface, and the leakage power attenuation from OFF state to ON state is about 17 dB. In other words, the absorber could be real-time controlled switching the surface from OFF state directly into ON state representing a sharp response. This has the advantage that at low power level (less than the preset threshold), the absorber could remain in the OFF state, which would not affect the performance of communication systems under protection. However, as soon as the threshold is reached, the absorber could be automatically turned on to shield sensitive electronic devices.

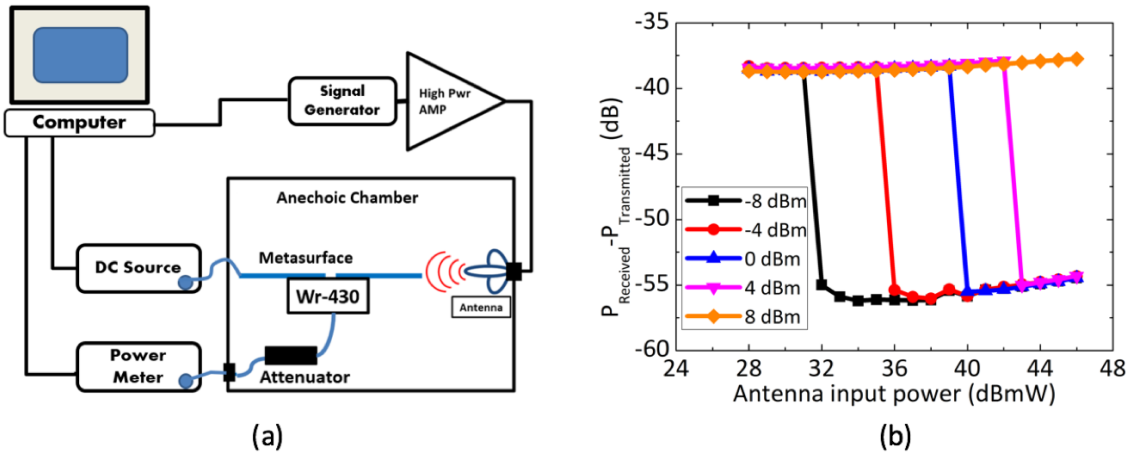

Figure 3.12: (a) Experimental setup for sharp response absorbing ability measurement. (b) Sharp response of absorption with different power level thresholds.

3.5 Conclusion

We introduced the first transistor-based, high-power, switchable and tunable surface wave absorbing metasurface. Two topologies of transistor-based metasurface absorber are studied and discussed. Combining the surface wave suppression ability of high-impedance surfaces with transistors' tunable drain to source channel resistance property, switchable absorbers are designed and measured. In the waveguide high-power measurement, the two topologies showed more than 60% and 70% absorption rate with input power density of 168W/m2 and 838W/m2 respectively in their ON states, while in the OFF states, at the frequency of interest they showed less than 10% and 20% absorption rate accordingly. A large panel with a slit working as a slot antenna is fabricated and measured. The radiation pattern and surface wave absorption is measured in both ON and OFF states and they matched each other well. Finally, a threshold preset self-sensing absorbing surface is tested and showed a sharp absorption response versus input power level.

This high-power, switchable and tunable surface wave metasurface absorber has the advantage of being low-profile, and having electronically controllable absorption, which could be used in against a wide range of incident power levels that may cause damage or interference to the communications systems or sensitive microwave components being shielded.

Chapter 3 is based on and is mostly a reprint of the following paper: **A. Li**, S. Kim, Y. Luo, Y. Li, J. Long, and D. Sievenpiper, "High-Power, Transistor-Based Tunable and Switchable Metasurface absorber", *IEEE Transactions on Microwave Theory and Techniques*, vol. **65**, no.8, pp.2810-2818, August 2017. The dissertation author was the primary author of the work in this chapter, and the co-author has approved the use of the material for this dissertation.

Chapter 4

High Power Microwave Metasurface Transmitter

A low profile, directive, high power and yet cost efficient radio frequency source plays a crucial role in long distance communication, sensing and anti-interference research. Convectional approaches to achieve such high power radiations require a microwave source, an amplifier as well as a radiator, which are mostly expensive and bulky. In this paper, we were able to transform DC energy to electromagnetic radiation, aimed to a desired direction, using only a thin sheet of metasurface. The proposed approach can be scaled both in power and frequency within the UHF to THz range. The concept makes use of the k=0 mode in a periodic resonant surface to excite a series of phase-locked individual sources on the surface. The phase-locked sources create an overall coherent mode in the far field at the desired direction. The proposed idea is inspired by spark-gap transmitters, pulsed ring-down sources, and antenna arrays to provide a novel and highly scalable electromagnetic source. We envision that the proposed active metasurfaces for DC conversion to electromagnetic radiation can be potentially used in long range communication, sensing devices, and radars.

4.1 Introduction and Motivation

Development of electromagnetic radiation sources, which are essential parts of modern communication and radar systems, has been ongoing since over a century ago and has led to many types of sources [99]. For instance, in a conventional source based on the theory of Cherenkov radiation [100], the well-known microwave tube is needed to transform the electronic beam into the radiation. Another example is microwave generators based on transition radiation [101], in which radiation occurs as electrons travels through the boundary between two media with different refractive indices, and so on [102, 103]. Here, we propose a scalable, low-profile and the low-cost radiation source structure based on metasurfaces.

Metasurfaces composed of the two-dimensional subwavelength periodical unit cells, provide the potential to excite and control surface waves which are usually modeled by the generalized sheet transition conditions (GSTCs) [4, 104]. The well-known high impedance metasurface (a.k.a. "mushroom structure") which has a dispersion diagram with non-zero band gaps has found numerous applications in the recent 20 years. At low frequencies, the mushroom textures can only support transverse magnetic (TM) surface waves, while at higher frequencies, above their band gap, they can also support transverse electric (TE) surface waves. Some applications of mushroom structures are the low-profile tunable leaky-wave antenna [105], controlling the surface waves which are dependent of the waveform [14, 76], producing the diode or transistor based surface wave absorbers [2, 62, 75], designing the non-Foster circuit based wideband hard surface and even the realizing of the adaptive metasurfaces [106] which are dominated by the power of the source of the incident wave.

In this paper, the design of a new type of microwave source based on the non-linear mushroom structure has been proposed to transform the direct current (DC) source to the

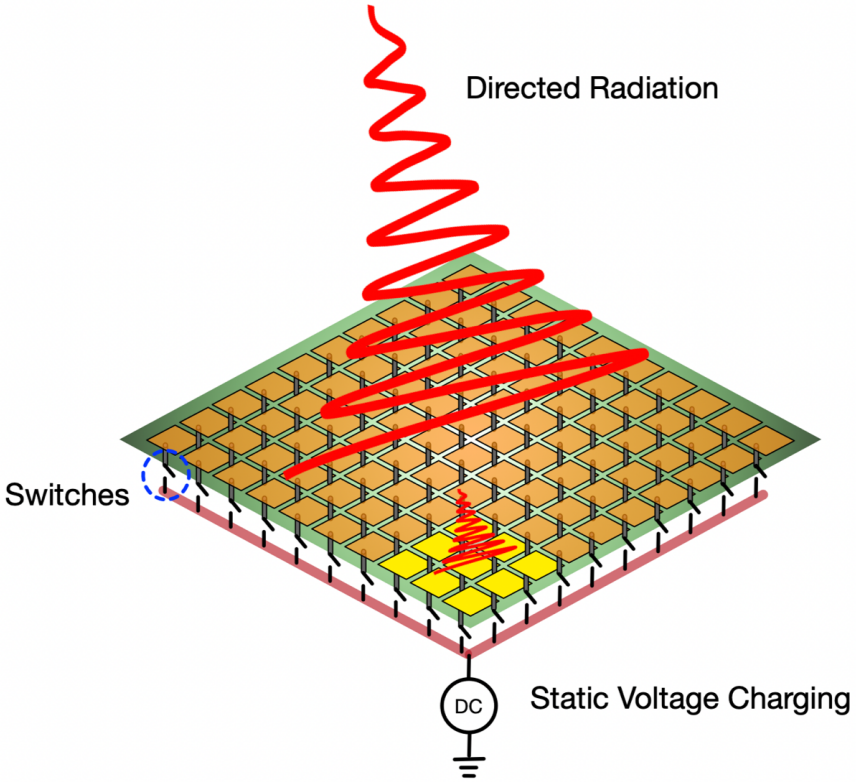

Figure 4.1: Active metasurface transforming static DC energy to steerable RF radiation. The metasurface could be charged up with DC voltages and further triggered simultaneously or in a delayed sequence along rows or columns resulting the charges flowing from top patch to the ground formulating a resonating mode and radiating into free space to the designated direction in a k=0 leaky wave mode.

radio frequency (RF) source. As illustrated in Fig. 4.1, the centerpiece of this work is a resonant textured metasurface which, along with a DC source and a switching mechanism, forms a two-stroke mechanism: a) the charging stroke, during which energy is transferred from the DC source to the capacitive storages on the metasurface, and b) the radiating stroke, in which the stored energy is depleted as electromagnetic radiation.

4.2 DC to RF Transformation Principle

A wide variety of structures can serve this purpose, which can be generally classified as conductor-backed frequency selective surfaces (FSS). The primary requirement is that the structure should include (a) a ground plane to ensure unidirectional radiation, (b) a resonant property which sets the frequency of radiation, (c) an energy storage component which may be considered in the abstract as a capacitor or inductor, and (d) a switch that toggles between charging and radiating strokes. All these 2D surfaces could be potentially charged with a high voltage, only limited by the air breakdown between anode and cathode of the charged surface, thus are capable of handling high power applications. The subwavelength property of the unit cells in metasurfaces, makes the proposed sources highly scalable and very thin compared to their conventional counterparts.

We adopted high impedance surface (HIS) in our designs due to its simplicity and convenience of adding active electronic components to it. We continue with two different topologies of HIS unit cells as demonstrated in Fig. 4.2 (a). Topology A (Fig. 4.2 (b)) consists of top metallic sub-wavelength patches conducted to the ground plane with offset vias, which can be considered as a distributed circuit with and values of,

$$L = \mu t \tag{4.1}$$

$$C = \frac{w(\varepsilon_1 + \varepsilon_2)}{\pi} Cosh^{-1}(\frac{a}{g}) \tag{4.2}$$

where is the thickness of the surface and is the resonating frequency, is the patch width, permittivities of the materials on two sides of the patch, is the period, and is the gap size of the patch.

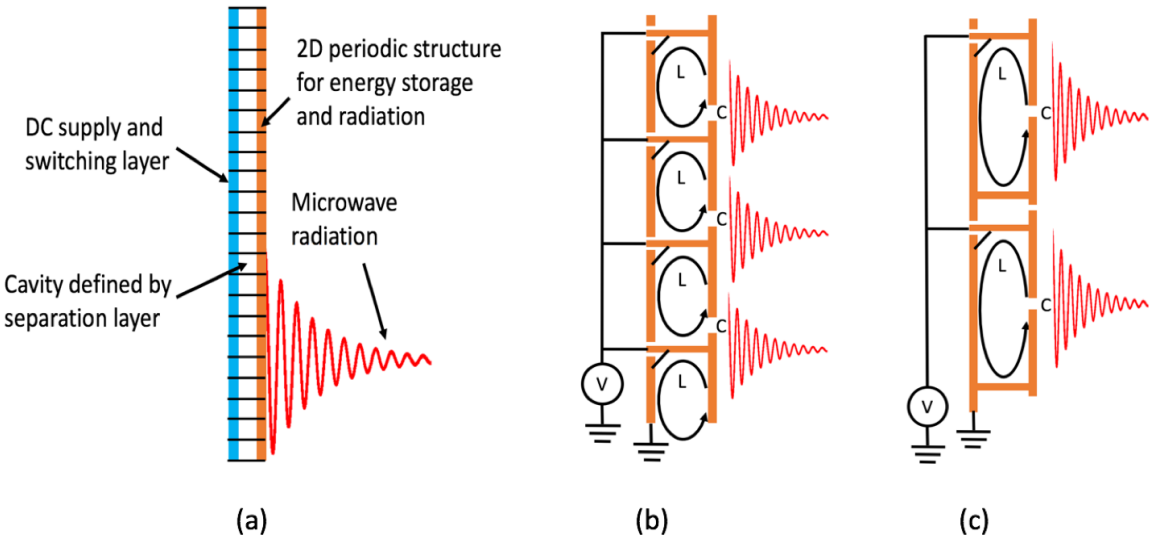

Figure 4.2: Structure crosssection overview and operation principle of two topologies. (a) The basic concept includes a periodic structure that is charged up from a DC supply layer during a charging state, and then switched into a resonant/radiative state. By exciting the k=0 mode of the periodic structure, the radiation from all unit cells forms a coherent beam in the far field. (b) The basic concept can be understood in the context of a offset via high impedance surface consisting of a switchable LC circuit. The capacitance is charged up during the charging state and the inductance is switched in during the radiative state. (c) Unit cell of topology B is composed of a pair of metallic patches with mirrored offset vias at the edges. One via is connected with DC source charging up the top patch at charging state, while the other via connects top patch to the ground. When switch is on, a cavity is formed and radiating energy out at the resonating frequency of the structure.

In order to better demonstrate the concept, we first use ideal single pole double throw switches (SP2T) placed at the gap between the conducting vias and the ground plane. During the charging stroke, the switches are in the OFF state (vias are not connected to the ground). As a result, the DC power source (with the voltage V) stores energy of $(\frac{1}{2}CV^2)$in the capacitive regions around the gaps between neighboring unit cells. The radiating stroke begins as soon as switches are triggered ON instantaneously (vias conducted to the ground) which causes charge oscillation inside unit cells. With proper design of the subwavelength periodic HIS structure, the oscillating charges can radiate energy into the space. In fact, the

radiation is a result of a leaky wave mode excitation on the HIS at the frequency defined by the and C values of the HIS. Note that the vias are designed to have offset in order to avoid opposite polarities among neighboring radiating elements, ensuring they all add up in phase in the far field. As the stored energy damps during the radiating stage, each element's voltage rings down as a decaying sinusoidal wave into free space.

Topology B (Fig. 4.2 (c)) has a unit cell composed of a pair of subwavelength metallic patches with two offset vias on the opposite edges of the patches. One of the vias is directly connected to the ground while the other via is connected to a switch which bridges it to the ground. By adjusting the symmetry of the structure, the resonance can be split into two modes resonating at different frequencies. The structure can be designed so that nearly all of the energy is stored in regions that correspond to one of the modes. As both topologies in Fig. 4.2 have subwavelength dimensions, it is completely feasible to combine hundreds or even thousands of unit cells to scale the power. Moreover, by precise control of switches timing, the radiated energy can be guided to a desired direction. Topology A is more uniform and compact than topology B, however it requires more switches for the same aperture size.

Both proposed topologies include two-dimensional periodic structures which can be represented by their band structure for surface waves. As shown in Fig. 4.3, our design excites the $k = 0$ mode (when all switches are triggered simultaneously) which is where the first TE mode meets the frequency axis. The curve extraction is discussed in the methods section.

The power radiated from the scalable microwave source can be estimated from the voltage on each cell, and the dimensions of the cells. Assuming a square aperture, radiated power is equal to the total voltage (V_{total}^2) squared divided by the impedance of free space.

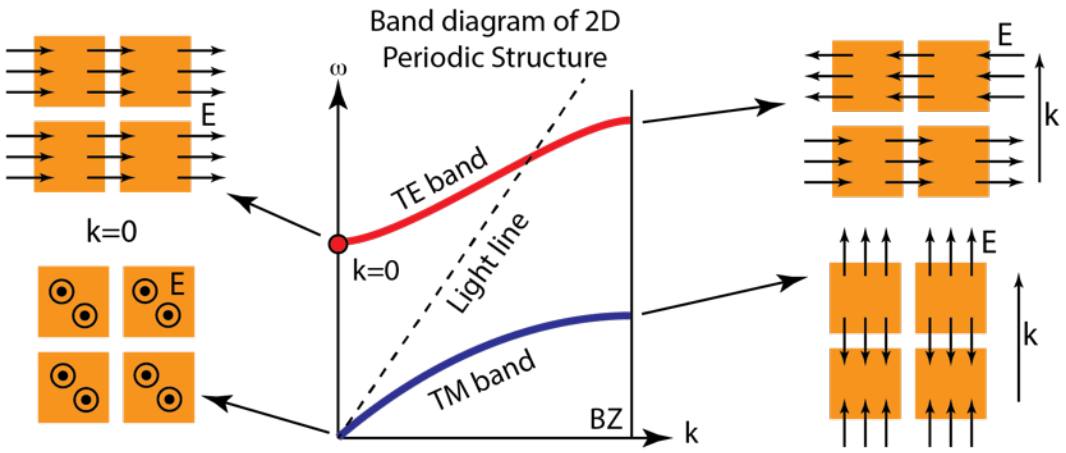

Figure 4.3: Dispersion diagram of the traditional high impedance surface. The band structure of the periodic surface gives clues to the kinds of modes that the surface supports. The classic high impedance surface supports both TM surface waves and leaky TE surface waves.

$$P_{rad} = \frac{V_{total}^2}{\eta} \tag{4.3}$$

in which η is vacuum intrinsic impedance. Total voltage is equal to the voltage on each cell (V_{cell}) times the ratio of total size to cell size, $V_{total} = V_{cell}\frac{L}{l}$, in which is the length of the metasurface while is the period of the unit cell. The antenna gain (G) is related to the area and wavelength (λ), estimated to be assuming 100% radiation efficiency. The peak effective isotropic radiated power (P_{eff}) of the pulse is given by the total power (P_{rad}) times the gain of the metasurface:

$$P_{eff} = P_{rad}G = \frac{4\pi V_{cell}^2 L^4}{\eta l^2 \lambda^2} \tag{4.4}$$

The surface quality factor is related to its thickness () relative to the wavelength on resonance:

$$Q = \frac{\lambda}{2\pi t} \tag{4.5}$$

The duration δ of the pulse is related to the :

$$\delta = \frac{Q}{\omega} = \frac{Q\lambda}{2\pi c} = \frac{\lambda^2}{4\pi^2 tc} \tag{4.6}$$

The effective pulse energy is the average effective isotropic radiated power (EIRP) times the pulse duration:

$$U_{pulse} = \frac{P_{eff}\delta}{2} = \frac{V_{cell}^2 L^4}{2\pi\eta l^2 tc} \tag{4.7}$$

The actual energy required to charge up the capacitors can be obtained as follows. The resonant frequency of the metasurface ($\omega = \frac{1}{\sqrt{L/C}}$) can be determined from (4.1) and (4.2). This gives us the resonance quality factor as:

$$Q = \frac{\eta}{\sqrt{L/C}} \tag{4.8}$$

These can be combined to obtain the capacitance per unit cell:

$$C_{cell} = \frac{Q}{\eta\omega} \tag{4.9}$$

with total capacitance to be $C_total = \frac{Q}{\eta\omega}\frac{L^2}{l^2}$, thus, the total energy to charge the surface for each pulse can be calculated as:

$$U_{charge} = \frac{C_{total} V_{cell}^2}{2} = \frac{\lambda^2 L^2 V_{cell}^2}{8\pi^2 l^2 t\eta c} \tag{4.10}$$

Then, we can calculate the ratio of radiated pulse energy to charging energy, and find that it

is equal to the antenna gain as expected.

$$\frac{U_{pulse}}{U_{charge}} = \frac{V_{cell}^2 L^4}{2\pi\eta l^2 tc} * \frac{8\pi^2 l^2 t\eta c}{\lambda^2 L^2 V_{cell}^2} = \frac{4\pi L^2}{\lambda^2} = G \tag{4.11}$$

4.3 Simulation Analysis

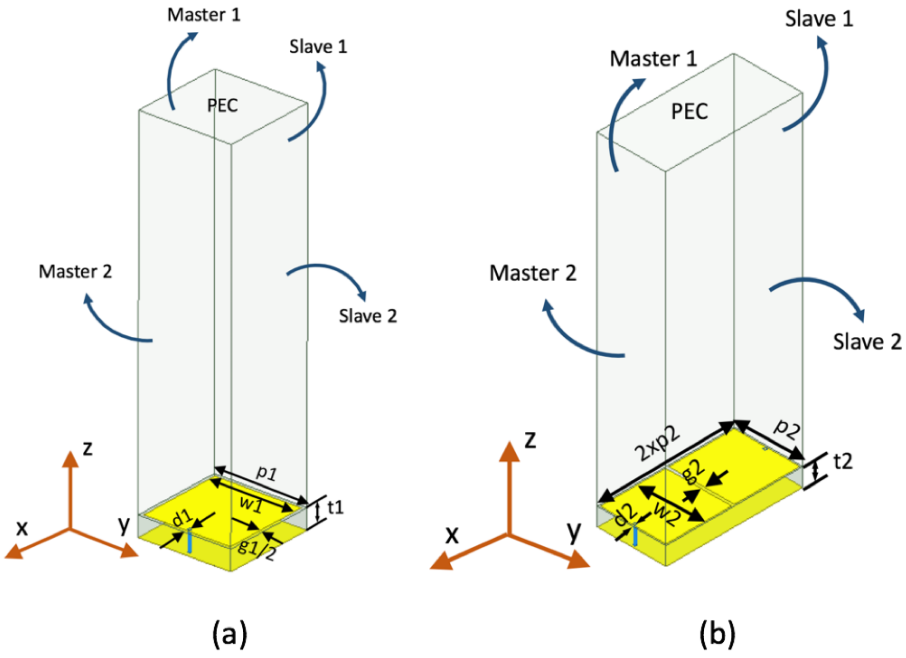

Figure 4.4: HFSS model in eigenmode simulation. (a) Topology A. (b) Topology B.

We designed both topologies A and B (in Fig. 4.2) to radiate at 2.2 GHz frequency in HFSS. The model of both topologies are depicted in Fig. 4.4 in this material, for topology A, with period p1 = 16mm, gap size g1 = 1mm, patch width w1 = 15mm, via offset d1 = 1mm with via radius r1=0.25mm, substrate (Rogers Duroid 5870, dielectric constant 2.2) thickness t1 = 3.175mm and the height of the air box h = 60mm, while for topology B, p2 = 12mm, g2 = 0.5mm, w2 = 11.5mm, d2 = 0.6mm, r2 = 0.25mm, t2 = 3.175mm with same substrate material with topology A. Along the via offset direction (x axis direction in

this case), the two side walls are set to be master and slave boundaries with a variable of phase delay defined. The other two side walls (along y direction) are set master and slave boundaries with no delays. When eigenmode simulations are performed in HFSS sweeping the delays from 0 degree to 180 degrees and the first mode (TE mode) and the second mode (TM mode) could be extracted and shown in Fig. 4.5. The intersection of the TE leaky mode to the frequency axis is indicating the supported surface wave propagation along the surface (x direction) is zero, in other words radiating out normal to the surface into free space.

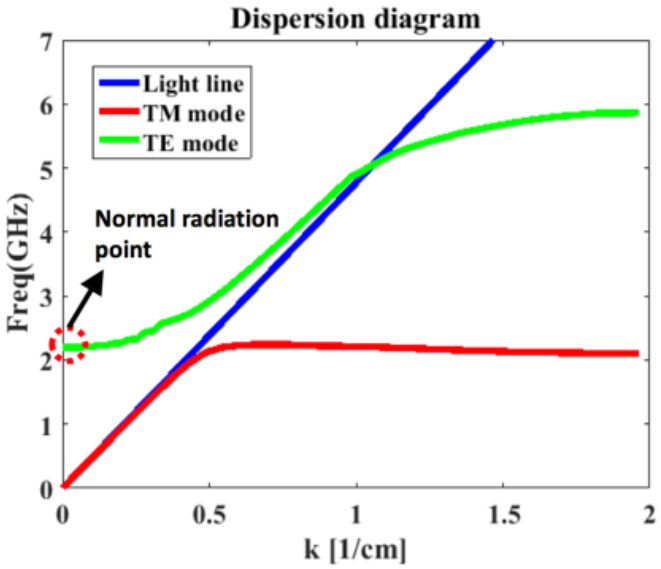

Figure 4.5: Dispersion diagram of topology A with TE mode intersect with k=0 at 2.2 GHz which is coherent with the frequency of the radiated signal.

Using EM-circuit Co-simulation method we could more straightforwardly simulate the whole operating process from DC charging state to radiative state in time domain. The two port HFSS model is first made in full wave driven modal simulator of HFSS shown in Fig. 4.6 (a) (Topology A) and Fig. 4.6 (b) (Topology B). Not that there is ring shaped gap between the via and the ground with a lumped port applied. The top surface of the air box is defined as a flouquet port. The side walls are set to be periodic boundaries (Master and Slave boundaries) with no delay. All the other dimensions are consistent with Fig. 4.4.

A wide frequency range are swept from the simulation from DC to 10 GHz to get wide enough frequency bands for more accurate transient simulations later. The 2 port S-matrix is obtained and plugged into the circuit simulation with the lumped port pinned with a SP2T switch switching between DC charging source (100V) through a 500 charging resistor and the ground while top flouquet port is terminated with a 377ω resistor consistent with free space characteristic impedance. The switch toggled between the DC source and ground with ON time 50 ns which is long enough to damp the charged static charges, with OFF time 50 ns (total 100 ns for one period) long enough to have the surface fully charged. The schematic of the circuit simulation is shown in Fig. 4.6 (c). From the EM-circuit Co-simulation explained in this section, topology A and topology B's radiated RF voltages could be obtained and plotted in Fig. 4.7 (a) and Fig. 4.7 (b) respectively. The blue curves represents the charging DC voltage while the red damping sinusoidal wave indicates the radiated RF waveform monitored from the 377 ω resistors at in the circuit model. The spectrum of both structures are plotted in Fig. 4.7 (c) and Fig. 4.7 (d) respectively.

4.4 Efficiency Calculation

The efficiency of this direct DC to RF conversion could be obtained if the stored DC energy and radiated RF energy could be obtained. The stored static DC energy P_{dc} is:

$$P_{dc} = \frac{1}{2}CV^2 \tag{4.12}$$

where C is the equivalent capacitance of the metasurface and V is the charging voltage. To find the value of C, we can derive from the resonating frequency $\omega = \frac{1}{\sqrt{LC}}$ if we know the equivalent inductance L. For the centered via high impedance surface (HIS),

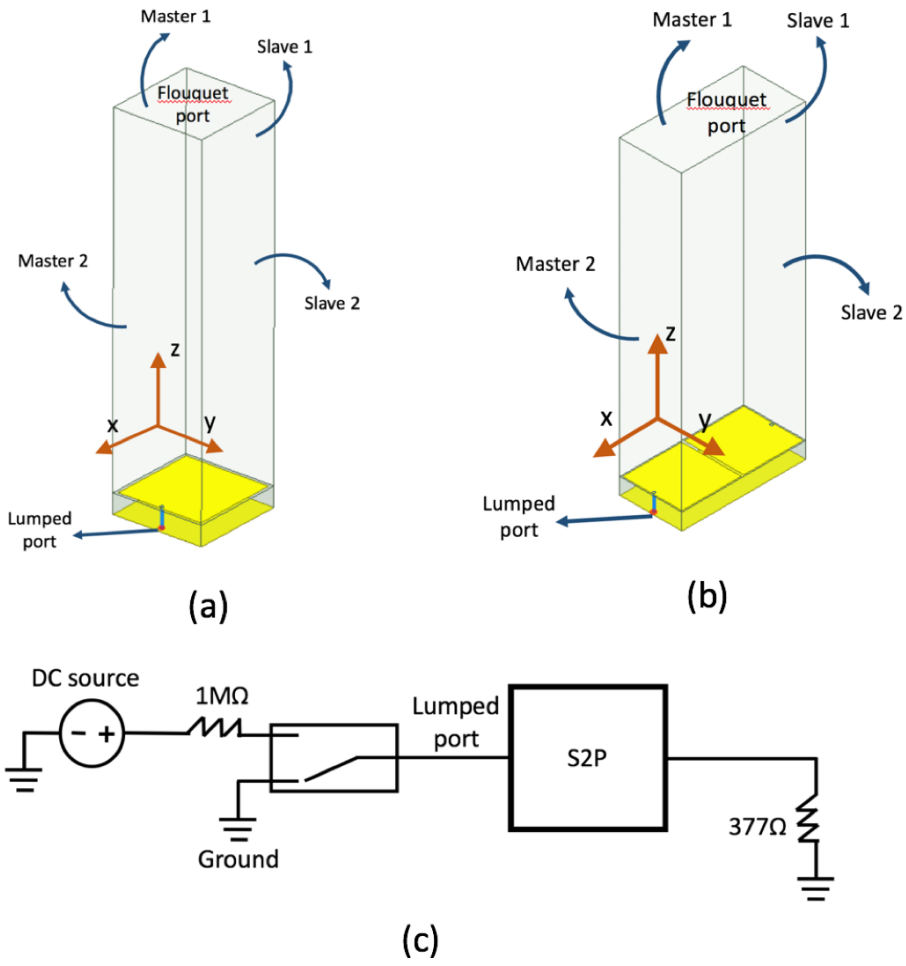

Figure 4.6: EM-circuit Co-simulation models. (a) Topology A: Driven modal simulation in HFSS with periodic boundaries, topped with a flouquet port with a lumped port set between the via and the ground. (b) Topology B. (c) Extracted S-parameters (S2p) file is linked to the circuit simulation to perform transient simulation in circuit simulator.

$L = \mu t$, where μ is the permeability of the substrate and t is the thickness of the substrate. However, as our proposed structures are offset via HISs, a more accurate way of extracting C is needed. The equivalent capacitance could be obtained accurately from the time constant τ,

$$\tau = RC \tag{4.13}$$

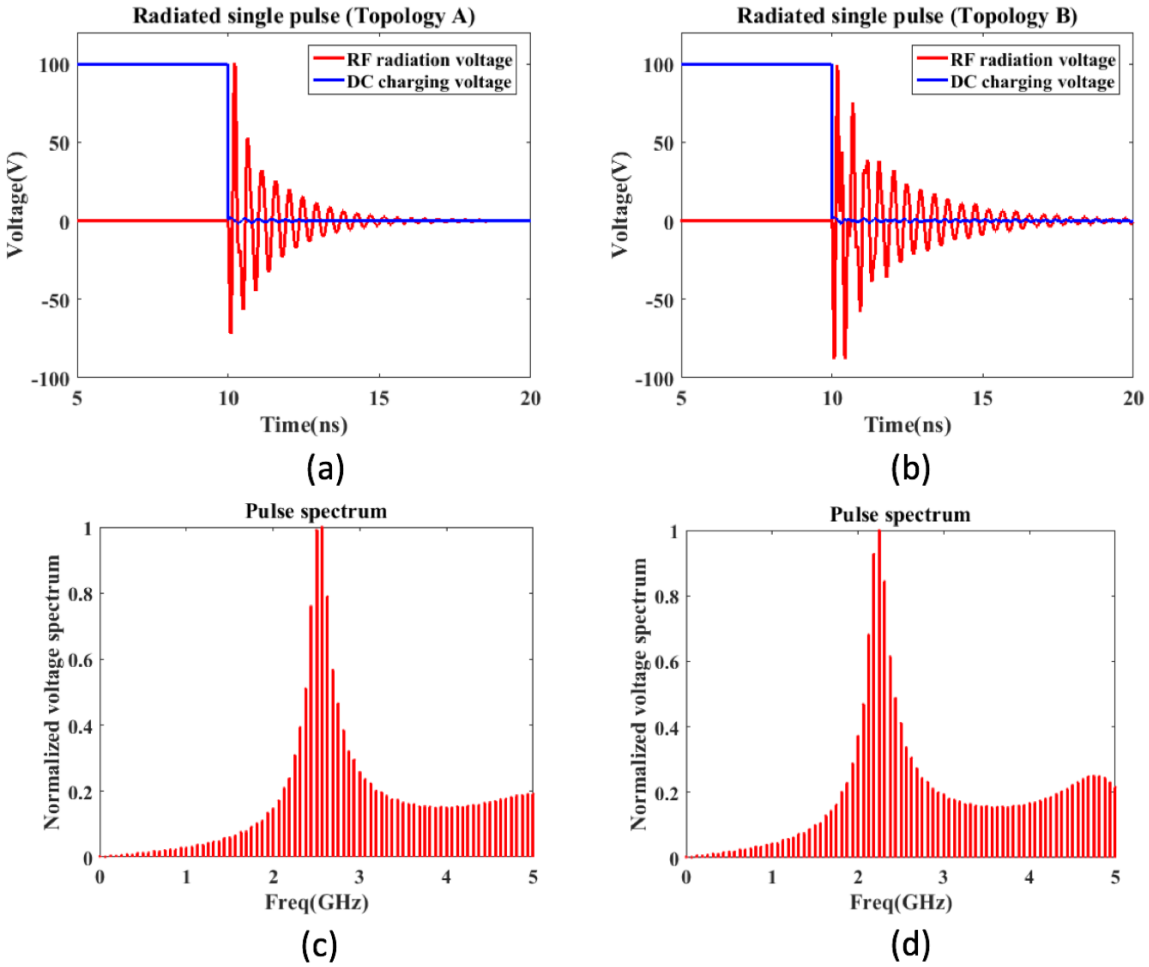

Figure 4.7: EM-circuit Co-simulation results. (a) Transient simulation output of Topology A. (b) Transient simulation output of Topology B. (c) Spectrum of output signal of Topology A. (d) Spectrum of output signal of Topology B.

where R is the charging resistor to the surface. τ could be obtained from the simulation, at the time the voltage is charged up to 63% of the ultimate voltage, shown in Fig. 4.8 for topology A as an example. From equations. 4.12, can be accurately estimated. can be easily calculated by integrating the energy in one period known from Fig. 4.7 (a) for topology A and Fig. 4.7 (b) for topology B. The efficiency of topology A is calculated to be 93% and topology B to be 88%, which are all close to unity.

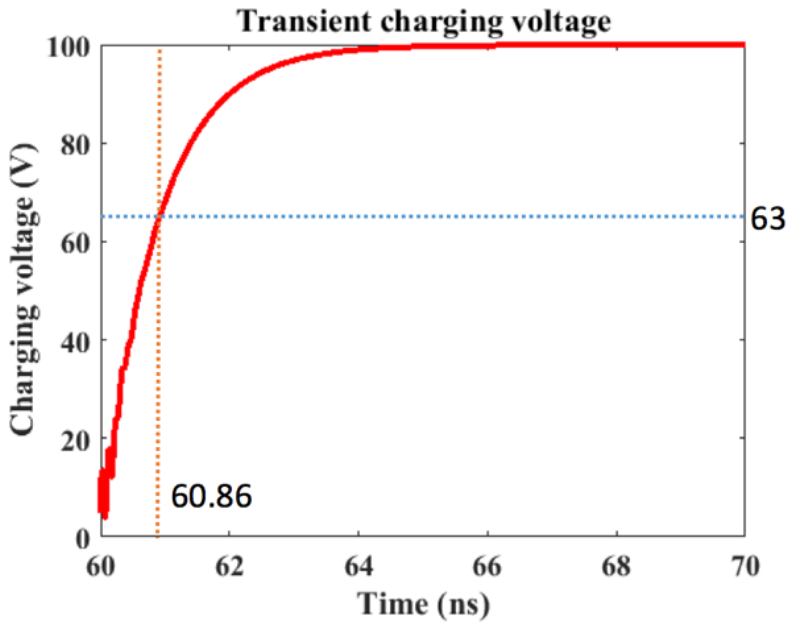

Figure 4.8: Charging voltage in time domain of topology A. Time constant can be calculated from where voltage equals 63% of the ultimate static voltage (100V) to be 0.86ns.

4.5 Fabrication and Measurement Results

In practice, ohmic loss and finite speed are inevitable while implementing the switch. Possible choices for the triggering switches are transistors, optical switches, or plasma switches, which are all applicable in high power designs. Note that the rise time of the switch should be way smaller than the period of the resonating signal to minimize loss. Avalanche transistors being widely applied in ultra-fast pulse generators and switches with rise times below nanosecond stand out as good candidates for sub GHz applications with high peak currents. To apply avalanche transistors to our metasurface, we connected the transistor collector and emitter to the via and ground, respectively. The transistor collector is also attached to the DC supply using a charging resistor. After the whole meatsurface array is charged, all avalanche switches can be switched ON, simultaneously, by triggering the transistors' bases using an ultra-fast pulse. We re-designed both topologies A and B (in

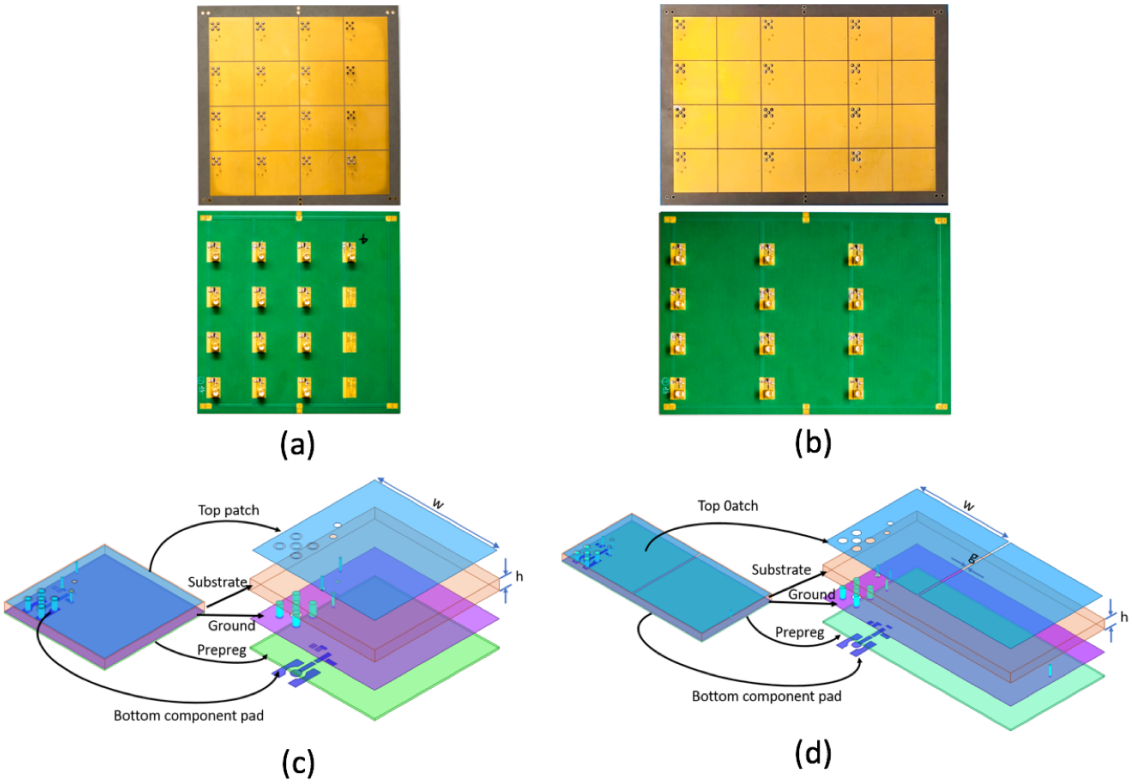

Figure 4.9: Fabrication and unit cells. (a) Fabricated 4 by 4 array of topology A. (b) Fabricated 4 by 3 array of topology B. (c) Topology A's unit cell's stack up. (b) Topology B's unit cell's stack up.

Fig. 4.2) for 800 MHz to verify the concept experimentally. Fig. 4.9 shows both topology A and topology B's fabricated panel and the measurement results. The chosen avalanche transistor's (FMMT413) rise time is experimentally measured to be around 500 ps. As a result, we limited our operating frequency to 800 MHz to avoid excessive loss and jittering noise at higher frequencies. Both of the structures are composed of three layers with a top patch layer, middle ground layer and a bottom switching layer. Fig. 4.9 (a) and Fig. 4.9 (b) show the 4 by 4 array of topology A and 4 by 3 array of topology B, respectively. Note that for topology A shown in Fig. 4.9 (a), only the left three columns are back mounted with avalanche transistors and the last column on the right is working as parasitic patches. The offset vias contribute to the inductance while the gaps between patches in horizontal

position gives parasitic capacitance. Topology B does not require extra column of unit cells as parasitic patches since the unit cell comes into a pair and the parasitic capacitance are mostly due to the gap in between unit cell patches. The stack up information with detailed dimensions of the two topologies' stack ups are shown in Fig. 4.9 (c) and Fig. 4.9 (d). The value of the charging resistors is chosen to be 1 M. A 50ω SMA connector is directly mounted at the base of the avalanche transistors for feeding the triggering signal. To evaluate the DC to microwave radiation performance of the metasurface, we measured the normalized radiation pattern of both topologies in the anechoic chamber for both horizontal and vertical polarizations. The surface is biased 100 V which is below the avalanche break down voltage of the transistors. A picosecond pulse generator working with a periodicity of 100 kHz is used to trigger all cells of the metasurface simultaneously through designed power dividers. We observed a peak radiation at the normal direction with cross-pole over 10 dB. A measured radiation pulse of topology A and B are shown in Fig. 4.10 (a) and Fig. 4.10 (b) respectively. The associated spectrum of this pulse has a peak at 625 MHz, as shown in Fig. 4.10 (c) and Fig. 4.10 (d). The decaying sinusoidal wave was captured by a receiving antenna as expected. As in the simulation we used an ideal switch, there was a frequency shift in the measurement (from 800 MHz to 625 MHz) due to the parasitic elements of the avalanche transistors. From the transient signal, we could calculate the ratio of the total radiated power to the stored static energy around 10 percent. The measured radiation pattern of topologies A and B are shown in Fig. 4.10 (e) and Fig. 4.10 (f) respectively. And the measurement setup schematic and photo of of far field measurement environment are shown in Fig. 4.11 (a) and Fig. 4.11 (b).

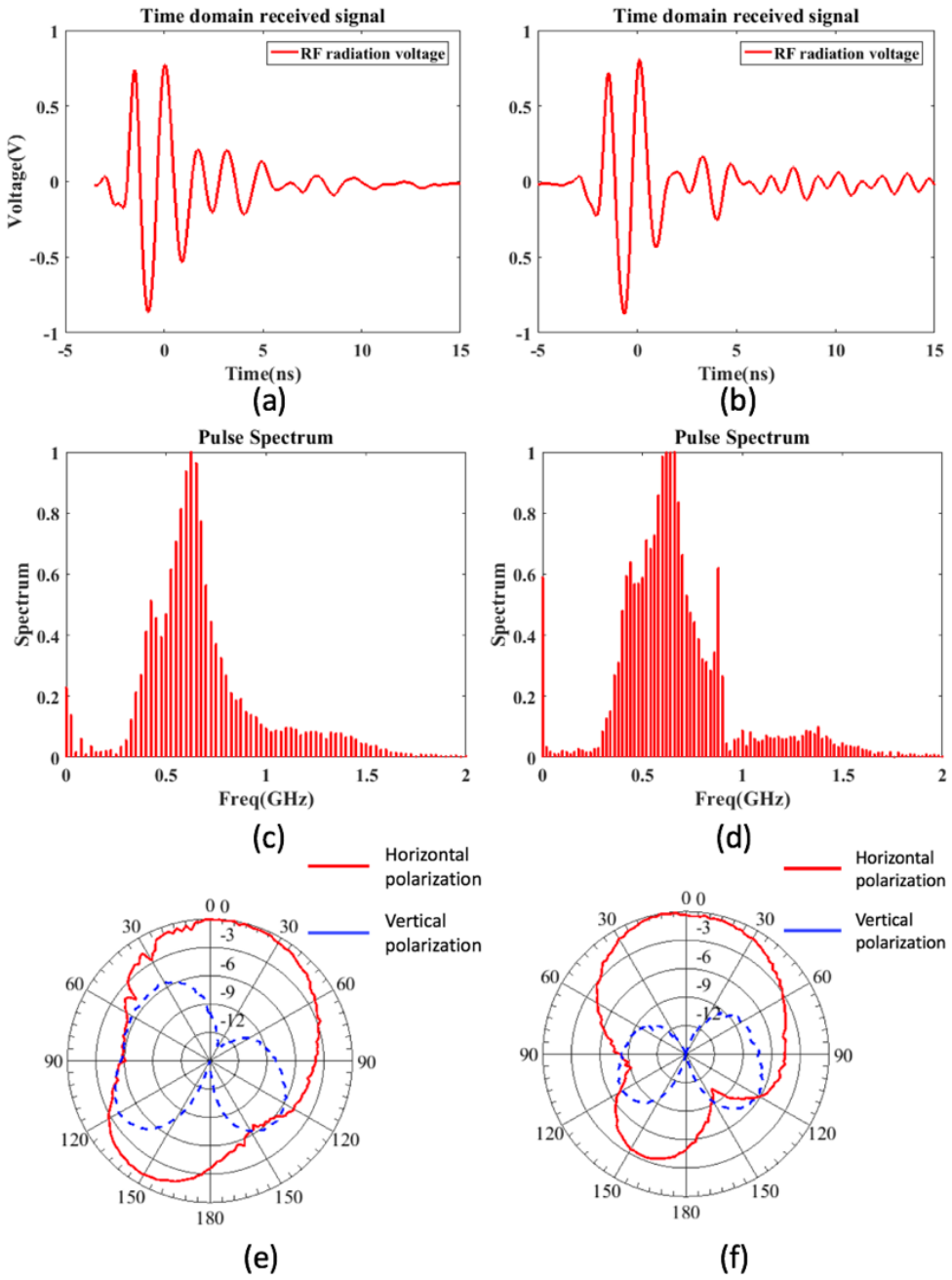

Figure 4.10: Measurement Results. (a) Topology A's normal direction radiated signal from 3 meters away. (b) Topology B's normal direction radiated signal from 3 meters away. (c) Spectrum of topology A's output. (d) Spectrum of topology B's output. (e) Radiation pattern of both topology A with both horizontal and vertical polarizations. (f) Radiation pattern of both topology B with both horizontal and vertical polarizations.

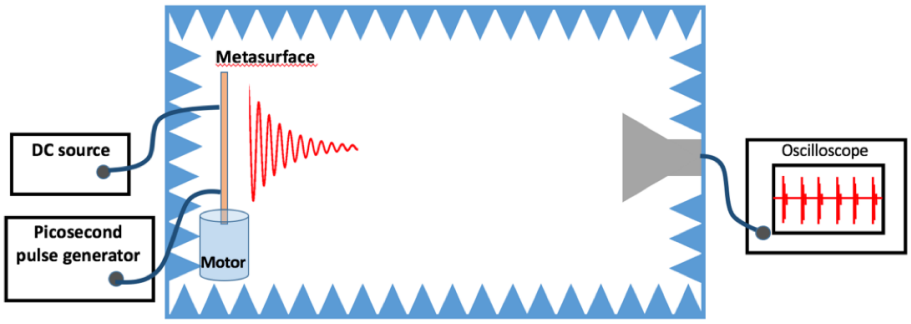

(a)

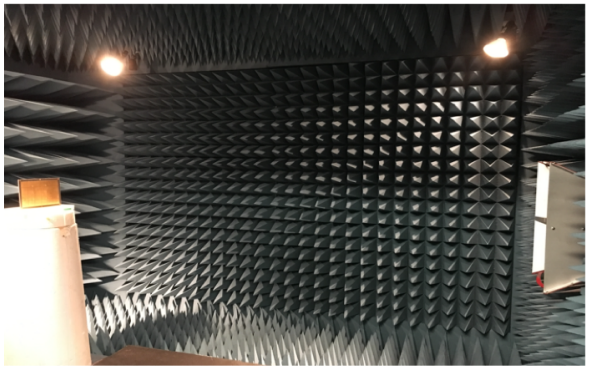

(b)

Figure 4.11: Experimental setup. (a) Schematic of the setup in anechoic chamber. (b) Photo of the measurement environment.

4.6 Beam Steering Capability

Besides normal radiation, the proposed metasurface can potentially have beam steering capability. In this section, we demonstrate this capability in simulation perspective, since it needs a comparatively larger array with a sharp beam to make this beam steering effect visible. When the metasurface elements are all charged up but triggered to oscillating mode with an increasing delay between each rows or columns we are expecting a beam shift to a specific angel that all elements radiation in far field adding up in phase. Taking topology A as an example, we simulated an array of 4 by 16 shown in Fig. 4.12 (a). With the push excitation technique in HFSS, we could push the delayed triggering transient current sources back to the HFSS full wave simulation hence generating the radiation pattern with different

column/row to column/row delays. Fig. 4.12 (b) shows the E-plane radiation pattern with different switching triggering delays (d_t) between neighboring columns.

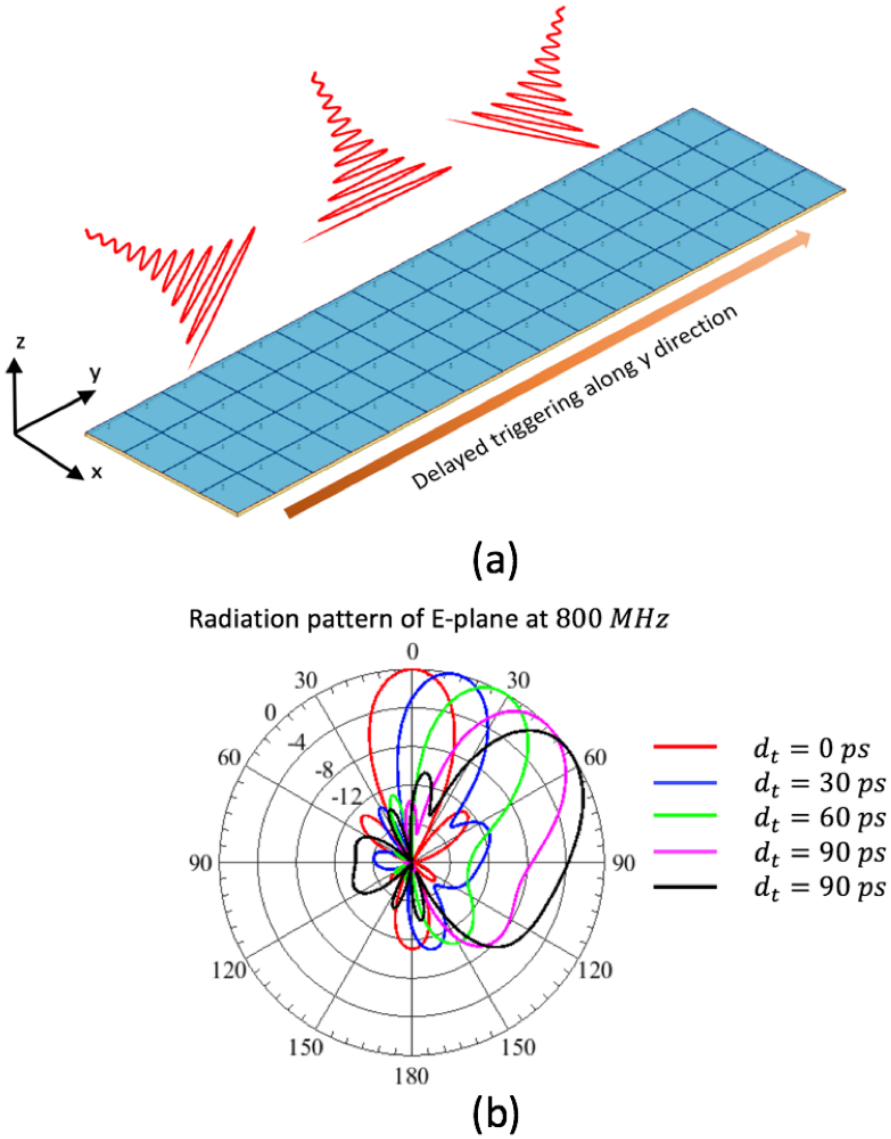

Figure 4.12: Beam steering simulation. (a) Simulation model of the 4 by 16 HIS array with an increasingly delayed triggering along the y direction. (b) Normalized radiation patterns in dB with different delay intervals. A beam steering effect is observed.

Besides using electric switches approach, optical trigger could be adopted taking advantage of their sharper response and easiness to be massively triggered. For example, a

photoconductive switch, or a phototransistor could be turned on by an optical signal. This has the advantage that the optical signal can be designed to illuminate the entire surface at the same time, to ensure that all cells fire in-phase. While this is also possible with a well-designed electrical triggering system, optics has the advantage of a free-space distribution option. By varying the angle of incidence of the optical pulse, the delay could be added between cells, which would translate into steering the radiated microwave beam as well.

4.7 Discussion and Conclusion

We have introduced a novel approach of transforming DC energy directly into desired RF radiation. This paper describes a new class of scalable high power microwave sources that borrows concepts from existing architectures, while applying new materials and techniques to dramatically increase power, frequency, and flexibility. The concept makes use of a k=0 mode in a periodic resonant metasurface to produce a coherent mode from many individual sources which are combined in-phase in the far field. This is combined with ideas borrowed from spark-gap transmitters and pulsed ring-down sources to provide a novel and highly scalable RF source that is also grounded in well-established concepts. We adopted offset via HISs as the media for this transformation, due to its ultra-thin and highly scalable property. Our simulated results showed an efficient transformation from DC to microwave radiation by combing active switches on the surface when all unit cells are triggered together and radiating simultaneously resulting a pulsed decaying sinusoidal wave radiation. It is envisioned that these new RF sources can be scaled from UHF to THz frequencies depending on various design parameters, and will be capable of multi-GW operation. To demonstrate our concept, we designed and fabricated two topologies of the meatsurface array applying avalanche transistors as switching, a directional RF radiation is

achieved. The drop in the converting efficiency in our measurement is mostly due to the losses and phase mismatch introduced by the switch. The shift in frequency is mostly due to the parasitics of the avalanche transistors. Beam steering could be achieved by adding delays to the switches between each rows or columns. This gives the metasurface a totally RF feedless, 2D scanning microwave emitting source by charging the metasurface with DC currents as well as triggering the surface with different switching sequences.

In conclusion, we proposed a scalable, ultra-thin active microwave transmitting metasurface with only DC energy as a source with beam scanning capabilities. This novel concept takes TE leaky wave mode of the periodic structures converting static DC currents into desired RF directional radiation could be applied in applications including high power microwave source, long range communication, sensing and radars.

Chapter 4 is based on and is mostly a reprint of the following paper: **A. Li**, Y. Li, E. Forati, S. Kim, J. Lee, J. Long and D. Sievenpiper, ”Direct conversion of static voltage to a steerable RF radiation beam using an active metasurface”, in preparation. The dissertation author was the primary author of the work in this chapter, and the co-author has approved the use of the material for this dissertation.

Chapter 5

Spatial-temporal Modulated Metasurface Non-reciprocal Absorber

We investigated a magnet free, non-reciprocal surface wave absorber based on high impedance surfaces (HIS) with time modulation approach. By modulating the surface by controlling the switches in sequence, the HIS metasurface breaks time and spatial symmetry, which could transmit surface waves at the designated frequency from one side of the surface to another but absorber power propagating reversely. From EM-circuit co-simulation results, we could observe an obvious non-reciprocity. We could envision that this could be possibly applied in future communication systems that preferably transmitting unidirectionally but absorbing interference from reverse directions caused by reflections or other devices.

5.1 Introduction and Motivation

Nonreciprocity plays an important role historically starting from Faraday rotation [107] discovered in 1845. In modern research and industrial applications, there are

numerous of phenomena and devices show their significance due to their nonreciprocal properties, for example, circulators, isolators and duplexers, etc. A traditional way of performing this nonreciprocal purpose is to involve a magnetic bias which aligns the spin of magnetic-optic materials, resulting huge difference in opposite direction wave transmission. However, as these conventional solutions are ferrite based [108], which are bulky, expensive and high cost. To have non-magnetic based nonreciprocal devices, antennas or surfaces are critical in recent applications for both microwave and optical frequencies due to the increasing demand on compactness of the system [109–111]. An interesting work applying angular momentum fulfilling a circulator for acoustic wave [112] is carried out. Recent researches demonstrated several approaches to break the symmetry, in which, time-varying media [113–115] brings broad attention in the non-reciprocity research. Works have been done in modulating the substrate, which makes the effective index of the substrate to be time varying that could be applied in nonreciprocal leaky wave metasurface antennas and isolators, etc [116–118]. Spatial-temporal modulation method has also been explored to fulfill unidirectional transmission [119–122]. Another new approaches to break the linearity is to apply switches to the transmission lines and manipulating the waveforms by controlling the sequences of the switches and further are demonstrated being integrated into chips [123, 124]. However, there are less work carried out for applications of nonreciprocal surface wave absorbers. For absorbers targeting on normal incidence are widely studied while for surface waves absorbers are also important but less investigated. Especially for transvers magnetic (TM) wave propagations, there are potentially leakage from openings and connections between discontinuous metallic surfaces. Metasurface absorbers [125–127] are widely studied and applied in both spatial and surface wave absorption applications due to their low profile, usually subwavelength thickness also simplicity, composed of metallic

patches. Recent studies brought active electronics including diodes, varactors and transistors to the metasurface absorber enabling the surface with more attracting properties like power dependency, waveform dependency, switchability and self-tuning capabilities. However, all these absorbers in the reference have reciprocal responses.

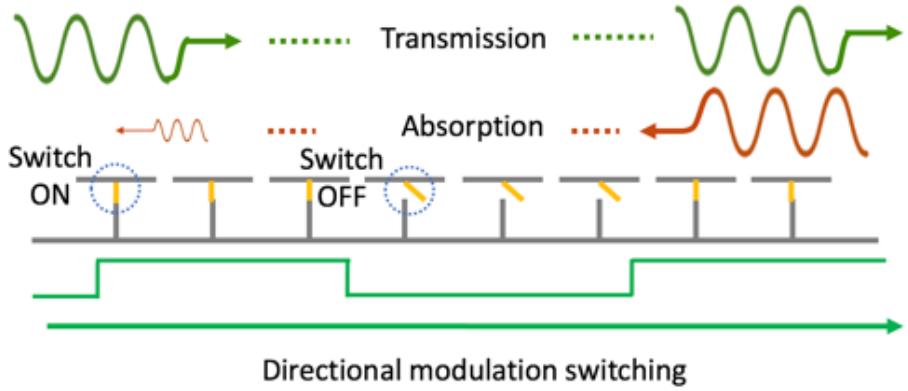

Figure 5.1: Diagram of principle of the time modulated non-reciprocal metasurface surface wave absorber. An ideal switch is placed at the via of the HIS conducting (ON state) and isolating (OFF state) the via and top patch. When the vias are modulated from left to right with a certain frequency, surface waves could propagate from the left to the right but absorbed from the right to the left.

It is critical to develop nonreciprocal surface wave absorbers since we may need unidirectional communication or surface waveguiding but absorbing opposite directional transmissions to avoid interference to sensitive electronics or devices from transmitting signals reflections or other jamming signals. High impedance surface (HIS) is a good candidate for surface wave absorbers because it supports no modes at the bandgap thus stops surface waves from propagation. By simply placing resistors at the gap between neighbouring elements, energy could be further dissipated as ohmic loss. Works have been done by applying active electronics on the HIS surface wave absorbers like varactors, transistors and diodes enabling the surface with property of frequency tenability, switchability, non-linearity and power dependency, etc. However, all these approaches did not break the symmetry

of the surface, in other words, the absorption or transmission property from forward and backward directions are consistent.

5.2 Principle and Theoretical Analysis

Here we propose a way to modulate the surface in a manner of traveling wave in a single direction, which could break the symmetry of the surface magneticlessly, indicated in Fig. 5.1. An ideal switch is placed between the top patch and the via to the ground of the HIS, reconfiguring the metasurface to be HIS (vias conducted the to the ground) and periodic subwavelength patches (without vias). When the switch is at ON state (conducting top patch to the ground), the surface forms a HIS which has a band gap between the first transverse electric (TE) and transvers magnetic (TM) mode that stops surface waves from propagating. On the contrary, when the switches are at OFF state (vias not conducting top patch with the ground), at the same frequency, TM waves can propagate through the surface. The absorption rate at two different switch states are simulated and the full wave simulation model is shown in Fig. 5.2. The full wave simulation model in Ansys HFSS is assigned with periodic boundaries and 10k resistor between gaps of the patches. Absorption rate (Abs) could be calculated as:

$$Abs = 1 - Transmission - Reflection \tag{5.1}$$

where Transmission is transmission rate defined by the transmitted power over incident power and Reflection is reflection rate defined as reflected power over incident power, shown in Fig. 5.3 (a). Here when the switches are at ON state, all the unit cells are turned into small cavities with via conducting top patch to the ground forming a HIS. The property of

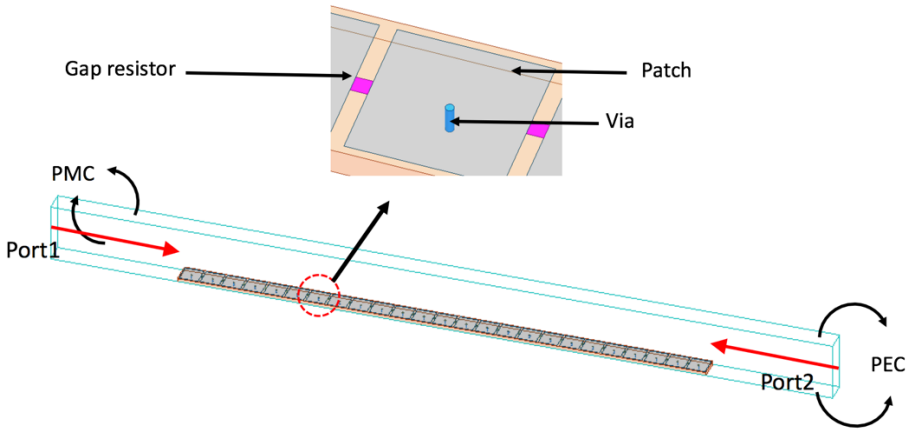

Figure 5.2: Full wave simulation model with periodic boundaries, perfect electric conductor at top and bottom while perfect magnetic boundary at two sides. The unit cells of the metasurfaces are with width $w = 18mm$, gap size $g = 2mm$, substrate (Rogers duroid 5880) thickness $t = 3.175mm$, gap resistance $R = 10k\Omega$.

HIS is that there is a bandgap between the first TE and TM mode that does not support any wave propagation along the surface for the frequencies falls into the bandgap. The energy of the wave is stored in the small cavities resonating thus could be dissipated and absorbed in form of ohmic loss when placing an absorbing resistor at the gap between neighboring unit cells. When the switches are at OFF state, the vias are not visible by the impinging waves and the surface is reconfigured periodic patches without vias, which supports TM mode wave propagation along the surface at the same frequencies. The dispersion diagram of the surface with via on and off are shown in Fig. 5.3 (b). The results showed in Fig. 5.3 are at switch static conditions, resulting a linear and reciprocal structure that gives the same response when waves are transmitting from left or right side of the surface in Fig. 5.2.

The symmetry of response to transmitting surface waves could be broken by introducing time and spatial modulation. For the proposed surface above, when the switches turned ON and OFF in a sequence following a traveling wave manner, the property of the surface from one side to the other differs, showing nonreciprocal. While the surface wave

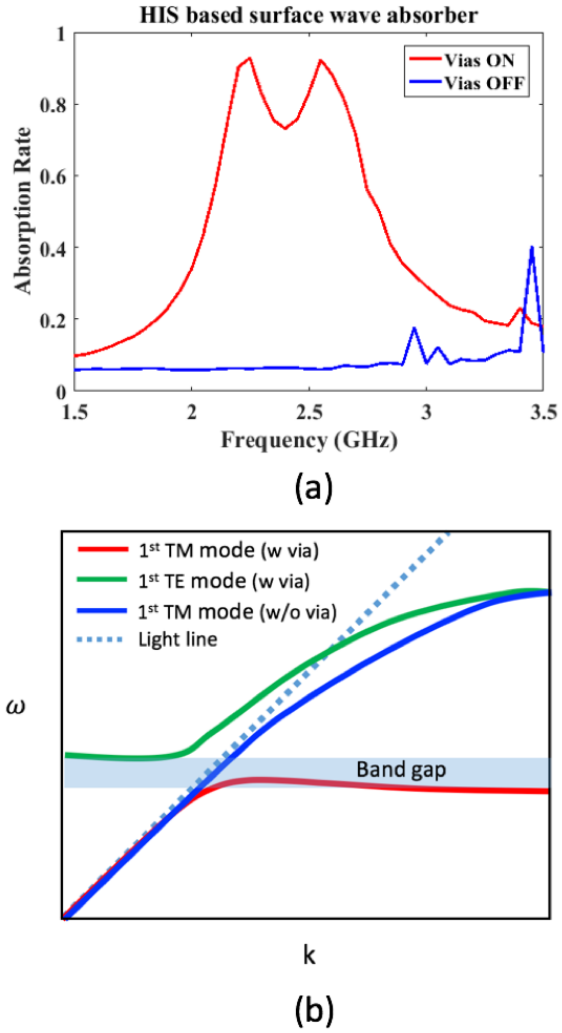

Figure 5.3: Simulation results of HIS absorber with via on and off.(a) Simulated absorption rate over frequencies with and without vias. (b) Dispersion diagram of the periodic surface with via switches ON and OFF. Surface waves with frequencies fall into bandgap of the HIS (via on) cannot be propagated but TM mode could be supported at periodic patches case (via off).

propagation follows the direction of the modulation direction (from one side to the other, switch from OFF to ON state), the traveling wave barely detects the vias long the traveling path, in other words, the surface appears closer to periodic patches without vias that supports the surface wave propagation. On the other hand, when waves coming from the opposite direction of the modulation direction, the whole surface is mostly equivalent to the HIS

with majority of the vias on, which stops surface waves from propagation and absorbed from ohmic losses at the gap resistors. Another way of addressing this spatiotemporal

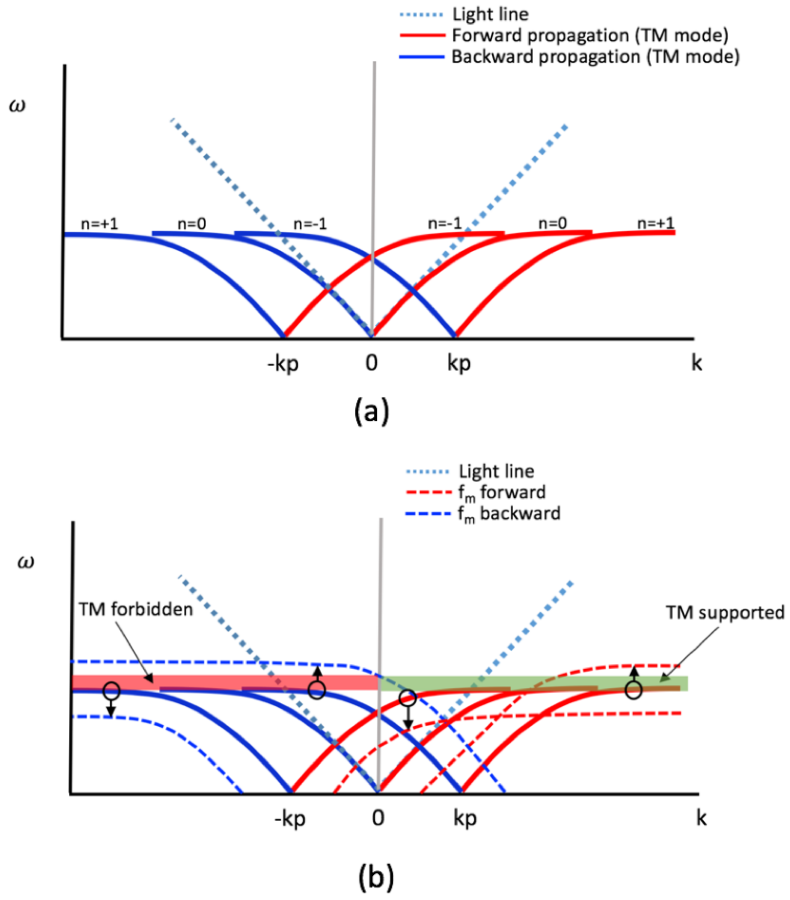

Figure 5.4: spatiotemporal modulation of the HIS presented in dispersion diagram.(a) Dispersion diagram of the first three space harmonics (n=0,±1), in which kz is the surface wave vector and p is the periodicity of the spatial modulation. (b) Time modulation to the dispersion curves in y axis. A TM mode forward propagation is supported while forbidden in backward propagation resulting a non-reciprocal property.

modulation is from dispersion diagram perspective analysis. The first TM mode of the HIS is considered as a fundamental mode, from which the modulations are carried out. The spatial modulation of the HIS, determined by the number of vias on and off per period, with +1 and -1 spatial harmonics are shown in Fig. 5.4 (a), modulated in x axis. When a

temporal modulation is applied to the surface, the dispersion diagrams are modulated in y axis shown in Fig. 5.4 (b). For propagation in forward directions (defined as same direction with the traveling modulation direction), the positive harmonics of the dispersion diagram is shifted up while the negative harmonics is shifted down, contrary for the negative direction propagations, shown in Fig. 5.4 (b). Combing all the dispersion diagrams, a supported TM mode dispersion curve is found for forward propagation while a band gap at the backward propagation. In other words, for waves at frequencies fall into the bandgap of backward transmission, they will be absorbed by the surface wave absorber while the forward direction TM wave transmission could be supported by this spatiotemporal modulation. The up and down shift of the dispersion diagram from the time modulation is determined by the modulation frequency f_m.

5.3 EM-circuit Co-simulation

To verify the nonreciprocal concept, we performed EM-circuit co-simulation. The same full wave simulation model is adopted and shown in Fig. 5.5 (a). Lumped ports are designed between top patch and the via vertically for each element to control the via connecting or isolating with the top patch from the ground. Also there are slumped ports assigned at the gaps between neighboring patches for assigning gap resistors. Wave ports are assigned at the left side (forward incidence) and right side (backward incidence) with characteristic impedance determined by the ratio of the height and the width of the TEM waveguide. The periodicity of the unit cells p is 20mm, patch width w is 18mm, gap size g is 2mm and the substrate (Roger Duroid 5870) thickness t is 3.175mm. The extracted S-matrix from a wide band (DC to 12GHz) full wave simulation is plugged into circuit simulator to perform transient simulation shown in Fig. 5.5 (b). The S-matrix is composed of two ports

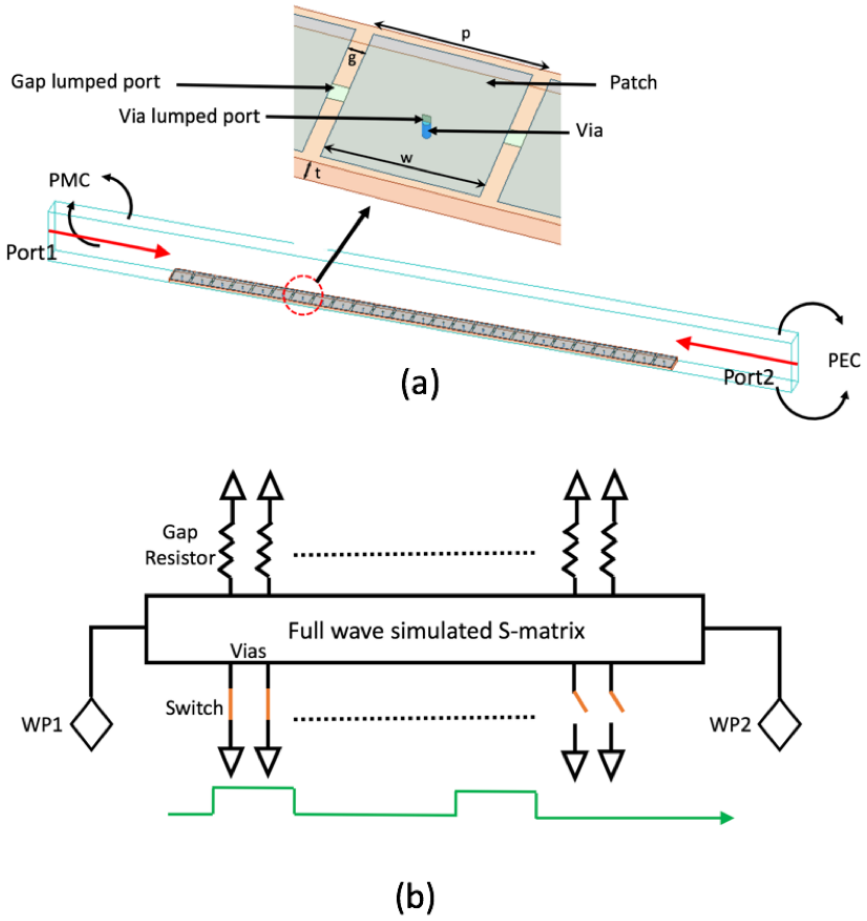

Figure 5.5: EM-circuit co-simulation models. (a) Full wave simulation model with periodic boundaries, perfect electric conductor at top and bottom while perfect magnetic boundary at two sides. The unit cells of the metasurfaces are with width $w = 18mm$, gap size $g = 2mm$, substrate (Rogers duroid 5880) thickness $t = 3.175mm$, gap lumped port and via lumped ports are assigned. (b) Solved EM model of the surface is plugged into the circuit simulator, with its lumped port connected with absorbing resistors at the gap and switches at the vias, with its two ports connected with wave ports to feed input waves.

at top on the left and right indicating transmitting and receiving ports with characteristic impedance same with the TEM waveguide. The gap ports are assigned resistors with resistance $R = 10k\Omega$ while the via ports are assigned to ideal switches which could control the vias to be conducted to the ground (switches on) or not (switches off), reconfiguring the surface to be HIS or periodic patches. A traveling square wave, which could modulate

the switch to be on and off following a sequence, is transmitted through a 50Ω impedance controlled transmission line from the left to the right. Here we are using square wave for the modulation is due to the surface unit cells have two discrete states (via conducted or not), which could be reached with high and low states of the square wave respectively. The modulation is in a traveling wave manner from WP1 direction towards WP2 direction. For forward transmission (left to right)/backward transmission (right to left), WP1/WP2 is assigned a source while WP2/WP1 is assigned to be a receiving port. By sweeping all interested frequencies in the transient simulation, the incident, transmitted and reflected power of the source could be obtained, thus absorption rate could be calculated from Equations.5.1. There are several parameters of the square wave for this traveling modulation could be optimized for this nonreciprocal surface wave absorber, including modulation wave's phase velocity, period and duty cycle, targeting maximizing the difference between the forward absorption and backward absorption rate. Phase velocity of modulation wave stays the same with the 1st TM mode surface wave phase velocity, which could be extracted from the dispersion curve from eigenmode simulation of the periodic patches without vias (approximately same with the speed of light), to ensure the maximum transmission of the power from the left to the right along the spatial modulation direction. The period and the duty cycle of the square waves are swept and optimized to give the largest difference in absorption rate from opposite incident directions. As mentioned above that the periodicity of the modulation determines the range of up and down shift of the dispersion curve, while the duty cycle of the modulating square wave determines the modulation depth. One extreme case is duty cycle to be 0, which indicates vias all off case maximizing the transmission rate. The other extreme case is duty cycle to be 1, which represents all vias are on forming a HIS, maximizing the absorption rate. For the proposed non-reciprocal metasurface surface wave

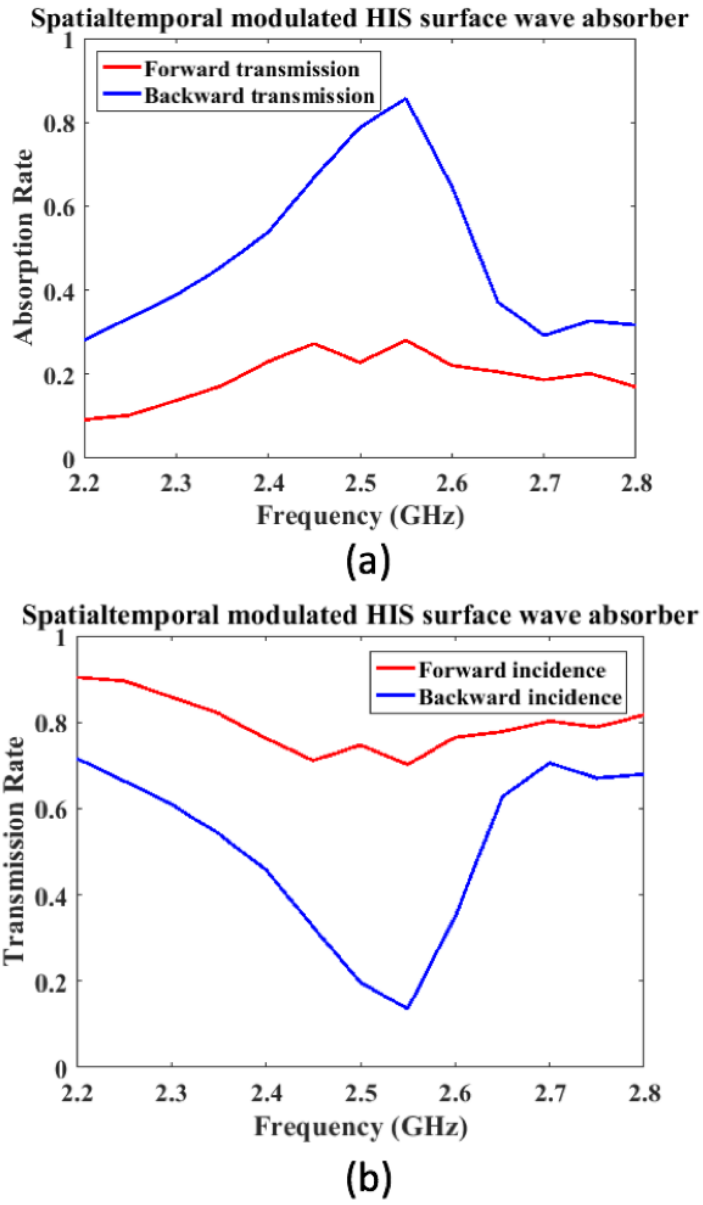

Figure 5.6: EM-circuit co-simulation results. (a) The absorption rate of forward and backward incidence in transient simulation is extracted with via switches modulated in a travelling manner at speed of light with period 1.2ns, 1/3 duty cycle. (b) The transmission rate of forward and backward incidence in transient simulation.

absorber, the period of the square wave is optimized to be 1.2 ns and the duty cycle is 1/3 accordingly. The absorption rate from forward (left) and backward (right) incidence, shown in Fig. 5.5 (a) and Fig. 5.5 (b). are simulated and plotted in Fig. 5.6 (a). At 2.55 GHz, the

peak absorption rate from backward incidence is 86% with a forward incidence to be 28%. The transmission rate of both directions of incidence are plotted in Fig. 5.6 (b).

5.4 Conclusions

Additionally, the proposed absorber could be functioning as a reciprocal switchable surface wave absorber. When switches are turned on, the surface is reconfigured to be HIS surface absorbers, while transparent to the surface wave at the same frequencies when switches are turned off all the time, which enables the absorber more flexibility.

In summary, we proposed a HIS based time modulated metasurface surface wave absorber. By using a traveling square wave modulating the HIS's vias conducting top patches to the ground, the absorber showed non-reciprocal properties in terms of incidence direction. At targeting frequencies, when the incident wave travels against the direction of the modulation, the majority of the power are being absorbed, but transmitted when along the direction of the modulation.

Chapter 5 is based on and is mostly a reprint of the following paper: **A. Li**, Y. LI, J. Long, E. Forati and D. Sievenpiper, "Time moduated non-reciprocal metasurface surface wave absorber", in preparation. The dissertation author was the primary author of the work in this chapter, and the co-author has approved the use of the material for this dissertation.

Chapter 6

Summary and Future Work

6.1 Summary of Work

In this thesis, the advance of applying active electronics on passive metasurface structures showed unique performances in various of applications, that could not be achieved with traditional passive structures. The thesis starts with an overview of the metasurface in their basic properties and applications, discussing their fundamental limitations. Then some examples of applying active electronics on the metasurface in applications of switchable absorber, microwave transmitter and non-reciprocal absorbers are demonstrated either experimentally or in simulation showing the advance properties when the surfaces are active powered.

Chapter 2 studies a significant property of the resonant metasurfaces, field enhancement. At microwave range, the field enhancement in the cavity of the high impedance surfaces is proportional to the quality factor of the surface. However, the highest field concentrates at the gap between neighboring unit cells when shined with normal incident waves, the magnitude of which is determined by the geometrical factor only irrelevant with

the surface quality factor. The field enhancement in inferred frequencies are also studied.

Chapter 3 introduces the first transistor based switchable and tunable metasurface absorbers. A TM surface wave absorbing scenario is specifically addressed, taking advantage of high impedance surface's band stop properties that could effectively prevent strong interference signals leaking through the gaps and discontinuities of the surface. When transistors are applied to the surface, positioned at the vias, the surface could be reconfigured thus switching the absorption on or off at different switching states. Also, absorption rate could also be tuned by applying different biasing voltages to the gate of the transistors. Two topologies of the switchable absorbers are simulated and fabricated and tested in the waveguides, showing a consistent results with the simulation. A large panel with a slot in the middle is fabricated and demonstrated the self adaptive switching capabilities of the metasurface.

Chapter 4 proposed a new type of RF/microwave transmitter, which could directly convert DC energy into RF radiation with the help of active loaded metasurfaces. The concept takes the normal radiation leaky wave mode of the high impedance surfaces, that could be charged to static DC energy at a charging state and then radiate the charged energy out at a oscillating state when the switches on the surfaces are turned on simultaneously. Two topologies of active switches loaded metasurfaces are designed in simulation, then fabricated and tested, which showed expected decaying sinusoidal output waveforms. This radiation could be be steered to wanted directions by simply adding delays to the switches in a row or column or both. The beam steering effect is simulated and demonstrated in EM-circuit co-simulation.

Chapter 5 brings spatial and time modulation to the metasurface absorbers thus enables the metasurface absorbers with more flexibility. The high impedance surfaces'

vias are modulated by turning on and off in a traveling manner along the direction of the incidence wave. This modulation breaks the symmetry of the dispersion curves of the surface in terms of forward and backward propagation thus could be optimized to support waves propagation in one propagation direction but stop the propagation and absorb the wave in the other propagation direction, presenting non-reciprocal property. The non-reciprocity of this surface wave active metasurface absorber is demonstrated in EM-circuit co-simulations.

In conclusion, the thesis gives some new concepts and examples and demonstrations of the benefits brought by the active electronics loading comparing with traditional passive solutions in terms of switchability, tunability, non-reciprocity as well as new approaches to antennas and potential new opportunities of microwave devices.

6.2 Future Works

It is just a starting point by applying the existing active electronics onto the metasurface. Actually this active loading could be broadened to a variety of passive structures including antennas, materials and other passive microwave devices. A more compact and integrated designs are required, for example IC design on top of the metasurfaces could enhance the performance and functionality [123].

For passive structures there are always fundamental limitations in terms of reciprocity, bandwidth, thickness, etc. This could be addressed to some extent by active loading and have great potentials. Non-foster circuit loaded devices, antennas and metasurfaces were studied and the bandwidth are greatly enhanced. However this approach is not usually stable when operation power is high nor when working frequencies are high. Time modulation techniques could be further explored and applied to the surface to enhance the bandwidth due to it's wide bandwidth properties [124].

Additionally, all these active loading approaches could be modified and applied in higher frequencies in optical frequency ranges.

Bibliography

[1] E. M. Purcell and D. J. Morin, *Electricity and magnetism*. Cambridge University Press, 2013.

[2] A. Li, S. Singh, and D. Sievenpiper, "Metasurfaces and their applications," *Nanophotonics*, vol. 7, no. 6, pp. 989–1011, 2018.

[3] S. B. Glybovski, S. A. Tretyakov, P. A. Belov, Y. S. Kivshar, and C. R. Simovski, "Metasurfaces: From microwaves to visible," *Physics Reports*, vol. 634, pp. 1–72, 2016.

[4] C. L. Holloway, E. F. Kuester, J. A. Gordon, J. O'Hara, J. Booth, and D. R. Smith, "An overview of the theory and applications of metasurfaces: The two-dimensional equivalents of metamaterials," *IEEE Antennas and Propagation Magazine*, vol. 54, no. 2, pp. 10–35, 2012.

[5] H.-T. Chen, A. J. Taylor, and N. Yu, "A review of metasurfaces: physics and applications," *Reports on Progress in Physics*, vol. 79, no. 7, p. 076401, 2016.

[6] R. Mittra, C. H. Chan, and T. Cwik, "Techniques for analyzing frequency selective surfaces-a review," *Proceedings of the IEEE*, vol. 76, no. 12, pp. 1593–1615, 1988.

[7] J. C. Vardaxoglou, *Frequency selective surfaces: analysis and design*. Research Studies Press London, 1997, vol. 997.

[8] B. A. Munk, *Frequency selective surfaces: theory and design*. John Wiley & Sons, 2005.

[9] N. I. Landy, S. Sajuyigbe, J. J. Mock, D. R. Smith, and W. J. Padilla, "Perfect metamaterial absorber," *Physical review letters*, vol. 100, no. 20, p. 207402, 2008.

[10] S. Kim and D. F. Sievenpiper, "Theoretical limitations for tm surface wave attenuation by lossy coatings on conducting surfaces," *IEEE Transactions on Antennas and Propagation*, vol. 62, no. 1, pp. 475–480.

[11] B. Zhu, Y. Feng, J. Zhao, C. Huang, and T. Jiang, "Switchable metamaterial reflector/absorber for different polarized electromagnetic waves," *Applied Physics Letters*, vol. 97, no. 5, p. 051906, 2010.

[12] D. Shrekenhamer, W.-C. Chen, and W. J. Padilla, "Liquid crystal tunable metamaterial absorber," *Physical review letters*, vol. 110, no. 17, p. 177403, 2013.

[13] Y. Yao, R. Shankar, M. A. Kats, Y. Song, J. Kong, M. Loncar, and F. Capasso, "Electrically tunable metasurface perfect absorbers for ultrathin mid-infrared optical modulators," *Nano letters*, vol. 14, no. 11, pp. 6526–6532, 2014.

[14] H. Wakatsuchi, S. Kim, J. J. Rushton, and D. F. Sievenpiper, "Waveform-dependent absorbing metasurfaces," *Physical review letters*, vol. 111, no. 24, p. 245501, 2013.

[15] C. Pfeiffer and A. Grbic, "Metamaterial huygens' surfaces: tailoring wave fronts with reflectionless sheets," *Physical review letters*, vol. 110, no. 19, p. 197401, 2013.

[16] J. Lee and D. F. Sievenpiper, "Patterning technique for generating arbitrary anisotropic impedance surfaces," *IEEE Transactions on Antennas and Propagation*, vol. 64, no. 11, pp. 4725–4732, 2016.

[17] R. Quarfoth and D. Sievenpiper, "Artificial tensor impedance surface waveguides," *IEEE Transactions on Antennas and Propagation*, vol. 61, no. 7, pp. 3597–3606, 2013.

[18] C. Caloz, T. Itoh, and A. Rennings, "Crlh metamaterial leaky-wave and resonant antennas," *IEEE Antennas and Propagation Magazine*, vol. 50, no. 5, 2008.

[19] D. F. Sievenpiper, "Forward and backward leaky wave radiation with large effective aperture from an electronically tunable textured surface," *IEEE transactions on antennas and propagation*, vol. 53, no. 1, pp. 236–247, 2005.

[20] M. Esquius-Morote, J. S. Gómez-Dı, and J. Perruisseau-Carrier, "Sinusoidally modulated graphene leaky-wave antenna for electronic beamscanning at thz," *IEEE Transactions on Terahertz Science and Technology*, vol. 4, no. 1, pp. 116–122, 2014.

[21] X.-C. Wang, W.-S. Zhao, J. Hu, and W.-Y. Yin, "Reconfigurable terahertz leaky-wave antenna using graphene-based high-impedance surface," *IEEE Transactions on Nanotechnology*, vol. 14, no. 1, pp. 62–69, 2015.

[22] Y. B. Li, B. G. Cai, Q. Cheng, and T. J. Cui, "Isotropic holographic metasurfaces for dual-functional radiations without mutual interferences," *Advanced Functional Materials*, vol. 26, no. 1, pp. 29–35, 2016.

[23] G. Minatti, S. Maci, P. De Vita, A. Freni, and M. Sabbadini, "A circularly-polarized isoflux antenna based on anisotropic metasurface," *IEEE Transactions on Antennas and Propagation*, vol. 60, no. 11, pp. 4998–5009, 2012.

[24] R. Fleury, F. Monticone, and A. Alù, "Invisibility and cloaking: Origins, present, and future perspectives," *Physical Review Applied*, vol. 4, no. 3, p. 037001, 2015.

[25] P.-Y. Chen and A. Alu, "Mantle cloaking using thin patterned metasurfaces," *physical review B*, vol. 84, no. 20, p. 205110, 2011.

[26] P.-Y. Chen, J. Soric, Y. R. Padooru, H. M. Bernety, A. B. Yakovlev, and A. Alù, "Nanostructured graphene metasurface for tunable terahertz cloaking," *New Journal of Physics*, vol. 15, no. 12, p. 123029, 2013.

[27] S. Liu, H.-X. Xu, H. C. Zhang, and T. J. Cui, "Tunable ultrathin mantle cloak via varactor-diode-loaded metasurface," *Optics express*, vol. 22, no. 11, pp. 13 403–13 417, 2014.

[28] B. Orazbayev, N. M. Estakhri, M. Beruete, and A. Alù, "Terahertz carpet cloak based on a ring resonator metasurface," *Physical Review B*, vol. 91, no. 19, p. 195444, 2015.

[29] P.-Y. Chen, C. Argyropoulos, and A. Alù, "Broadening the cloaking bandwidth with non-foster metasurfaces," *Physical review letters*, vol. 111, no. 23, p. 233001, 2013.

[30] D. L. Sounas, R. Fleury, and A. Alù, "Unidirectional cloaking based on metasurfaces with balanced loss and gain," *Physical Review Applied*, vol. 4, no. 1, p. 014005, 2015.

[31] H.-T. Chen, W. J. Padilla, M. J. Cich, A. K. Azad, R. D. Averitt, and A. J. Taylor, "A metamaterial solid-state terahertz phase modulator," *Nature photonics*, vol. 3, no. 3, p. 148, 2009.

[32] Z. Miao, Q. Wu, X. Li, Q. He, K. Ding, Z. An, Y. Zhang, and L. Zhou, "Widely tunable terahertz phase modulation with gate-controlled graphene metasurfaces," *Physical Review X*, vol. 5, no. 4, p. 041027, 2015.

[33] B. Bai, Y. Svirko, J. Turunen, and T. Vallius, "Optical activity in planar chiral metamaterials: Theoretical study," *Physical Review A*, vol. 76, no. 2, p. 023811, 2007.

[34] J. B. Pendry, "Negative refraction makes a perfect lens," *Physical review letters*, vol. 85, no. 18, p. 3966, 2000.

[35] M. Bosiljevac, M. Casaletti, F. Caminita, Z. Sipus, and S. Maci, "Non-uniform metasurface luneburg lens antenna design," *IEEE transactions on antennas and propagation*, vol. 60, no. 9, pp. 4065–4073, 2012.

[36] M. Khorasaninejad, F. Aieta, P. Kanhaiya, M. A. Kats, P. Genevet, D. Rousso, and F. Capasso, "Achromatic metasurface lens at telecommunication wavelengths," *Nano letters*, vol. 15, no. 8, pp. 5358–5362, 2015.

[37] F. Aieta, P. Genevet, M. A. Kats, N. Yu, R. Blanchard, Z. Gaburro, and F. Capasso, "Aberration-free ultrathin flat lenses and axicons at telecom wavelengths based on plasmonic metasurfaces," *Nano letters*, vol. 12, no. 9, pp. 4932–4936, 2012.

[38] X. Ni, A. V. Kildishev, and V. M. Shalaev, "Metasurface holograms for visible light," *Nature communications*, vol. 4, p. 2807, 2013.

[39] G. Zheng, H. Mühlenbernd, M. Kenney, G. Li, T. Zentgraf, and S. Zhang, "Metasurface holograms reaching 80% efficiency," *Nature nanotechnology*, vol. 10, no. 4, p. 308, 2015.

[40] W. Ye, F. Zeuner, X. Li, B. Reineke, S. He, C.-W. Qiu, J. Liu, Y. Wang, S. Zhang, and T. Zentgraf, "Spin and wavelength multiplexed nonlinear metasurface holography," *Nature communications*, vol. 7, p. 11930, 2016.

[41] J. Hunt, T. Driscoll, A. Mrozack, G. Lipworth, M. Reynolds, D. Brady, and D. R. Smith, "Metamaterial apertures for computational imaging," *Science*, vol. 339, no. 6117, pp. 310–313, 2013.

[42] C. M. Watts, D. Shrekenhamer, J. Montoya, G. Lipworth, J. Hunt, T. Sleasman, S. Krishna, D. R. Smith, and W. J. Padilla, "Terahertz compressive imaging with metamaterial spatial light modulators," *Nature Photonics*, vol. 8, no. 8, p. 605, 2014.

[43] T. Sleasman, M. Boyarsky, M. F. Imani, T. Fromenteze, J. N. Gollub, and D. R. Smith, "Single-frequency microwave imaging with dynamic metasurface apertures," *JOSA B*, vol. 34, no. 8, pp. 1713–1726, 2017.

[44] D. Sievenpiper, L. Zhang, R. F. Broas, N. G. Alexopolous, and E. Yablonovitch, "High-impedance electromagnetic surfaces with a forbidden frequency band," *IEEE Transactions on Microwave Theory and techniques*, vol. 47, no. 11, pp. 2059–2074, 1999.

[45] D. Sievenpiper, H.-P. Hsu, J. Schaffner, G. Tangonan, R. Garcia, and S. Ontiveros, "Low-profile, four-sector diversity antenna on high-impedance ground plane," *Electronics Letters*, vol. 36, no. 16, pp. 1343–1345, 2000.

[46] A. Tennant and B. Chambers, "A single-layer tuneable microwave absorber using an active fss," *IEEE Microwave and Wireless Components Letters*, vol. 14, no. 1, pp. 46–47, 2004.

[47] W. Dallenbach and W. Kleinsteuber, "Reflection and absorption of decimeter-waves by plane dielectric layers," *Hochfreq. u Elektroak*, vol. 51, pp. 152–156, 1938.

[48] W. W. Salisbury, "Absorbent body for electromagnetic waves," Jun. 10 1952, uS Patent 2,599,944.

[49] J. B. Mueller, N. A. Rubin, R. C. Devlin, B. Groever, and F. Capasso, "Metasurface polarization optics: independent phase control of arbitrary orthogonal states of polarization," *Physical review letters*, vol. 118, no. 11, p. 113901, 2017.

[50] C. Valagiannopoulos, A. Tukiainen, T. Aho, T. Niemi, M. Guina, S. Tretyakov, and C. Simovski, "Perfect magnetic mirror and simple perfect absorber in the visible spectrum," *Physical Review B*, vol. 91, no. 11, p. 115305, 2015.

[51] R. Quarfoth and D. Sievenpiper, "Alteration of electromagnetic scattering using hard and soft anisotropic impedance surfaces," *IEEE Transactions on Antennas and Propagation*, vol. 63, no. 10, pp. 4593–4599, 2015.

[52] S. Sun, Q. He, S. Xiao, Q. Xu, X. Li, and L. Zhou, "Gradient-index meta-surfaces as a bridge linking propagating waves and surface waves," *Nature materials*, vol. 11, no. 5, p. 426, 2012.

[53] C. A. Valagiannopoulos, J. Vehmas, C. R. Simovski, S. A. Tretyakov, and S. I. Maslovski, "Electromagnetic energy sink," *Physical Review B*, vol. 92, no. 24, p. 245402, 2015.

[54] Y. Liu and X. Zhang, "Metasurfaces for manipulating surface plasmons," *Applied Physics Letters*, vol. 103, no. 14, p. 141101, 2013.

[55] Y. Yang, L. Jing, L. Shen, Z. Wang, B. Zheng, H. Wang, E. Li, N.-H. Shen, T. Koschny, and H. C. Soukoulis, Costas M, "Hyperbolic spoof plasmonic metasurfaces," *NPG Asia Materials*, vol. 9, no. 8, p. e428, 2017.

[56] D. Sievenpiper, H.-P. Hsu, and R. M. Riley, "Low-profile cavity-backed crossed-slot antenna with a single-probe feed designed for 2.34-ghz satellite radio applications," *IEEE transactions on antennas and propagation*, vol. 52, no. 3, pp. 873–879, 2004.

[57] R. J. Broas, D. F. Sievenpiper, and E. Yablonovitch, "An application of high-impedance ground planes to phased array antennas," *IEEE transactions on antennas and propagation*, vol. 53, no. 4, pp. 1377–1381, 2005.

[58] L. Novotny, E. J. Sánchez, and X. S. Xie, "Near-field optical imaging using metal tips illuminated by higher-order hermite–gaussian beams," *Ultramicroscopy*, vol. 71, no. 1-4, pp. 21–29, 1998.

[59] N. Liu, M. Mesch, T. Weiss, M. Hentschel, and H. Giessen, "Infrared perfect absorber and its application as plasmonic sensor," *Nano letters*, vol. 10, no. 7, pp. 2342–2348, 2010.

[60] H. A. Atwater and A. Polman, "Plasmonics for improved photovoltaic devices," *Nature materials*, vol. 9, no. 3, p. 205, 2010.

[61] Q. Sun, K. Ueno, H. Yu, A. Kubo, Y. Matsuo, and H. Misawa, "Direct imaging of the near field and dynamics of surface plasmon resonance on gold nanostructures using photoemission electron microscopy," *Light: science & applications*, vol. 2, no. 12, p. e118, 2013.

[62] A. Li, S. Kim, Y. Luo, Y. Li, J. Long, and D. F. Sievenpiper, "High-power transistor-based tunable and switchable metasurface absorber," *IEEE Transactions on Microwave Theory and Techniques*, vol. 65, no. 8, pp. 2810–2818, 2017.

[63] A. Li, E. Forati, and D. Sievenpiper, "Study of the electric field enhancement of high-impedance surfaces," in *Antennas and Propagation (APSURSI), 2016 IEEE International Symposium on*. IEEE, 2016, pp. 105–106.

[64] P. B. Johnson and R.-W. Christy, "Optical constants of the noble metals," *Physical review B*, vol. 6, no. 12, p. 4370, 1972.

[65] S. Kim, J. Jin, Y.-J. Kim, I.-Y. Park, Y. Kim, and S.-W. Kim, "High-harmonic generation by resonant plasmon field enhancement," *Nature*, vol. 453, no. 7196, p. 757, 2008.

[66] W. L. Barnes, A. Dereux, and T. W. Ebbesen, "Surface plasmon subwavelength optics," *nature*, vol. 424, no. 6950, p. 824, 2003.

[67] S. A. Maier, "Plasmonic field enhancement and sers in the effective mode volume picture," *Optics Express*, vol. 14, no. 5, pp. 1957–1964, 2006.

[68] E. Forati, T. J. Dill, A. R. Tao, and D. Sievenpiper, "Photoemission-based microelectronic devices," *Nature communications*, vol. 7, p. 13399, 2016.

[69] S. Ramo, J. R. Whinnery, and T. Van Duzer, *Fields and waves in communication electronics*. John Wiley & Sons, 2008.

[70] A. Cvitkovic, N. Ocelic, J. Aizpurua, R. Guckenberger, and R. Hillenbrand, "Infrared imaging of single nanoparticles via strong field enhancement in a scanning nanogap," *Physical review letters*, vol. 97, no. 6, p. 060801, 2006.

[71] M. Käll, H. Xu, and P. Johansson, "Field enhancement and molecular response in surface-enhanced raman scattering and fluorescence spectroscopy," *Journal of Raman Spectroscopy: An International Journal for Original Work in all Aspects of Raman Spectroscopy, Including Higher Order Processes, and also Brillouin and Rayleigh Scattering*, vol. 36, no. 6-7, pp. 510–514, 2005.

[72] Y. Lu, G. L. Liu, J. Kim, Y. X. Mejia, and L. P. Lee, "Nanophotonic crescent moon structures with sharp edge for ultrasensitive biomolecular detection by local electromagnetic field enhancement effect," *Nano letters*, vol. 5, no. 1, pp. 119–124, 2005.

[73] J. A. Fan, C. Wu, K. Bao, J. Bao, R. Bardhan, N. J. Halas, V. N. Manoharan, P. Nordlander, G. Shvets, and F. Capasso, "Self-assembled plasmonic nanoparticle clusters," *science*, vol. 328, no. 5982, pp. 1135–1138, 2010.

[74] F. Monticone and A. Alu, "Metamaterial, plasmonic and nanophotonic devices," *Reports on Progress in Physics*, vol. 80, no. 3, p. 036401, 2017.

[75] S. Kim, H. Wakatsuchi, J. J. Rushton, and D. F. Sievenpiper, "Switchable nonlinear metasurfaces for absorbing high power surface waves," *Applied Physics Letters*, vol. 108, no. 4, p. 041903, 2016.

[76] H. Wakatsuchi, F. Gao, S. Yagitani, and D. F. Sievenpiper, "Responses of waveform-selective absorbing metasurfaces to oblique waves at the same frequency," *Scientific reports*, vol. 6, p. 31371, 2016.

[77] K. Crozier, A. Sundaramurthy, G. Kino, and C. Quate, "Optical antennas: Resonators for local field enhancement," *Journal of Applied Physics*, vol. 94, no. 7, pp. 4632–4642, 2003.

[78] D. R. Ward, F. Hüser, F. Pauly, J. C. Cuevas, and D. Natelson, "Optical rectification and field enhancement in a plasmonic nanogap," *Nature nanotechnology*, vol. 5, no. 10, p. 732, 2010.

[79] V. A. Zenin, A. Andryieuski, R. Malureanu, I. P. Radko, V. S. Volkov, D. K. Gramotnev, A. V. Lavrinenko, and S. I. Bozhevolnyi, "Boosting local field enhancement by on-chip nanofocusing and impedance-matched plasmonic antennas," *Nano letters*, vol. 15, no. 12, pp. 8148–8154, 2015.

[80] C. L. Holloway, R. R. Delyser, R. F. German, P. McKenna, and M. Kanda, "Comparison of electromagnetic absorber used in anechoic and semi-anechoic chambers for emissions and immunity testing of digital devices," *IEEE Transactions on Electromagnetic Compatibility*, vol. 39, no. 1, pp. 33–47, 1997.

[81] B.-K. C. H.-T. Chuah, "Modeling of rf absorber for application in the design of anechoic chamber," *Progress In Electromagnetics Research*, vol. 43, pp. 273–285, 2003.

[82] Y. Naito and K. Suetake, "Application of ferrite to electromagnetic wave absorber and its characteristics," *IEEE Transactions on Microwave Theory and Techniques*, vol. 19, no. 1, pp. 65–72, 1971.

[83] S. Sugimoto, K. Okayama, S.-i. Kondo, H. Ota, M. Kimura, Y. Yoshida, H. Nakamura, D. Book, T. Kagotani, and M. Homma, "Barium m-type ferrite as an electromagnetic microwave absorber in the ghz range," *Materials Transactions, JIM*, vol. 39, no. 10, pp. 1080–1083, 1998.

[84] M. Li, H.-L. Yang, X.-W. Hou, Y. Tian, and D.-Y. Hou, "Perfect metamaterial absorber with dual bands," *Progress In Electromagnetics Research*, vol. 108, pp. 37–49, 2010.

[85] M. Li, S. Xiao, Y.-Y. Bai, and B.-Z. Wang, "An ultrathin and broadband radar absorber using resistive fss," *IEEE Antennas and Wireless Propagation Letters*, vol. 11, pp. 748–751, 2012.

[86] A. H. Panaretos, D. E. Brocker, and D. H. Werner, "Ultra-thin absorbers comprised by cascaded high-impedance and frequency selective surfaces," *IEEE Antennas and Wireless Propagation Letters*, vol. 14, pp. 1089–1092, 2015.

[87] B. Zhu, Z. Wang, C. Huang, Y. Feng, J. Zhao, and T. Jiang, "Polarization insensitive metamaterial absorber with wide incident angle," *Progress In Electromagnetics Research*, vol. 101, pp. 231–239, 2010.

[88] J. Lee and S. Lim, "Bandwidth-enhanced and polarisation-insensitive metamaterial absorber using double resonance," *Electronics Letters*, vol. 47, no. 1, pp. 8–9, 2011.

[89] G. I. Kiani, K. L. Ford, K. P. Esselle, A. R. Weily, and C. J. Panagamuwa, "Oblique incidence performance of a novel frequency selective surface absorber," *IEEE Transactions on Antennas and Propagation*, vol. 55, no. 10, pp. 2931–2934, 2007.

[90] A. Fallahi, A. Yahaghi, H.-R. Benedickter, H. Abiri, M. Shahabadi, and C. Hafner, "Thin wideband radar absorbers," *IEEE Transactions on Antennas and Propagation*, vol. 58, no. 12, pp. 4051–4058, 2010.

[91] J. Zhao, Q. Cheng, J. Chen, M. Q. Qi, W. X. Jiang, and T. J. Cui, "A tunable metamaterial absorber using varactor diodes," *New Journal of Physics*, vol. 15, no. 4, p. 043049, 2013.

[92] Y. Huang, G. Wen, W. Zhu, J. Li, L.-M. Si, and M. Premaratne, "Experimental demonstration of a magnetically tunable ferrite based metamaterial absorber," *Optics express*, vol. 22, no. 13, pp. 16 408–16 417, 2014.

[93] H. Wakatsuchi, S. Kim, J. J. Rushton, and D. F. Sievenpiper, "Circuit-based nonlinear metasurface absorbers for high power surface currents," *Applied Physics Letters*, vol. 102, no. 21, p. 214103, 2013.

[94] D. F. Sievenpiper, "Nonlinear grounded metasurfaces for suppression of high-power pulsed rf currents," *IEEE Antennas and Wireless Propagation Letters*, vol. 10, pp. 1516–1519, 2011.

[95] H. Wakatsuchi, J. Rushton, J. Lee, F. Gao, M. Jacob, S. Kim, and D. Sievenpiper, "Experimental demonstration of nonlinear waveform-dependent metasurface absorber with pulsed signals," *Electronics Letters*, vol. 49, no. 24, pp. 1530–1531, 2013.

[96] M. Yoo and S. Lim, "Active metasurface for controlling reflection and absorption properties," *Applied Physics Express*, vol. 7, no. 11, p. 112204, 2014.

[97] J. Li, J. Jiang, Y. He, W. Xu, M. Chen, L. Miao, and S. Bie, "Design of a tunable low-frequency and broadband radar absorber based on active frequency selective surface," *IEEE Antennas and Wireless Propagation Letters*, vol. 15, pp. 774–777, 2016.

[98] P. Kong, X. Yu, Z. Liu, K. Zhou, Y. He, L. Miao, and J. Jiang, "A novel tunable frequency selective surface absorber with dual-dof for broadband applications," *Optics express*, vol. 22, no. 24, pp. 30 217–30 224, 2014.

[99] J. F. Mulligan, "Heinrich hertz and the development of physics," *Physics Today*, vol. 42, pp. 50–57, 1989.

[100] J. V. Jelley, "Cherenkov radiation and its applications," 1958.

[101] V. Pafomov, "Transition radiation and cerenkov radiation," *Soviet. Phys. JETP*, vol. 9, p. 1321, 1959.

[102] L. Sch, *Beam-wave interaction in periodic and quasi-periodic structures*. Springer Science & Business Media, 2011.

[103] A. S. Gilmour Jr, "Microwave tubes," *Dedham, MA, Artech House, 1986, 502 p.*, 1986.

[104] C. L. Holloway, M. A. Mohamed, E. F. Kuester, and A. Dienstfrey, "Reflection and transmission properties of a metafilm: With an application to a controllable surface composed of resonant particles," *IEEE Transactions on Electromagnetic Compatibility*, vol. 47, no. 4, pp. 853–865, 2005.

[105] D. Sievenpiper, J. Schaffner, J. Lee, and S. Livingston, "A steerable leaky-wave antenna using a tunable impedance ground plane," *IEEE Antennas and Wireless Propagation Letters*, vol. 1, no. 1, pp. 179–182, 2002.

[106] Z. Luo, X. Chen, J. Long, R. Quarfoth, and D. Sievenpiper, "Nonlinear power-dependent impedance surface," *IEEE Transactions on Antennas and Propagation*, vol. 63, no. 4, pp. 1736–1745, 2015.

[107] M. Mansuripur, "The faraday effect," *Optics and Photonics News*, vol. 10, no. 11, pp. 32–36, 1999.

[108] C. L. Hogan, "The ferromagnetic faraday effect at microwave frequencies and its applications," *Reviews of Modern Physics*, vol. 25, no. 1, p. 253, 1953.

[109] C. Caloz, A. Alù, S. Tretyakov, D. Sounas, K. Achouri, and Z.-L. Deck-Léger, "Electromagnetic nonreciprocity," *Physical Review Applied*, vol. 10, no. 4, p. 047001, 2018.

[110] C. Caloz and A. Alù, "Guest editorial special cluster on magnetless nonreciprocity in electromagnetics," *IEEE Antennas and Wireless Propagation Letters*, vol. 17, no. 11, pp. 1931–1937, 2018.

[111] S. Taravati, B. A. Khan, S. Gupta, K. Achouri, and C. Caloz, "Nonreciprocal nongyrotropic magnetless metasurface," *IEEE Transactions on Antennas and Propagation*, vol. 65, no. 7, pp. 3589–3597, 2017.

[112] R. Fleury, D. L. Sounas, C. F. Sieck, M. R. Haberman, and A. Alù, "Sound isolation and giant linear nonreciprocity in a compact acoustic circulator," *Science*, vol. 343, no. 6170, pp. 516–519, 2014.

[113] L. Felsen and G. Whitman, "Wave propagation in time-varying media," *IEEE Transactions on Antennas and Propagation*, vol. 18, no. 2, pp. 242–253, 1970.

[114] D. K. Kalluri, *Electromagnetics of time varying complex media: frequency and polarization transformer*. CRC Press, 2016.

[115] R. Fante, "Transmission of electromagnetic waves into time-varying media," *IEEE Transactions on Antennas and Propagation*, vol. 19, no. 3, pp. 417–424, 1971.

[116] Y. Hadad, J. C. Soric, and A. Alu, "Breaking temporal symmetries for emission and absorption," *Proceedings of the National Academy of Sciences*, p. 201517363, 2016.

[117] S. Taravati and C. Caloz, "Mixer-duplexer-antenna leaky-wave system based on periodic space-time modulation," *IEEE Transactions on Antennas and Propagation*, vol. 65, no. 2, pp. 442–452, 2017.

[118] Y. Hadad, D. Sounas, and A. Alu, "Space-time gradient metasurfaces," *Physical Review B*, vol. 92, no. 10, p. 100304, 2015.

[119] A. Kord, D. L. Sounas, and A. Alù, "Magnet-less circulators based on spatiotemporal modulation of bandstop filters in a delta topology," *IEEE Transactions on Microwave Theory and Techniques*, vol. 66, no. 2, pp. 911–926, 2018.

[120] D. Correas-Serrano, J. Gomez-Diaz, D. Sounas, Y. Hadad, A. Alvarez-Melcon, and A. Alù, "Nonreciprocal graphene devices and antennas based on spatiotemporal modulation," *IEEE Antennas and Wireless Propagation Letters*, vol. 15, pp. 1529–1532, 2016.

[121] R. Fleury, D. L. Sounas, and A. Alu, "Non-reciprocal optical mirrors based on spatio-temporal modulation," *arXiv preprint arXiv:1709.00702*, 2017.

[122] N. Chamanara, S. Taravati, Z.-L. Deck-Léger, and C. Caloz, "Optical isolation based on space-time engineered asymmetric photonic band gaps," *Physical Review B*, vol. 96, no. 15, p. 155409, 2017.

[123] A. Nagulu, T. Dinc, Z. Xiao, M. Tymchenko, D. Sounas, A. Alù, and H. Krishnaswamy, "Non-reciprocal components based on switched transmission lines," *arXiv preprint arXiv:1803.06690*, 2018.

[124] M. M. Biedka, R. Zhu, Q. M. Xu, and Y. E. Wang, "Ultra-wide band non-reciprocity through sequentially-switched delay lines," *Scientific reports*, vol. 7, p. 40014, 2017.

[125] S. Tretyakov and S. Maslovski, "Thin absorbing structure for all incidence angles based on the use of a high-impedance surface," *Microwave and Optical Technology Letters*, vol. 38, no. 3, pp. 175–178, 2003.

[126] N. Engheta, "Thin absorbing screens using metamaterial surfaces," 2002.

[127] O. Luukkonen, F. Costa, C. R. Simovski, A. Monorchio, and S. A. Tretyakov, "A thin electromagnetic absorber for wide incidence angles and both polarizations," *IEEE transactions on antennas and propagation*, vol. 57, no. 10, pp. 3119–3125, 2009.